UNIVERSITY OF CALIFORNIA, SAN DIEGO

High resolution image reconstruction of pulsar B0834+06 scattered by the interstellar medium

A dissertation submitted in partial satisfaction of the
requirements for the degree
Doctor of Philosophy

in

Electrical Engineering(Electrical Circuits & System)

by

Jianjian Gao

Committee in charge:

William A. Coles, Co-Chair
Barney J. Rickett, Co-Chair
Walter F. Brisken
William S. Hodgkiss
Tom W. Murphy
Kevin B. Quest

2012

The dissertation of Jianjian Gao is approved, and it is acceptable in quality and form for publication on microfilm and electronically:

_____

_____

_____

_____

_____
Co-Chair

_____
Co-Chair

University of California, San Diego

2012

DEDICATION

To Dad - I believe you will make it.

TABLE OF CONTENTS

LIST OF FIGURES

LIST OF TABLES

ACKNOWLEDGEMENTS

I would like to thank Barney Rickett and Bill Coles for their immense contribution to the successful completion of the dissertation. Their guidance, encouragement and patience were an invaluable help to me. Barney Rickett is the most kind person I have ever met and he makes everything so easy for me. Bill Coles taught me so much things that I will benefit from it for the rest of my life. Both of them are the most brilliant people I ever met and I learned so much from them.

I would also thank Walter Brisken and Adam Deller for their correlated VLBI data on pulsar B0834+06. Without their data, I wouldn't have material to work on.

I would also thank my friends and my family for their constant support and encouragement.

Chapter 2, in full, is a reprint of the material as it appears in ApJ 2010. W. F. Brisken, J.-P. Macquart, J. J. Gao, B. J. Rickett, W. A. Coles, A. T. Deller, S. J. Tingay, C. J. West, 2010. The dissertation author was the primary investigator and author of this paper.

VITA

2003	B.S. in Electrical Engineering, Beijing University of Chem. Tech., Beijing, China
2006	M.S. in Applied Physics, Graduate University of Chinese Academic of Sciences, Beijing, China
2006-2010	Graduate Research Assistant, University of California, San Diego
2010-2012	Graduate Teaching Assistant, University of California, San Diego
2012	Ph.D. in Electrical Engineering (Electrical Circuits & System), University of California, San Diego

PUBLICATIONS

Barney Rickett, Dan Stinebring, Bill Coles and J. J. Gao, "Pulsar Scintillation Arcs reveal filaments in the Interstellar Plasma", *AIP Conference Proceedings*, 1357, 97-100, 2011.

Gao, J. J.,Rickett, B. J., Coles, W. A., "Scattered image reconstruction of Pulsar B0834+06", *Proceedings of the SPIE*, 7800, 78000M-78000M-10, 2010

W. F. Brisken, J.-P. Macquart, J. J. Gao, B. J. Rickett, W. A. Coles, A. T. Deller, S. J. Tingay, and C. J. West, "100 μas Resolution VLBI Image of Anisotropic Interstellar Scattering Toward Pulsar B0834+06", *The Astrophysical Journal*, 708, 232243, 2010

Coles, W. A.; Rickett, B. J.; Gao, J. J.; Hobbs, G.; Verbiest, J. P. W., "Scattering of Pulsar Radio Emission by the Interstellar Plasma", , *The Astrophysical Journal*, 171, 1206-1221, 2010

ABSTRACT OF THE DISSERTATION

High resolution image reconstruction of pulsar B0834+06 scattered by the interstellar medium

by

Jianjian Gao

Doctor of Philosophy in Electrical Engineering(Electrical Circuits & System)

University of California, San Diego, 2012

William A. Coles, Co-Chair
Barney J. Rickett, Co-Chair

The scattered radio image of a pulsar, as a result of the radio wave passing through the turbulent interstellar plasma, is a valuable probe of the plasma turbulence. However the scattering angles are often so small, typically a few milli-arcsec, that the radio image cannot be resolved even with very long baseline interferometry (VLBI).

We used several different methods to reconstruct the scattered brightness image of pulsar B0834+06. We first combined the secondary spectrum technique with VLBI astrometry and successfully mapped the scattered brightness image

of pulsar B0834+06 at 327 MHz with an angular resolution 100 times finer than would have been possible with VLBI alone. We find that the scattering occurs in a compact region about 420 pc from the Earth. This image has two components, both essentially linear and nearly parallel. The primary feature is highly inhomogeneous on spatial scales as small as 0.05 AU, and extremely anisotropic. The second feature (called offset feature) is much fainter and is displaced from the axis of the primary feature by about 9 AU. We find that the velocity of the scattering plasma is 16 ± 10 km s^{-1}approximately parallel to the axis of the linear feature. Another technique is then presented which allows reconstruction of the core scattered brightness image in two dimensions from individual reversed sub-arc, providing an estimate of the axial ratio of the anisotropic turbulence. we obtained well-estimated 2 dimensional core image, and successfully estimated the half power width in both parallel and perpendicular direction ($\sim$ 3.85 mas and $\sim$ 1.3 mas respectively) with axial ratio ~ 3. Based on previous knowledge that this brightness image is highly elongated, we take it to the extreme and find a very good scattered brightness model: a 1-dimensional curvi-line model for primary feature, and a two straight-line linear model for offset feature. We also found that offset feature is frequency dependent.

Considering all those interesting properties of this plasma turbulence, we came up with two possible geometry models for the physical plasma turbulence behind the scattered brightness image, the parallel geometry model and the orthogonal geometry model. Although no direct proof is available, we believe orthogonal model fits our observation better. It doesn't require the pulsar to be underneath the center of the primary feature, and it's easy to explain the similarity of those two data sets 22 months apart. A prism-shaped screen provides an explanation of the 1 ms offset feature and also helps to explain the frequency dependence of the offset feature.

Chapter 1

Introduction

1.1 Pulsars

A pulsar is a highly magnetized, rotating neutron star that emits a beam of electromagnetic radiation. Neutron stars are very dense, and have short, regular rotational periods. When the beam of emission is pointing towards the Earth, radiation can be observed on Earth, like a lighthouse. Pulsars have very precise periods which range from roughly milliseconds to seconds.

Pulsars were first discovered by Jocelyn Bell and Antony Hewish at Cambridge University in 1967 [43]. It came about as a unexpected result of putting into operation a large radio telescope array designed to study the interplanetary scintillation of compact radio sources. Until now about 2000 pulsars have been discovered, and the number has been increasing very fast due to continuing all-sky surveys targeted at pulsars.

The formation of a pulsar begin when the core of a massive star is compressed during a supernova and collapses into a neutron star. Since most of its angular momentum is retained, a pulsar has very high rotation speed (in the range of $\sim$1.4ms to $\sim$8.5s). A beam of radiation is emitted along the magnetic axis of the pulsar, which spins along with the rotation of the neutron star. Its magnetic axis is not necessarily the same as rotational axis, and this misalignment causes

the beam to sweep like a lighthouse, which leads to the "pulsed" nature of its appearance. It also means that we can see only a small fraction of the pulsars for which the beam passes over the Earth.

Individual pulses vary greatly in intensity, However, if several hundred pulses are added together, a very stable pulse profile is obtained. Duty cycle (pulse time length over period) is typically 5%, some are much smaller than 1%, some are nearly 100% too.

Pulsars are physics laboratories providing extreme conditions [44], i.e. deep gravitational potentials, densities exceeding nuclear densities, high electric and magnetic fields, which are not available on Earth. Magnetic fields which average 10^8 gauss can reach 10^{14} or 10^{15} gauss. Electric fields are high enough to cause pair production so the pulsar wind is an electron-positron plasma. Pulse periods can be measured with accuracies approaching 1 part in 10^{16}, which makes it possible to measure extremely small perturbations such as those that might be caused by gravitational waves radiated by orbiting massive bodies, such as a pair of black-holes.

The study of pulsars has resulted in many applications in physics and astronomy, such as the confirmation of the existence of gravitational radiation as predicted by general relativity and the first detection of an extrasolar planetary system. Pulsar can also be used as precise clocks because of its precise period, especially millisecond pulsars for which the long term stability is comparable with our best atomic clocks. The radiation from pulsars passes through the interstellar medium (ISM) before reaching the Earth. With their sharp and short-duration pulse profiles, small angular size and very high brightness temperatures, pulsars are unique probes to study the ionized interstellar medium (IISM).

1.2 Interstellar Medium (ISM)

Interstellar medium is the matter that exists in the space between the stars in our Milk Way Galaxy [1]. ISM usually contains interstellar matter, relativistic charged particles known as cosmic rays, and magnetic fields. Interstellar matter includes gas (99%) in molecular, neutral atomic, and ionized form and dust (tiny solid particles, 1%). My thesis will focus on the ionized form. Of the gas in the Milky Way, 90% by mass is hydrogen, with the remainder mostly helium. These three basic constituents (interstellar matter, cosmic rays and magnetic fields) have comparable pressures and are intimately coupled together by electromagnetic forces [45].

The ISM is only a small fraction of the total mass of the Galaxy, and it does not shine in the sky as visibly and brightly as stars do, but it plays a vital role in many of the physical and chemical processes taking place in the Galactic ecosystem, such as the cycle of matter from the ISM to stars and back to the ISM. A good knowledge of the dynamics, energetics, and chemistry of the ISM helps us understand the present-day properties of our Galaxy and predict its long-term evolution.

Roughly half the interstellar mass is confined to discrete clouds occupying only ∼1-2 % of the interstellar volume. These interstellar clouds can be divided into three types: the dark clouds made of very cold molecular gas (T ∼ 20 K), the diffuse clouds, which consist of cold atomic gas (T ∼100 K), and the translucent clouds (mix of both cold molecular gas and cold atomic gas). The rest of the interstellar matter, spread out between the clouds, exist in three different forms: warm atomic, warm ionized, and hot ionized (warm $\sim 10^4$ K, hot $\sim 10^6$ K).

Cold molecular (mostly H_2) and cold atomic gas (mostly H I) represent the raw material from which stars can be formed in the disk of the galaxy if they become gravitationally unstable and collapse[47]. Warm atomic gas is also mostly H I with T $\sim 6000 - 1000$ K. Although those clouds do not emit visible radiation, molecular clouds can be detected by their radio and infrared emission and

absorption lines. H I cloud can be detected by H I 21cm emission line wherever it exists. It can be detected in absorption wherever H I absorbs some other more distant radiation and a continuum radio source exists. Pulsars can be detected in HI absorption sometimes when the HI is between the pulsar and the Earth.

Both warm and hot ionized gas are ionized hydrogen (H II), also called plasma. Warm ionized gas is produced when the ultraviolet radiation emitted by hot young stars ionizes surrounding clouds of gas. In warm ionized region, hydrogen is almost fully ionized [45], and it can be observed by its Hα emission (an optical emission at a wavelength of 656 nm) and probed by pulsar dispersion. While in hot ionized region, temperature is much higher so that not only hydrogen but also metals are highly ionized[1]. It is now widely accepted that the hot ionized gas is generated by supernova explosions and, to a lesser extent, by the generally powerful winds from the progenitor stars [46]. Supernova explosions drive rapidly propagating shock waves in the ISM, which sweep out cavities filled with hot rarefied gas and surrounded by a cold dense shell of collapsed interstellar matter[45].

1.3 Interstellar Radio Wave Propagation

The radiation from pulsars passes through the ionized interstellar medium (IISM) before reaching Earth. Free electrons in the ISM directly affects the interstellar radio waves propagation in a few different ways resulting in the phenomena of dispersion, scattering and scintillation. The influence on the pulsar's radiation provides an important probe of the IISM itself [45].

1.3.1 Dispersion

In the ionized ISM the refractive index (n) can be expressed as

$$n = \sqrt{1 - \frac{w_p^2}{w^2}} \tag{1.1}$$

w_p is the plasma frequency which is proportional to $\sqrt{N_e}$, N_e is the electron number

density of the plasma. Phase velocity $V_p = C/n$, C is the light speed. The propagation constant $k = w/V_p = nk_0$. The group velocity $V_g = dw/dk$. In this particular case, $V_g = Cn$, it means that higher frequency radio wave travels faster than lower frequency, the resulting delay in the arrival of pulses at a range of frequencies is directly measurable as the dispersion measure (DM) of the pulsar. The dispersion measure is the total column density of free electrons between the observer and the pulsar.

$$DM = \int_0^D N_e(s)\mathrm{d}s \tag{1.2}$$

Here D is the distance from the pulsar to the observer. Usually pulsar with bigger DM is further away than pulsar with smaller DM, but it's not always true since DM also depends on electron density.

Pulsar signal is a broadband signal, the dispersion in arrival time across the bandwidth of a receiver broadens the pulse profile. Since pulsar duty cycle is typically very small, DM can be roughly estimated by measure the width of broadened pulse.

To recover the emitted pulse profile of a pulsar[48], dispersion has to be removed as the first process of pulsar signal processing. Both coherent and incoherent de-dispersion algorithms can be applied to remove the dispersion effect. Coherent de-dispersion is a linear operation, it requires more calculation but it can remove it completely while incoherent de-dispersion uses filter bank to remove group delay between different channel in a more calculation efficient way. Although the dispersion within each channel can not be removed using incoherent method, satisfactory result can be achieved by using sufficient number of channels in the filter bank.

1.3.2 Scattering

If the IISM had no electron density fluctuations transverse to the line of sight, only dispersion will be observed. However there are transverse fluctuations

in plasma density which modulate the phase of the radio wave. The phase modulations causes angular scattering, The angular scattering causes other phenomena including pulse broadening and intensity scintillation. Scattering and scintillation are our main research interests. They are different observable phenomena but from the same cause. Our research relates those two phenomena and provides a way to reconstruct the underlying scattered image of the pulsar.

Angular Broadening

Radio waves from pulsar are forced to deviate from a straight trajectory when they pass the in-homogenous IISM, which causes an angular broadening phenomena when we observe on the Earth. Since pulsar can be treated as a point source, the fine structure of ionized ISM can be revealed by this broadened pulsar image which we call the pulsar scattered brightness image denoted by $B(\boldsymbol{\theta})$. Because of the frequency dependence of the plasma refractive index Eq 1.1, the angular width of the scattered image varies as wavelength.

Traditionally VLBI interferometry provides the highest angular resolution imaging technique which is limited by diffraction to λ/b over a baseline length b at frequency λ . Because the scattered image is typically smaller than this resolution, it can not normally be resolved by VLBI. Our research uses parabolic arc theory to indirectly construct the scattered brightness image at much finer resolution.

Temporal (Pulse) Broadening

The scattering in IISM causes multi-path interference, each path has a different time delay which leads to temporal broadening in observed individual pulses. For homogeneous scattering most of the signal arrives with a small scattering angle and a small delay, but the more highly scattered radiation leads to an approximately exponential tail.

1.3.3 Scintillation

RISS, DISS and Dynamic Spectrum

Scintillation refers to the intensity fluctuations in observed radio sources caused by propagation from the source to the observer through the turbulent interstellar plasma. There are two scintillation phenomena: diffractive ISS (DISS) and refractive ISS (RISS). DISS is the faster fluctuation (in the scale of minutes and hours) while RISS is relatively slow (in the scale of days or even months). RISS corresponds to larger spatial-scale which makes it possible to analyze larger spatial-scale structure in the IISM, and it is not very sensitive to the size of the radio source (Compact radio sources, such as AGN's and galactic masers, are small enough). DISS, on the other hand, provides a tool to analyze small spatial-scale structure ($<<$ 1AU) in the electron density in ISM, and requires a small radio source as a probe ($<< 10^4 km$ for B0834+06). Pulsars have very small diameter which ensures that they can be considered as an un-resolvable small radio source, and they can display the full range of scintillation and scattering phenomena, and it makes it possible to probe the small spatial-scale structure. Our research focuses on DISS.

DISS is seen in the dynamic spectrum, a two dimensional distribution $I(\nu, t)$. Each point in the dynamic spectrum is obtained by summing over the on-pulse portions of several pulse periods (depends on the time resolution) at time t in one channel spectrometer centered at frequency ν, with the off-pulse portions subtracted. Telescope mean system noise can be removed by subtracting the off-pulse too. RFI usually shows as an increase at constant frequency or at a constant time, i.e. it is either narrow band and not time variable or broad band and short time. So it can often be detected and removed from a dynamic spectrum. Figure 1.1 is the dynamic spectrum of PSR B0834+06 observed at the Arecibo Observatory on 2003 December 31[21]. The flux density as a function of frequency and time is shown using a gray scale that is linear in power, with dark regions indicating high power. The time spans are less than 1 hour and suppress any refractive intensity fluctuations. The dynamic spectrum shows some periodic fringes

in this example, which also shows the phenomenon of diffractive scintillation.

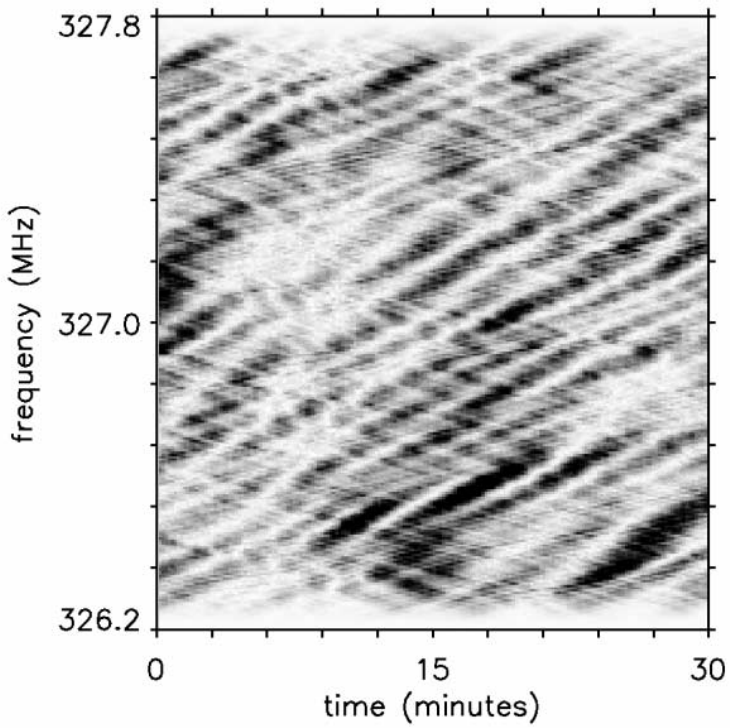

Figure 1.1: Dynamic spectrum example, PSR B0834+06 observed at the Arecivo Observatory on 2003 December 31 [21]

Secondary Spectrum

Secondary Spectrum is the squared amplitude of the two-dimensional Fourier transform, $\tilde{I}(\tau, f_{\mathrm{D}})$, of the dynamic spectra of intensity. Figure 1.2 is the secondary spectrum corresponding to the dynamic spectrum in Figure 1.1 [21]. The gray scale is logarithmic in power. Fringes in the dynamic spectrum appear as discrete features in the secondary spectrum which is due to the interference between pairs of points on the scattering screen, such as shown in Figure 1.3. Delay (τ) is the differential delay between one pair of paths, and differential Doppler frequency, or called fringe frequency (f_{D}), is the difference of the Doppler frequency of each path.

In Figure 1.2, there are some faint but clearly visible power extends away

from the origin in a parabolic pattern, this pattern is called parabolic arc. More details will be discussed in the later section.

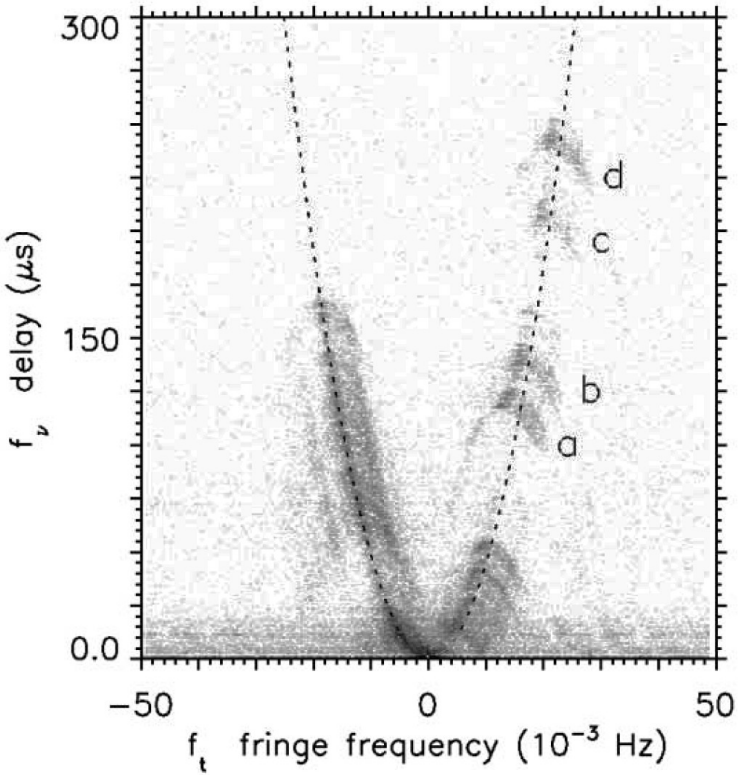

Figure 1.2: Secondary spectrum example [13]

1.3.4 Plasma Turbulence in ISM

Scintillation and scattering have been observed from hundreds of pulsars over forty years since their discovery. These can be adequately explained by propagation through the IISM, modeled as a turbulent plasma with a homogenous isotropic 3D Kolmogorov spectrum of electron density. The resulting 2D scattered brightness image can use the following approximation if the spectrum of the phase fluctuations is Kolmogorov.

$$B(\theta_x, \theta_y) = \frac{C_0}{(1 + (\frac{\theta_x}{\theta_{x0}})^2 + (\frac{\theta_y}{\theta_{y0}})^2)^{11/6}} \tag{1.3}$$

However, inhomogeneity has been observed on different scales in the turbulence, from kiloparsec scales [9] to parsec scale in the local ISM [14] [22], to AU-scale inhomogeneity which is observed from extreme scattering events (ESEs) [18] [23] [33]. There is also evidence that interstellar scattering is not only inhomogeneous but also anisotropic. Anisotropy in the ISS diffraction pattern has been measured indirectly [30] [7]. Such observations give evidence for elongated fine structure in the ISM on scales of thousands of kilometers. All those evidences show the existence of compact (AU-scale) ionized structure in ISM, which we refer as a cloud, whose scattering is inhomogeneous and anisotropic. Such clouds behave as a scattering screen[27] [31] since they are much thinner than the distance between pulsar to the Earth. Because of their small scale, those clouds are still hard to observe directly. In this thesis, we developed a number of algorithms to indirectly construct scattered brightness image showing inhomogeneous anisotropic turbulence.

1.4 Theory of Parabolic Arc

1.4.1 Simple scattering screen theory

The parabolic arc phenomenon discovered by Stinebring [35] provides a powerful tool to probe ionized clouds. Theory of parabolic arcs is based on the assumption that scattering is dominated by a single local scattering region which is very thin compared with the distance from the pulsar to the Earth. This assumption is called simple scattering screen theory and thin region is called scattering screen. Figure 1.3 shows the geometry of pulsar and scattering screen, and all scattering models and their corresponding algorithms in this thesis are based on simple screen. This figure demonstrates the scattering screen bends two radio waves from the same pulsar and they arrive on Earth with different angles (θ_1 and θ_2) and interfere at the telescope.

Based on the geometry in Figure1.3, Equations 3.1 [13] shows the interference relationship between differential delay, differential Doppler frequency and θ_1 and θ_2.

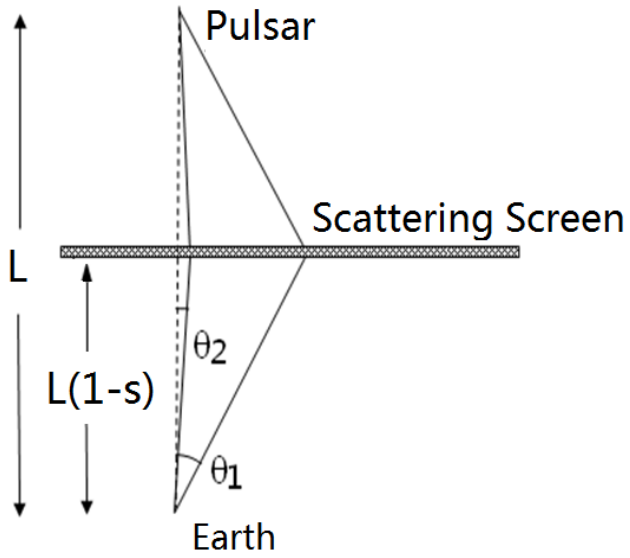

Figure 1.3: Geometry of pulsar and scattering screen

$$f_D = \frac{(\boldsymbol{\theta}_1 - \boldsymbol{\theta}_2) \cdot \boldsymbol{V}_{eff}}{\lambda} \tag{1.4}$$

$$\tau = \frac{(\theta_1^2 - \theta_2^2) D_{eff}}{2c} \tag{1.5}$$

Where $\boldsymbol{V}_{eff}$ is effective velocity which is a combination of velocity of pulsar, Earth and screen, D_{eff} is the effective distance which counts in both the distance of pulsar and screen to Earth. When the interference is between the bright center ($\theta_2 = 0$) and an essentially linear scattered image, then τ is a quadratic function of f_D, this type of interference produces a primary parabolic arc.

$$\tau = \frac{\lambda^2 D_{eff}}{2c {V_{eff}}^2 \cos^2 \alpha} f_D^2 \tag{1.6}$$

Where α is the angle between this linear image and effective velocity. When the interference is between a bright offset spot (at θ_2) and the linear core image, then a reversed parabolic arc with the same curvature is produced.

$$\tau = -\frac{\lambda^2 D_{eff}}{2c {V_{eff}}^2 \cos^2 \alpha} (f_D - f_{D0})^2 + \tau_0 \tag{1.7}$$

Where (f_{D0} τ_0) corresponds to the bright offset spot at θ_2.

1.4.2 Observed Parabolic Arc

Observing bright pulsar with high dynamic range provided by big telescope, sometimes parabolic arc can be seen in the secondary spectrum. The curvature depends on the frequency, pulsar and scattering screen. Parabolic arcs are are seen most clearly when the scattered image is essentially linear. If SNR is high enough, some reversed arclets, called sub-arcs, are visible too. They have the same curvature with apexes lie along or close to the main parabolic arc. In Figure 1.2, the parabolic arc's curvature η is $0.47s^3$ shown with a dashed line. There are four isolated reversed sub-arc labeled a-d on the positive doppler side. Here we also call the main parabolic the forward parabolic arc. Forward parabolic arcs are due to the interference between the entire outer part of the scattered image and the bright un-scattered emission at the origin, while sub-arcs are due to the interference between outer bright point and the core scattered image. More details of parabolic arcs will be discussed in chapter 2.

1.5 Content of thesis

Chapter 2 is a paper published by Brisken et al, (2010), I am a co-author on that paper. Walter Brisken and Adam Deller arranged the observations, recorded the data and correlated it, and my advisors (Barney Rickett and William Coles) and I did all imaging and data analysis on those data. In this paper, we used astrometry on the dynamic visibility spectrum observed by a VLBI network to successfully map the scattered brightness astrometrically with much higher resolution than the diffractive limit of the interferometer. We employ this technique to measure an extremely anisotropic scattered image of the pulsar B0834+06 at 327 MHz. We find that the scattering occurs in a compact region about 420 pc from the Earth. This image has two components, both essentially linear and nearly parallel. The primary feature is highly modulated on spatial scales as small as 0.05 AU. The second feature is much fainter and is displaced from the axis of the

primary feature by about 9 AU. We find that the velocity of the scattering plasma is 16 ± 10 km s^{-1}approximately parallel to the axis of the linear feature. However, the core scattered image is unclear which makes it impossible to estimate of the axial ratio of the plasma turbulence. And only scattering positions are determined, no brightness estimation is achieved.

In chapter 3, a new technique is used which allows reconstruction of the core scattered image in two dimensions, providing a way to estimate of the axial ratio of the anisotropic turbulence. This technique relies on the assumption that the offset source is point source, and it uses the modeling of sub-arcs in secondary spectrum, which originates from the interference between an offset bright point in the scattered image and the core. The algorithm was tested using simulated data that confirms its operation and examines how the size of offset bright point can affect the reconstruction of the core image. Using the ensemble-averaging model, we obtained a 2-D core image, and successfully estimated the half power width in both parallel and perpendicular direction (~ 3.85 mas and ~ 1.3 mas respectively) with axial ratio ~ 3.

Chapter 4 is based on the result from [41], which is the decomposed scattered waves' components: amplitude $|\tilde{\mu_j}|$, Doppler shift f_{Dj} and delay τ_j, we develop a direct relationship between (f_{Dj}, τ_j) and the apparent positions $\boldsymbol{\theta}$ of the scattered waves to reconstruct the scattered image. However, it can't resolve the position ambiguity since there is no phase information in the result of [41]. With the assistance of the estimated axis angle from astrometry in chapter 2, and the knowledge that two ambiguities are symmetric to the velocity axis, we flipped some part of the brightness image along the velocity axis and got another estimate of the scattered image, except the center part which is partially unresolved. This work is based on the same pulsar but a different dataset, which is 22 months earlier than the main dataset in all other chapters.

From all those techniques we find that the features in the scattered image

are highly elongated. In chapter 5, an alternative is considered as a 1-dimensional straight-line brightness distribution and its modified curvi-line distribution are introduced to model this scattered image. Based on those models, both primary feature and 1ms feature are analyzed and converted from secondary spectrum domain back to brightness distribution in both parallel $\theta_{\parallel}$ and perpendicular $\theta_{\perp}$ direction. Algorithms are developed for the steepest gradient fitting and a modified version of 'clean' method to estimate brightness and $\theta_{\perp}$. We get a well-estimated one dimensional brightness image of the primary feature with $\theta_{\perp}$ fluctuation. And we found that two straight-line linear model can better describe the offset feature, we also found that offset feature is frequency dependent.

In chapter 6, the overall conclusion of this research and possible physical explanation of this scattered image are covered. We summarize all the properties of our reconstructed brightness image. Based on estimated scattered brightness and its properties, we came up with two possible geometry models for physical plasma turbulence, Parallel geometry model and orthogonal geometry model, and conclude that the orthogonal model fits our observation better than the parallel model.

Chapter 2

100 μas resolution VLBI imaging of anisotropic interstellar interstellar scattering toward pulsar B0834+06

W. F. Brisken, J.-P. Macquart, J. J. Gao, B. J. Rickett, W. A. Coles, A. T. Deller, S. J. Tingay, C.J.West

This is the reprint of published paper [2]

2.1 Abstract

We have invented a novel technique to measure the radio image of a pulsar scattered by the interstellar plasma with 0.1 mas resolution. We extend the "secondary spectrum" analysis of parabolic arcs by Stinebring et al. (2001) to very long baseline interferometry and, when the scattering is anisotropic, we are able to map the scattered brightness astrometrically with much higher resolution than the diffractive limit of the interferometer. We employ this technique to measure an extremely anisotropic scattered image of the pulsar B0834+06 at 327 MHz. We

find that the scattering occurs in a compact region about 420 pc from the Earth. This image has two components, both essentially linear and nearly parallel. The primary feature, which is about 16 AU long and less than 0.5 AU in width, is highly inhomogeneous on spatial scales as small as 0.05 AU. The second feature is much fainter and is displaced from the axis of the primary feature by about 9 AU. We find that the velocity of the scattering plasma is 16 ± 10 km s^{-1}approximately parallel to the axis of the linear feature. The origin of the observed anisotropy is unclear and we discuss two very different models. It could be, as has been assumed in earlier work, that the turbulence on spatial scales of ($\sim$ 1000 km) is homogeneous but anisotropic. However it may be that the turbulence on these scales is homogeneous and isotropic but the anisotropy is produced by highly elongated (filamentary) inhomogeneities of scale 0.05-16 AU.

2.2 Introduction

Radio pulsars provide a powerful tool for studying the ionized interstellar medium. The dispersion in their pulse arrival times probes the mean electron density. Their very small diameters ensure that they display the full range of scintillation and scattering phenomena, which probe the fine spatial structure in the electron density. Their pulse amplitudes exhibit a combination of diffractive and refractive intensity scintillation on times from seconds to months. Compact emission from some bright active galactic nuclei can also show scintillation on times of hours to months, albeit smoothed by the effect of their larger angular diameters. The large body of pulsar scintillation data has been interpreted in terms of homogeneous isotropic Kolmogorov turbulence in the interstellar plasma [3]. See reviews by [28, 26].

However, a litany of observational evidence now points to the existence of compact ionized structures in the interstellar medium (ISM) whose scattering characteristics are well beyond those of such homogeneous isotropic Kolmogorov turbulence. In particular the scattering is seldom uniformly distributed along the line of sight. It is often dominated by one local region somewhere in the line of

sight, which we refer to as a "thin screen." Although it is unlikely to resemble a screen, it is thin with respect to the total line of sight from the source to the observer [27, 31]. Inhomogeneity in the turbulence is required on kiloparsec scales to explain how the level of pulsar scattering varies with distance and Galactic coordinates [9]. Inhomogeneity is also required on the parsec scale in the local ISM to explain the intermittent nature of the scintillation observed in a few quasars on hour-long time scales [14, 22].

In addition, evidence for AU-scale inhomogeneity in the turbulence comes from extreme scattering events (ESEs), which are observed in a few quasars as rare, large (10 to 50%) variations in flux density over several weeks [18, 23, 33]. These are generally seen as a decrease in flux density attributed to the passage across the line of sight of an ionized cloud which either scatters [18] or refracts [32] the radiation.

In recent years there has also been increasing evidence that interstellar scattering (ISS) is not only inhomogeneous but also anisotropic. The most direct measure of anisotropy is through very long baseline interferometry (VLBI) imaging of scattered brightness, but it is only detectable on a few heavily scattered lines of sight [17]. Anisotropy in the ISS diffraction pattern has also been measured indirectly [30, 14, 7, 4]. Such observations give evidence for elongated fine structure in the ISM on scales of thousands of kilometers, suggesting anisotropic magneto-hydrodynamic turbulence controlled by the magnetic field as discussed by [19] and [34].

The examples cited above show departures from both homogeneity and isotropy in the ionized ISM. It is possible, but by no means proven, that the various phenomena have a common origin in a population of AU-scale anisotropic regions of enhanced density and turbulence which we here generically refer to as "clouds." However, we note that such localized clouds must contain fine scale substructure that causes scattering at radio frequencies. Such a population of clouds presents a serious puzzle. Their number density must be many orders of magnitude greater than that of stars and their implied electron densities $n_{\rm e} \gtrsim 10$ cm^{-3} are much higher than expected in pressure equilibrium in the warm ionized phase ISM [32].

The discovery of parabolic arcs in the ISS of pulsars by [35] has added a powerful new tool for probing such clouds. Many pulsars exhibit parabolic arcs in their secondary spectra (SS), which is the power spectrum (versus delay and Doppler frequency) of the dynamic spectrum of intensity (versus frequency and time). The arcs are sometimes narrow (in delay) which implies scattering by a thin layer. The distribution of power in the SS often reveals anisotropic scattering and in some cases there are discrete downwards facing "arclets," which also imply scattering from isolated anisotropic clouds ("cloudlets"). See [13, 38] for interpretation of the arcs.

The SS allows a two dimensional reconstruction of the scattered image from observations at a single receiver, since each point in the SS isolates the scintillation power associated with interference between pairs of points on the scattering disk. However the reconstruction can be model dependent and has an inherent two-fold ambiguity [13, 37]. Occasionally one can also see isolated peaks in the SS corresponding to narrow bandwidth fringes in the dynamic spectrum [40, 29]. Such fringes result from interference between the normal primary (on-axis) scattering disk and the off-axis discrete cloud.

Recent results from [21] have compounded the difficulties in understanding the nature of the underlying ionized clouds. They observed the SS towards pulsar B0834+06 and found four distinct arclets scattered through 7 to 12 mas which they interpreted as originating from $\sim$0.2 AU clouds requiring $n_{\rm e} > 100$ cm^{-3}, similar to those invoked to explain ESEs towards quasars. By monitoring the evolution of structures in the secondary spectrum, they followed these clouds over three weeks and showed that they co-moved with the rest of the scattering material.

In this paper we report VLBI observations of the scintillation from the same pulsar (B0834+06) in order to further investigate these clouds. We have developed a novel astrometry technique that makes use of SS-like quantities derived from the interferometer visibilities. Using these "secondary cross spectra" (defined in Table2.3), we can accurately localize points on the scattering screen corresponding to high signal-to-noise pixels of the SS. We use the results of the astrometry of many such points to measure the distance and velocity of the interstellar clouds

and so define a precise model for the scattering. Applying this precise model to the astrometric image with the scattering model allows us to eliminate all the otherwise troublesome ambiguities and validates the model. We then use this precise model to recover the scattered image with even greater angular resolution from the secondary spectrum itself. In our observations the Rayleigh resolution (i.e., synthesized beam) of the VLBI array is about 35 mas, the astrometric precision is about 1 mas, and structure in the scattered image recovered by modeling is found on a scale of 100 μas.

2.3 Observations and Primary Analysis

Pulsar B0834+06 was observed as part of a global VLBI project on 2005 November 12. To obtain the greatest astrometric precision we used four of the largest telescopes in the global VLBI network: Arecibo (AO); the Green Bank Telescope (GBT); Jodrell Bank (JB); and tied-array Westerbork (WB). We used a somewhat lower frequency than most secondary spectrum observations (327 MHz) in order to obtain higher angular scattering and thus to better resolve the image with astrometry. Baseband data were recorded using the Mark5A disc recorders at all antennas. Four dual circular polarization 8 MHz bands spanning the frequency range 310.5 to 342.5 MHz were recorded with four-level quantization, yielding a total data rate of 256 Mbps per antenna. In order to minimize unwanted signals that may correlate between stations, the pulse calibration signals were disabled at all of the antennas. A total of 5700 s of on-source data were recorded.

An initial correlation was performed using the VLBA correlator in Socorro, NM with typical continuum VLBI spectral and temporal resolutions. These correlator products were used for delay and bandpass determination. The raw data were recorrelated at Swinburne University with the DiFX software correlator [15], whose flexibility enabled the data to be processed with extremely high spectral resolution. The output visibilities consisting of 32768 spectral channels per 8 MHz band (244 Hz resolution) were dumped every pulse period (1.25 s). The software correlator used incoherent dedispersion to apply a 125 ms wide on-pulse bin; both

the on- and off-pulse visibilities were recorded. The timing information from which the gate ephemeris was derived was determined through simultaneous pulsar timing observations made at the GBT.

Dynamic spectra were constructed from the autocorrelation spectra generated by the correlator for each polarization. In an analogous manner, *dynamic cross spectra* were formed from the cross correlation spectra (visibilities). In the case of the power spectra the off-pulse spectra were subtracted from the on-pulse spectra, removing the telescope system noise and most radio frequency interference (RFI). This was not necessary in forming clean dynamic cross spectra because the noise and RFI are not correlated between any two antennas. Both the dynamic spectra and the dynamic cross spectra were averaged into 5-pulse time blocks to reduce the effect of the strong pulse-to-pulse intensity fluctuations. The total power in each 8 MHz band was constrained to be constant, a reasonable condition considering that 8 MHz is much wider than the diffractive scintillation bandwidth, measured here as $\delta\nu \sim 3$ kHz, which we note is considerably narrower than 38 kHz from [8]. This process will suppress any refractive intensity fluctuations, however these would have a time scale of many days.

The instrumental bandpasses were corrected using interferometric observations of a strong background source. Delay, phase and amplitude calibration were derived from the observations of the target source itself using the coarsely averaged visibility data from the VLBA correlator. Since this applies *self-calibration*, the astrometric positions which we determine below are all referenced to the centroid of the intensity. After calibration, the two circular polarizations were summed to form the Stokes parameter I in order to maximize the signal to noise ratio, giving the dynamic spectra of total intensity, $I(f,t)$, for each antenna, and visibility, $V(f,t,\mathbf{b})$, for each baseline $\mathbf{b}$.

2.3.1 Secondary Spectrum Analysis and Arcs

The secondary spectra, $A(\tau, f_{\rm D})$, are squared amplitudes of the two dimensional Fourier transforms, $\tilde{I}(\tau, f_{\rm D})$, of the dynamic spectra of intensity. Here the transform variables conjugate to frequency, f, and time, t, are delay, τ, and

Doppler frequency, $f_{\rm D}$, respectively. The quantity $\tilde{V}(\tau, f_{\rm D}, \mathbf{b})$ represents the complex two-dimensional Fourier transforms of the complex dynamic cross spectra. As some of the quantities we discuss in this work have not yet been introduced in the literature, we summarize in Table 2.1 the conventions we adopt throughout for the various products derived from the correlator auto and cross correlations.

The dynamic spectra have a spectral resolution of 244 Hz over 8 MHz and temporal resolution of 6.25 s (about 5 pulsar rotation periods) over the observation duration of 6500 s, which are well-suited to resolving the diffractive scintillation, whose time scale is ~ 1 min and frequency scale is ~ 3 kHz. Thus the secondary spectra have a resolution of 125 ns in delay out to a maximum of 2.05 ms. They have resolution in Doppler frequency of 0.15 mHz over a width of $\pm$ 80 mHz. Custom software was used for this and all subsequent data processing.

For the first time, dynamic spectra of right minus left circular polarization and the corresponding secondary spectra were computed to test for differential Faraday rotation in the ISM [25]. No detectable signal, significant at the 0.1% level, was found in any of these differenced spectra. In a simple model this implies rotation measure differences across the image of less than $\sim 1.2 \times 10^{-3}$ rad m^{-2} on AU scales [25].

The amplitude of the quantity $\tilde{V}(\tau, f_{\rm D}, \mathbf{b})\ \tilde{V}(-\tau, -f_{\rm D}, \mathbf{b})$ is plotted in Figure 2.1. This quantity is a generalization of the secondary spectrum to the interferometric case and will be discussed later. The plot extends to a delay of 2 ms, which is considerably greater than has been published before, and is plotted with higher Doppler frequency and delay resolution than is usual. It thus reveals some interesting features. It is composed of a dense forest of fine arclets in which the apex of each arclet lies on or near the upwards facing main arc and all arcs are parabolic with the same curvature, as shown by [21]. The disjoint group of arclets near 1 ms in delay with negative Doppler frequency is particularly striking and will be referred to as the 1 ms feature. Their apexes lie inside the main arc and, as we find below, they form a separate and distinct part of the scattered image. Some faint arclets on the positive Doppler frequency side can be identified with delays as high as 2 ms, although they are not readily visible in this figure.

Table 2.1: Definitions of various products derived from the measured intensities and visibilities used throughout this text. In the definitions for the first two quantities, E is the electric field as measured by the antenna receiver and the angle brackets denote a time average over the measurement interval much longer than the inverse bandwidth.

Term	Symbol	Remarks
Correlator products (2nd order in electric field)		
Dynamic spectrum	$I(f,t) = \langle \lvert E(f,t)\rvert^2 \rangle$	the power of the electric field as a function of frequency and time
Dynamic cross spectrum	$V(f,t,\mathbf{b}) = \langle E_1(f,t) E_2^*(f,t) \rangle$	the visibilities measured on a baseline $\mathbf{b}$ as a function of freq and time
Intermediate quantities (2nd order in electric field)		
–	$\tilde{I}(\tau, f_D) = \mathrm{FT}\left[I(f,t)\right]$	the Fourier transform of the dynamic spectrum
–	$\tilde{V}(\tau, f_D, \mathbf{b}) = \mathrm{FT}\left[V(f,t,\mathbf{b})\right]$	the Fourier transform of dynamic cross spectrum
Derived quantities (4th order in electric field)		
Secondary spectrum	$A(\tau, f_D) = \lvert\tilde{I}(\tau, f_D)\rvert^2$	the squared-modulus of the Fourier transform of the dynamic spectrum
Secondary cross spectrum	$C(\tau, f_D, \mathbf{b}) = \tilde{V}(\tau, f_D, \mathbf{b})\tilde{V}(-\tau, -f_D, \mathbf{b})$	the (complex) product of $\tilde{V}(\tau, f_D, \mathbf{b})$ and its corresponding quantity at the point $(-\tau, -f_D)$

2.4 Theory of Secondary Cross Spectra

Here we briefly outline the theory of the arcs and refer the reader to [38] and [13] for more complete analyses. Points distributed along the main parabolic arc are due to interference between a highly scattered component at $\boldsymbol{\theta}$ and the components arising from near the pulsar brightness centroid at $\boldsymbol{\theta} = 0$. In this case there is a differential delay $\tau = \theta^2 D_{\mathrm{eff}}/2c$ and differential Doppler frequency[1] $f_{\mathrm{D}} = \mathbf{V}_{\mathrm{eff}} \cdot \boldsymbol{\theta}_{/} \lambda$. Here D_{eff} and $\mathbf{V}_{\mathrm{eff}}$ are the effective distance and velocity vector of the scattering screen as defined in §2.5, and λ is the observed wavelength. If the scattered image is essentially linear, through the origin at angle α with respect to

[1]Henceforth these terms will be abbreviated to delay and Doppler.

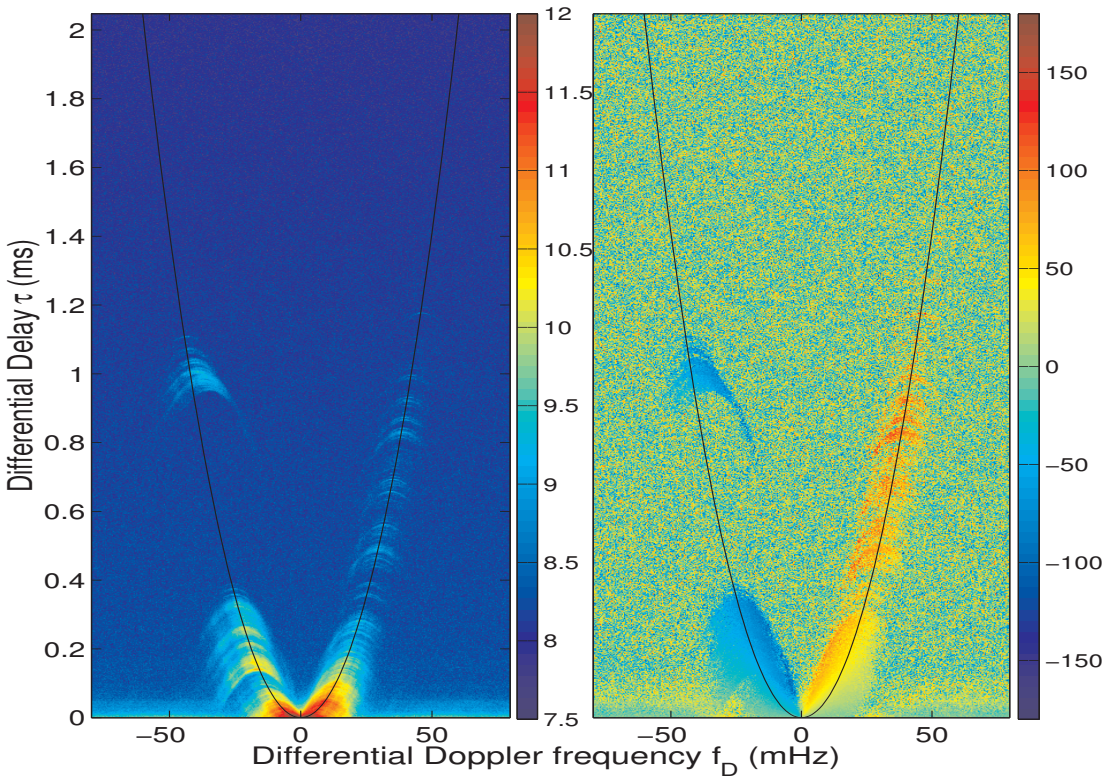

Figure 2.1: The amplitude (left) and phase (right) of the secondary cross spectrum C, defined in Table2.1, for the 8 MHz wide 314.5 MHz sub-band on the AO-GBT baseline. Amplitude scale is $\log_{10}$ and phase is in degrees For display purposes only, both diagrams have been smoothed over 5 pixels in delay to reduce the noise, giving plotted resolution of 0.44 mHz in Doppler frequency and 3.1 μs in delay. The black line is a parabola with curvature 0.56 s^3 on both panels. There are bright arclets in amplitude that extend along the ridge of this main parabola to delays > 1 ms. The phase appears much smoother, as discussed in §2.4.1.

$\mathbf{V}_{\rm eff}$, we can eliminate θ and obtain

$$\tau = a f_{\rm D}^2\,, \text{ where } a = D_{\rm eff}\lambda^2/(2cV_{\rm eff}^2\cos^2\alpha) \tag{2.1}$$

as the equation of the main parabola. Note that $a \propto \lambda^2$ regardless of the wavelength scaling of scattering angle θ, as confirmed experimentally by [20].

To understand the interferometric observations consider the pulsar as a point source at a distance $D_{\rm p}$ from Earth, whose radiation is scattered by an inhomogeneous region of ionized interstellar medium at a distance $D_{\rm s}$ from Earth.

In this thin-screen approximation the phasor due to radiation scattered at a point $\mathbf{x}_j = D_\mathrm{s}\boldsymbol{\theta}_j$ in the screen suffers a phase delay ϕ_j due to the scattering plasma and is received with a total phase delay $\Phi_j(\mathbf{r}) = \phi_j + k(\mathbf{x}_j - \beta\mathbf{r})^2/2\beta D_\mathrm{s}$ where $\beta = 1 - D_\mathrm{s}/D_\mathrm{p}$ and $\mathbf{r}$ is the transverse position of the receiving antenna. The received electric field is the summation of all such scattered components, either expressed by the Fresnel diffraction integral [13] or approximated by a summation over all stationary phase points [38], in strong scattering.

Here we use the stationary phase approximation to obtain the correlation of the fields between antennas at locations $-\mathbf{b}/2$ and $\mathbf{b}/2$. This defines the visibility whose Fourier transform in time and frequency can be written as:

$$\begin{aligned}\tilde{V}(\tau, f_\mathrm{D}, \mathbf{b}) &= \sum_{j,k} \exp[i(\Phi_j(-\mathbf{b}/2) - \Phi_k(\mathbf{b}/2))] \\ &\times \mu_j\mu_k\delta(f_\mathrm{D} - f_{\mathrm{D},jk})\delta(\tau - \tau_{jk}). \end{aligned} \tag{2.2}$$

where:

$$f_{\mathrm{D},jk} = \frac{1}{\lambda}(\boldsymbol{\theta}_j - \boldsymbol{\theta}_k)\cdot\mathbf{V}_\mathrm{eff}, \tag{2.3a}$$

$$\tau_{jk} = \frac{D_\mathrm{s}}{2\,c\,\beta}(\theta_j^2 - \theta_k^2) + \left[\frac{\phi_j}{2\pi\nu} - \frac{\phi_k}{2\pi\nu}\right]. \tag{2.3b}$$

The δ functions in equation (2.2) determine how each particular point on the secondary spectrum is related to a pair of points in the screen. With finite bandwidth and observing time the δ functions should be replaced by finite narrow sinc functions. The equation sums over all possible pairs of stationary phase points in the screen, with μ_j, μ_k as the magnifications determined by phase curvature of each point [38]. In the full Fresnel formulation, the summation becomes a double two-dimensional integration over the screen with all $\mu = 1$. The plasma delay term in square brackets in equation (2.3b) involving ϕ_j is unimportant compared to the first term when constructing secondary spectra in strong scintillation, but in any case this term cancels in the astrometry discussed below.

In either formulation equations (2.3a) and (2.3b) connect the points on the scattering screen to τ, f_D in the secondary spectrum and are independent of $\mathbf{r}$. Note that f_D can be understood as the differential Doppler shift between two

waves scattered at differing points on the screen [13] and that the delay τ is the differential group delay evaluated at the center of the observing band.

Each arclet arises due to the interference of radiation from a given fixed point on the scattering screen with scattered radiation from $\boldsymbol{\theta}_{\sim}0$. Examination of the delay in equation (2.3b) shows that for a strong contribution from fixed θ_j the greatest delay (i.e., arclet apex) will be where θ_k goes through zero. The particular shape of each of the arclets reflects the scattered brightness distribution near core of the image. Furthermore the fact that the SS amplitude is bright over a *narrow* range in delay shows that the points comprising the bright emission centroid region are extended along a line rather than in a circular halo [13, 38].

The velocity of the scintillation pattern across the line of sight is $\mathbf{V}_{\rm ISS} = (1-\beta)\mathbf{V}_{\rm p}+\beta\mathbf{V}_{\oplus}-\mathbf{V}_{\rm s}$, where $\mathbf{V}_{\rm s}$, $\mathbf{V}_{\oplus}$ and $\mathbf{V}_{\rm p}$ are the velocities of the screen, Earth and pulsar respectively [10]. The scintillation velocity is dominated by the pulsar, whose proper motion [24] combined with a distance of 643 pc (estimated from the dispersion measure using the NE2001 Galactic electron distribution model of [12]) gives $V_{{\rm p},\alpha} = 6.1^{+15}_{-15}$ km s^{-1}, $V_{{\rm p},\delta} = 156^{+15}_{-18}$ km s^{-1}; note that these velocity errors do not include the substantial uncertainties in the pulsar distance.

2.4.1 Astrometric Imaging

In single dish observations information on the scattered image is limited to the power in the secondary spectrum, obtained from $\tilde{I}(\tau, f_{\rm D})$. However, the addition of interferometric observations permits high-precision astrometry to be performed on each component of the secondary cross spectrum, which isolates the wavefield due to a single pair of interfering waves. By applying astrometry to each such pair individually, we can recover an apparent image of the scattered pulsar radiation.

For a particular pixel from $\tilde{V}(\tau, f_{\rm D}, \mathbf{b})$ equation (2.2) sums over all pairs of points that satisfy equations (2.3). However, we now consider the case that only one pair of points satisfies the latter conditions, a condition that is valid for a linear or sufficiently anisotropic source. Then the phase of $\tilde{V}$ is $\Phi_{j,k} = \Phi_j(-\mathbf{b}/2) - \Phi_k(\mathbf{b}/2)$

is

$$\Phi_{j,k} = \phi_j - \phi_k + \frac{kD_\mathrm{s}}{2\beta}[\theta_j^2 - \theta_k^2 + \frac{\beta \mathbf{b}}{D_\mathrm{s}} \cdot (\boldsymbol{\theta}_j + \boldsymbol{\theta}_k)] \tag{2.4}$$

which has terms that are symmetric and anti-symmetric in scattered points j, k. We cancel the anti-symmetric terms by summing the phase of $\tilde{V}$ at each point (f_D, τ) and its conjugate point at $(-f_\mathrm{D}, -\tau)$. This eliminates the random screen phase leaving the symmetric part of the phase as

$$\psi_{j,k}(\mathbf{b}) = \Phi_{j,k} + \Phi_{k,j} = \frac{2\pi}{\lambda} \mathbf{b} \cdot (\boldsymbol{\theta}_j + \boldsymbol{\theta}_k)\,, \tag{2.5}$$

which neatly encodes the average position of the two scattering points projected parallel to the baseline $\mathbf{b}$. As we show below, the scattering is indeed highly anisotropic and the assumption of a single pair of interfering waves for each pixel is well justified.

In practice the anti-symmetric phases are cancelled by first forming the secondary cross spectrum, defined as

$$C(f_\mathrm{D}, \tau, \mathbf{b}) = \tilde{V}(f_\mathrm{D}, \tau, \mathbf{b}) \tilde{V}(-f_\mathrm{D}, -\tau, \mathbf{b})\,, \tag{2.6}$$

for all non-negative values of τ. Subsequently, the resultant complex phasors are averaged over small regions (3 pixels in Doppler by 5 in delay) in order to reduce the effect of noise before the argument is determined:

$$\psi(\mathbf{b}) = \arg\left(\langle C(f_\mathrm{D}, \tau, \mathbf{b}) \rangle\right)\,. \tag{2.7}$$

Here $\langle\rangle$ denotes the 3 by 5 averaging which properly weights the complex products before the phase is computed. The result is the geometric phase of the secondary cross spectrum sampled with a resolution of 0.63 μs in delay and 0.44 mHz in Doppler. As with any phase measurement the result is modulo 2π.

The right panel of Figure 2.1 shows ψ, the phase of the secondary cross spectrum, for the baseline from GBT to AO. In contrast to the sharply defined arclets in the amplitude plot, the phase is relatively smooth, appearing continuous between the arclets, as might be expected if the fine structure in amplitude comes from a continuous image with fine structure in brightness. Consequently we can use astrometry from ψ to actually map out the scattered brightness distribution

with remarkable precision. Furthermore we can measure the position angle of the axis of elongation and estimate both the distance to the region of scattering and its velocity.

We can use equation (2.5) to find $(\boldsymbol{\theta}_j + \boldsymbol{\theta}_k)$ for any point in the secondary cross spectrum if it is dominated by a *single pair* $(\boldsymbol{\theta}_j, \boldsymbol{\theta}_k)$ and there are at least two baselines with sufficient signal-to-noise ratio (S/N). However if we can identify the apex of an arclet we know $\boldsymbol{\theta}_j$ or $\boldsymbol{\theta}_k$ is zero, so we have a unique solution for the remaining angle. The amplitude plot in Figure 2.1 shows that the apexes of the identifiable arclets lie near the parabolic curve shown as a line. Hence we sampled the secondary cross spectrum along that curve to approximate a set of apex positions even where the arclets are too densely spaced to be identified individually. We defined the main parabolic arc by the curvature $a = 5.577 \times 10^{16}/f^2$ (s^3) for center frequency f Hz in each of our four sub-bands, as shown by the black line in Figure 2.1.

We selected data with a high enough S/N to estimate $\boldsymbol{\theta}$ as follows. For each of the six baselines we found the phasor $\langle C(f_\mathrm{D}, \tau, \mathbf{b})\rangle$ and defined S as the S/N relative to the root mean square value of $|\langle C\rangle|$ in a low power (noise dominated) region near the point being examined. Samples with delays within ± 0.6 μs of the main parabola were selected if $S > 4$ on the GBT-AO baseline and if $S > 3$ on the WB-AO baseline.

For each sample of $\langle C\rangle$ we first formed a "dirty image" from the 6 baselines in the same sense as for traditional synthesis imaging [36]. At the dirty image maximum a two-dimensional Gaussian was fit to determine a position, and both S and the shape of the Gaussian were used to assign positional uncertainties. However, since C is a product of two visibilities this method gave too much relative weight to the high S/N baselines and led to apparent positional errors much smaller than the scatter of the points from neighbouring samples along the main arc. In addition there are lobe ambiguities in the synthesized beam, since two of four antennas (JB and WB) are relatively close to each other and so probe nearly the same spatial frequencies. The result is a dirty beam that is nearly doubly periodic with lattice vectors $\mathbf{a}_1 = (59.0, -61.9)$ mas and $\mathbf{a}_2 = (34.2, 17.8)$ mas at 322.5 MHz

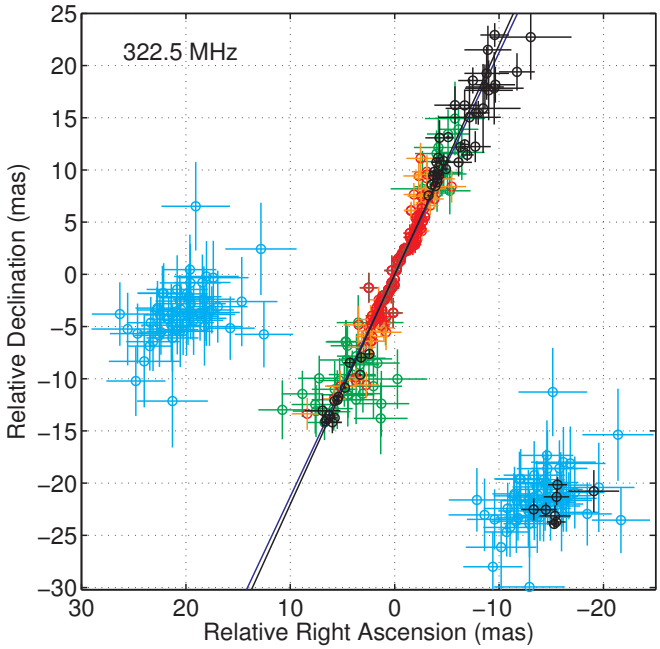

Figure 2.2: Map of the astrometric positions of the scattered radiation from samples along the main parabola in the sub-band at 322.5 MHz plotted as error bars in colors of green, orange, red & dark red, for amplitude, $|C|$, increasing by factors of 10. Right ascension and declination values are relative to the centroid position as determined by VLBI self-calibration. Note the increase of astrometric errors with decreasing amplitude $|C|$. The blue straight line is an unweighted fit to these points. The black error bars are from the apexes of identified arclets and the black line is a fit to these points. Samples from the 1 ms feature (negative Doppler and delay > 0.9 ms) are shown by cyan points for two possible lobe choices. As discussed in §2.5 the correct lobe position is at the lower right. This is overplotted with black error bars from the apexes of individual identified arclets near 1 ms.

(scaling linearly with wavelength).

After some investigation we adopted a simpler astrometric method based on a weighted linear least squares fit of the observed phases, ψ, using equation (2.5) (with one of the angles set to zero). Under conditions of high S/N one can show that the phase error is $\propto 1/\sqrt{S}$ and so we used weights $\propto \sqrt{S}$. Because the phase is observed modulo 2π there are ambiguities in position, corresponding to the lobe ambiguities. Consequently, we used a first guess position as an initial model and wrapped the phase (e.g., on the trans-Atlantic baselines) to be within $\pm\pi$ of that

solution before applying the least squares fit. For the points from the main arc our first guess was at the origin and the results are plotted as error bars (in a pale color) in Figure 2.2. Points from the main arc form a continuous elongated image close enough to the origin that the phase ambiguity is not a problem for them.

An empirically determined line passing through arclet apexes was used to sample the points in the SS associated with the 1 ms feature. The astrometry of these points, however, forms a distinct group offset from the origin in celestial coordinates, making it difficult to resolve the phase ambiguities. Accordingly, we used first guess positions from the two closest synthesized beam lobes which are roughly equidistant from the origin. The cyan points on the left show the fitted positions starting from the central lobe; the cyan points on the right show them starting from a position lobe-shifted by the lattice vector $-\mathbf{a}_2$, which corresponds to the addition of 2π to the phase on the transatlantic baselines. In §2.5 we discuss the resolution of this ambiguity in favor of the right hand position.

The major conclusion from Figure 2.2 is that the scattered image from the main arc is remarkably extended along a straight line with very few points more than 2σ from that line. As noted above highly anisotropic scattering was already inferred by the emptiness of the secondary spectrum (particularly the absence of power at $f_D \sim 0$, $\tau > 0$) and the many discrete arclets. The apparent flaring of the points away from the origin is due to the increasing size of the error bars because the SS amplitude decreases with angle of scattering. We define the straight line fitted to the points as the "scattering axis". Note that the plot is not a proper image of the scattered brightness, since the amplitude $|C|$ must be transformed by a Jacobian into the brightness. Hence the axial ratio is not easily estimated and we postpone the discussion of it to a later section.

2.4.2 Arclet Apex Astrometry

The astrometric positions discussed in the preceding section and plotted in Figure 2.2 are based on the assumption that samples along the main arc correspond to the apexes of an underlying arclet. However this is not always true, as is obvious in the 1 ms feature. So we have made an effort to identify all the discrete arclets,

estimate the apex of each in an optimal way, and then map the phases at each apex to an angular position. At 322.5 MHz we found 62 well defined arclets (with apex delays $\tau > 0.1$ ms) of which 7 are in the 1 ms feature. At smaller delays the arclets are too crowded to identify separately.

We formed a template by averaging all the arclet amplitudes, centered by their apex, and we fitted a straight line in phase versus $f_{\rm D}$ to the template to obtain the phase gradient versus $f_{\rm D}$ in the template. We then fitted the amplitude and phase templates to each arclet using a weighted least squares fit. Hence we obtained estimates for the delay, Doppler, phase, and amplitude at the apex and errors in all four parameters. We then estimated $\boldsymbol{\theta}$ and its error at each apex and repeated the procedure for all 4 sub-bands.

The astrometric positions and errors of the 62 arclets are plotted in black in Figure 2.2. The error bars are smaller than from the main arc because the phases were determined from a weighted average of the phases over the entire arclet. In addition the scatter should be smaller because they are known to correspond to interference with the bright centroid component at the origin. However, the lobe uncertainty in the location of the 7 arclets from the 1 ms feature remains. As we discuss below, we resolve the ambiguity in favor of the lower right lobe position marked by the black error bars derived from the 7 apexes. The apexes near the main arc have positions extending out to 20 mas from the origin and show good linear alignment with the inner points from the main arc. A straight line fitted to the inner main arc has a position angle of $-25.2 \pm 0.5^\circ$ (east of the declination axis)[2]. We use this axis to define $\theta_\parallel$ and define $\theta_\perp$ by a 90° clockwise rotation from it.

We have used three techniques to resolve the lobe ambiguity. The first relies on the frequency dependence of the positions obtained from each arclet apex. As discussed below in §2.4.3 we find that the angular positions of the scattered features that cause the arclets are essentially independent of frequency. Thus we can use the fact that the correct lobe choice should give a position that is independent of frequency. We computed the 2 dimensional mean for the 1 ms apexes from

[2]Here and elsewhere in this paper, reported uncertainties are 68% confidence intervals.

a weighted average position of its imaged points separately for each of the four sub-bands. For the lobe position at a negative RA offset in Figure 2.2 the mean position was independent of frequency within the errors of estimation (~ 0.1 mas). All other lobe choices show systematic frequency dependence in their positions in agreement with that expected for a lobe error.

Confirmation comes from two further tests. The second technique relies on equation (2.3b) relating delay to the angular offset of an arclet apex and is discussed in §2.5.1. Similarly, the third technique relies on equation (2.3a) for the Doppler frequency and is discussed in §2.5.2.

2.4.3 Frequency Scaling

[21] found the wavelength scaling of the apex Doppler frequencies of the four arclets which they identified in pulsar B0834+06 to scale $\propto \lambda^{-1}$. Hence using equation (2.3a) they concluded that the scattering angle responsible for the arclet was independent of wavelength. We have done a similar analysis on the apex Doppler frequencies of all the identified arclets in our four sub-bands. In addition we analyzed the wavelength scaling of the apex delay in the four sub-bands, which is $\propto \theta^2$ as in equation (2.3b). We combined the fits to estimate a single scaling parameter γ where $\theta \propto \lambda^{\gamma}$. We estimated γ separately for three groups of apexes and tabulate the values in Table 2.2.

Table 2.2: Wavelength-scaling exponents, γ, in the scattering angles ($\theta \propto \lambda^{\gamma}$) estimated from apex positions for three groups of arclets.

Arclet apex group	γ
$\tau \sim 1$ ms $f_{\rm D} < 0$	0.062 ± 0.006
$0.1 \lesssim \tau \lesssim 0.4$ ms	0.01 ± 0.01
$\tau > 0.4$ ms $f_{\rm D} > 0$	0.019 ± 0.004

The results show that the scattering responsible for each arclet originates at a location that is essentially independent of wavelength across the 10% range spanned by the four sub-bands. This is entirely incompatible with the value $\gamma = 2$, to be expected if the individual arclets came from separate ray paths caused by refraction due to differing gradients in the column density of electrons. The

conclusion applies to all arclets in the SS, with the possible exception for the 1 ms feature whose position scales weakly $\lambda^{0.06}$. Such a weak scaling might apply if the arclet were caused by a lens-like concentration of plasma, such as that invoked by [32] to explain ESEs, but with a transverse extent very much smaller than than its distance from the direct path.

2.5 Scattering Model

We now develop a model for the distance and velocity for the various features in the scattered image.

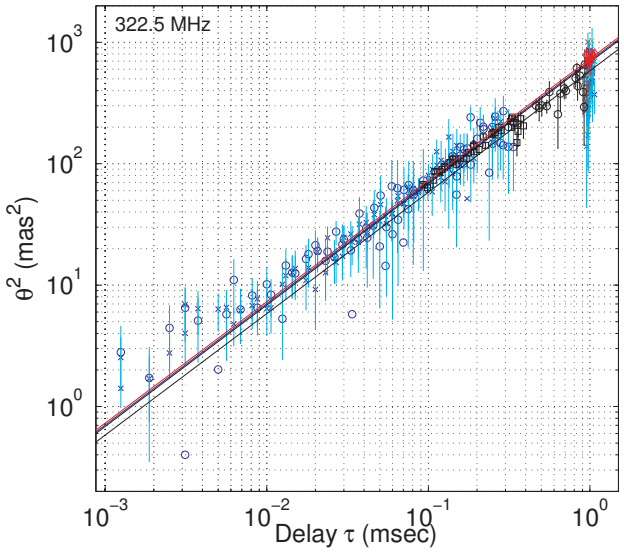

Figure 2.3: θ^2 versus delay. Points from the main arc in Figure 2.2 are shown as blue $\times$ ($f_D > 0$) and $\circ$ ($f_D < 0$); the apexes of the identified arclets are plotted in black, except for those from the 1 ms feature which are in red. The straight line models ($\theta^2 = m\tau$; see equation(2.8)) were fitted separately to various subsets of the points to estimate their distances.

2.5.1 Scattering Distance Estimation

Equation (2.3b) relates delay τ to the angular offset θ for an arclet apex, for which the second angular component is at the origin. Thus:

$$\tau = (D_{\rm eff}/2c)\theta^2 \tag{2.8}$$

where

$$D_{\rm eff} = D_{\rm p}(1-\beta)/\beta \tag{2.9}$$

In Figure 2.3 we plot on logarithmic scales θ^2 from the astrometry against delay with the various groups of data from Figure 2.2. Note that there is a bias to θ^2 due to the uncertainties in right ascension and declination. Since we have estimates of those uncertainties we subtracted the bias before fitting.

Table 2.3: Effective Distances and Velocities estimation from the VLBI astrometry

Main Parabolic Arc				
Frequency	D_{eff}(pc)		V_{eff}(km s^{-1})	
MHz	Inner Arc	$\tau \sim 1ms$	$V_{eff\,\parallel}$	$V_{eff\,\perp}$
314.5	1197± 23	1350 ±65	303.3±3.1	-131.9±6.4
322.5	1175 ± 24	1272 ± 29	300.7 ± 3.3	-151.5 ±11
330.5	1195 ± 29	1294 ± 20	303.3 ± 3.7	-161.5 ± 16
338.5	1133 ± 18	1287 ± 24	300.0 ± 2.5	-133.8 ± 5.0
326.5	1175 ± 29	1301 ± 40	301.8 ± 3.2	-144.7 ± 12
Apexes of Identified Arclets				
Frequency	D_{eff}(pc)			V_{eff}(km s^{-1})	
MHz	$\tau \lesssim 0.4$ ms	$\tau > 0.4$ ms	$\tau \sim 1ms$	$V_{eff\,\parallel}$	$V_{eff\,\perp}$
314.5	1165 ± 19	1370 ± 43	1064 ± 63	305.9 ± 2.9	-136.1 ± 4.4
322.5	1205 ± 19	1419 ± 67	1132 ± 24	313.4 ± 2.5	-152.9 ± 3.7
330.5	1162 ± 17	1406 ± 39	1180 ± 110	306.8 ± 2.3	-158.4 ± 11
338.5	1139 ± 15	1315 ± 67	1107 ± 17	305.4 ± 2.4	-134.9 ± 1.8
326.5	1168 ± 23	1378 ± 60	1121 ± 59	307.9 ± 3.3	-145.6 ± 8.6

Two separate straight lines through the origin were fitted to the (blue) points sampled along the main parabola and from the 1 ms feature. The apex points were also fitted separately for three regions: for apex delays less than 0.4 ms, delays bigger than 0.4 ms with positive Doppler and with negative Doppler (i.e., the 1 ms feature). The fits were weighted proportional to the reciprocal of the

standard deviation in θ^2. The derived effective distances are given in Table2.3 with their formal 1σ errors for all 4 sub-bands.

The simplest model puts all of the scattering in a single relatively thin region at the same effective distance. Comparing $D_{\rm eff}$ for the differing regions of the SS, we find $D_{\rm eff}$ in the range 1100 to 1400 pc. Since we found no significant scaling of the apex θ with frequency (see §2.4.3), we combine data from all four sub-bands to create a combined estimate shown as a fifth row in the table. We note that there is a possible contribution to inconsistencies among the sub-bands from a partial narrowing of the two outer sub-bands at AO by a front-end bandpass filter.

The average of the estimates in column 2 from delays less than 0.4 ms from both the main arc and from the arclet apexes is 1171 ± 23 pc. In column 4 the 1 ms cluster gives 1301 ± 40 pc, which overlaps at $\pm 2\sigma$ with the value 1121 ± 59 pc obtained from the 1 ms apexes. This small discrepancy appears in Figure 2.2 as an offset in the centroid of the blue and black points. Since the arclet apexes have been specifically identified so that one of the $\boldsymbol{\theta}$ parameters can confidently be set to zero and since $D_{\rm eff}$ for the 1 ms apexes is within 1σ of those from the main arc, we conclude that the scattering region responsible the 1 ms feature is located at the same distance as that causing the main arc. Without the lobe-shift a fit for $D_{\rm eff}$ gives values from 1700 to 2600 pc. The large discrepancy in this distance provides the second confirmation of the lobe-shift for the 1 ms points.

A possibly significant difference is seen between the apexes with positive Doppler and delays > 0.4 ms in column 3, which give a significantly larger $D_{\rm eff} = 1378 \pm 60$ pc. Whereas all of the sub-bands give a larger distance there are only a few identified arclets in each sub-band and they are of relatively low S/N in all 4 sub-bands so that accurate correction for the noise bias to θ^2 becomes more critical. Thus the evidence is relatively weak for a different distance for these points at large delay and positive Doppler.

We now take $D_{\rm eff} = 1171$ pc, combined with the pulsar distance of 640 pc in equation (2.9) to obtain the fractional scattering distance $\beta = 0.353 \pm 0.005$. This is consistent within 2σ of the value of 0.29 ± 0.04 obtained by [21] using the

same pulsar distance but without the advantage of knowing the full geometry of the scattering screen. However, its true uncertainty is dominated by uncertainty in the pulsar distance which is estimated from the dispersion measure. Dispersion measure distances are notoriously unreliable, especially for nearby pulsars and thus are only accurate to $\sim 40\%$ [6]; this gives a screen distance range of 250 to 580 pc from the Earth.

2.5.2 Velocity Estimation

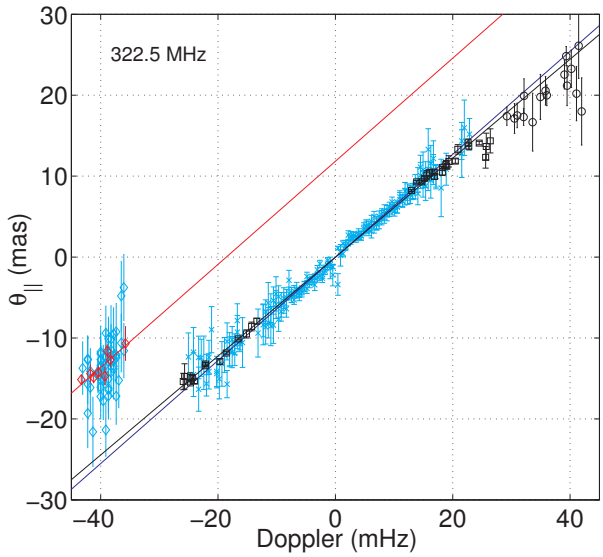

Figure 2.4: $\theta_\parallel$ plotted against the Doppler f_D for the sub-band at 322.5 MHz. Points plotted with cyan $\times$ marks are sampled from the inner main arc in Figure 2.2 and from a line through the 1 ms feature. Black points are from apexes of identified arclets, except 1 ms apexes which are red.

An independent analysis is provided by equation (2.3a), relating the Doppler frequency for the arclet apexes to their astrometric position. At each apex the Doppler frequency can be written as:

$$\begin{aligned} f_\mathrm{D} &= \boldsymbol{\theta}.\mathbf{V}_\mathrm{eff}/\lambda \\ &= (\theta_\parallel V_{\mathrm{eff}\parallel} + \theta_\perp V_{\mathrm{eff}\perp})/\lambda. \end{aligned} \tag{2.10}$$

where

$$\mathbf{V}_{\rm eff} = \mathbf{V}_{\rm ISS}/\beta \approx \mathbf{V}_{\rm p}(1-\beta)/\beta. \tag{2.11}$$

The final approximation ignores the velocities of the Earth and of the screen relative to that of the pulsar. Then the ratio $V_{\rm eff}/D_{\rm eff}$ estimates the pulsar proper motion independent of its distance and of β. However, here we do not make that approximation but use the measured proper motion to estimate the velocity of the scattering screen.

In Figure 2.4 we plot $\theta_\parallel$ against $f_{\rm D}$ which would give a straight line whose slope gives an estimate of $\lambda/V_{\rm eff\parallel}$, providing that the value of $\theta_\perp V_{\rm eff\perp}$ were the same or negligible for all points. As shown in Figure 2.2 the points fitted by the straight line have small $\theta_\perp$ scattered about zero. Hence we were able to estimate $V_{\rm eff\parallel}$ from the various groups of points and tabulate the results in Table2.3 excluding all the points with delays > 0.4 ms.

If we combine inner apex fits with values from the main arc we obtain $V_{\rm eff\parallel} = 305 \pm 3$ km s^{-1}. We now assume the same $V_{\rm eff\parallel}$ to apply to the 1 ms apexes and since these points have a significant measured $\theta_\perp$ we can fit for the perpendicular velocity also, obtaining $V_{\rm eff\perp} = -145 \pm 9$ km s^{-1}.

In summary the scattering model provides three observable parameters which we list in Table 2.4. We can express the velocities in RA, Dec and relate them to the measured pulsar proper motion velocity $V_{{\rm p},\alpha} = 6.1$ km s^{-1}, $V_{{\rm p},\delta} = 156$ km s^{-1}. The derived model parameters are also listed in the table. Equation (2.11) relates the measured effective velocity to the scintillation velocity $\mathbf{V}_{\rm ISS}$ which also depends on the transverse projected velocity of the Earth and the scattering screen. Using the pulsar velocity cited above gives an estimate of the ISM screen velocity relative to the Sun (~ 16 km s^{-1}), which is comparable in magnitude to other measured interstellar velocities.

The ISM velocity analysis provides the third confirmation of the lobe-shift applied to the 1 ms astrometry, since in the alternate position $V_{\rm eff\perp}$ is reversed and could only be reconciled with the pulsar velocity if there were an implausibly high velocity (> 200 km s^{-1}) for the scattering screen relative to the Sun.

Table 2.4: Model Parameters for Distance and Velocity, assuming $\beta = 0.353$. Note that the first five quantities are measured; the others are calculated from these assuming the pulsar distance and velocity as cited in the text.

Model Parameters	Value	Unit
$D_{\rm eff}$	1171 ± 23	pc
$V_{\rm eff\parallel}$	305 ± 3	km s^{-1}
$V_{\rm eff\perp}$	-145 ± 9	km s^{-1}
$\parallel$ Scattering axis	-25.2 ± 0.5	deg. east of north
$\perp$ Scattering axis	-115.2 ± 0.5	deg. east of north
$D_{\rm s}^{a}$	415 ± 5	pc
$V_{\rm s\parallel}^{b}$	-16 ± 10	km s^{-1}
$V_{\rm s\perp}$	0.5 ± 10	km s^{-1}
α	27 ± 2	deg.

[a] Assumes $D_{\rm p} = 640$ pc; the error in $D_{\rm s}$ due to the uncertainty in $D_{\rm p}$ is much larger $\sim 40\%$

[b] Including errors from uncertainty in pulsar distance and proper motion

2.5.3 Estimating the Image Center

In the discussion so far we have assumed that the astrometry is correctly centered on the emission centroid. However, since the scattered image is highly anisotropic, the centering done by self-calibration in the primary analysis would have been more precise in the perpendicular direction than in the parallel direction. Close examination of the initial versions of the plots as in Figures 2.3 and 2.4 revealed small but significant asymmetries, which allowed us to improve the centering in the parallel direction.

In the Doppler plot of Figure 2.4 a straight line fit did not pass exactly through the origin and this fitted offset in $\theta_{\parallel}$ was found to be on the order of 0.5 mas differing slightly between sub-bands. In the delay plot of Figure 2.3 the θ^2 values at a given delay with positive Doppler frequencies were systematically shifted relative to those with negative Doppler frequencies. We were able to minimize the χ^2 for the straight line by fitting for a positional offset in the parallel direction. We found that in each sub-band the optimum parallel offsets were consistent between the Doppler and delay estimation methods within their errors. An average of these two offsets was consequently applied to the astrometry in each sub-band before the

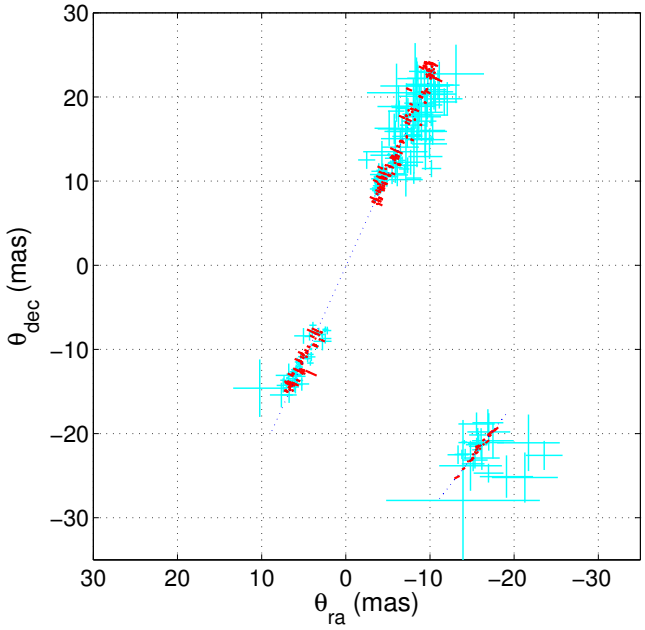

Figure 2.5: Cyan error bars are the VLBI astrometry of the apexes of the identified arclets superimposed from all 4 sub-bands. Red error boxes show the much finer precision of the back-mapped astrometry, as explained in §2.5.4 and clearly delineate the highly linear scattering from both the main arc and the 1 ms feature (at lower right).

analysis described in the two foregoing sections.

2.5.4 Astrometry Mapped Back from the Secondary Spectrum

The synthesized beam size of our VLBI array (its basic angular resolution) was about 35 mas at 327 MHz. In the astrometry shown in Figure 2.2 we obtain positional accuracies as small as ±0.5 mas near the center of the image due to the high signal to noise ratio and much larger errors away from the center. However we can do even better from the apex positions of the arclets in the SS using equations (2.8) and (2.10), which we will refer to as "back-mapping". This is possible since we used the VLBI astrometry to obtain accurate values for the model parameters $D_{\rm eff}$, $\mathbf{V}_{\rm eff}$, and α. The equations give the magnitude of θ from the delay τ and the

component θ_V parallel to $\mathbf{V}_{\rm ISS}$ from $f_{\rm D}$. There is an inherent ambiguity in such a mapping since it does not determine the sign of the angular coordinate orthogonal to the velocity. However, we can use the VLBI image to resolve that ambiguity and show the positions of each apex mapped back into in RA, Dec in Figure 2.5 overplotted for the 4 sub-bands. The mapped astrometry points are plotted as red error boxes on a background of the error bars of the VBLI positions. The apex points mapped back in this fashion extend along the same axis as the VLBI positions but with a narrower spread in $\theta_\perp$ due to their even smaller errors.

With errors $\delta\tau$ and $\delta f_{\rm D}$ in the apex positions we get positional errors $\delta\theta \sim c\,\delta\tau/(D_{\rm eff}\theta)$ and $\delta\theta_V \sim \delta f_{\rm D}\lambda/V_{\rm eff}$. With $\delta\tau \sim 1$ μs we obtain $\delta\theta \sim \theta_{\rm mas}^{-1}$, i.e., 0.05 mas at $\theta_{\rm mas} = 20$ mas, which improves on the 0.5 mas from astrometry, particularly at large scattering angles where the S/N worsens; and with $\delta f_{\rm D} \sim$ 1 mHz the resolution $\delta\theta_V \sim 0.6$ mas. The resulting confidence region is shown by the red box which is narrow in radial θ coordinate and wide in the transverse direction.

The map emphasizes the remarkable anisotropy of the scattering disk and also shows evidence that the 1 ms feature is also highly extended along a roughly parallel direction. This is an important aspect that will constrain any physical model for the scattering.

2.5.5 Scattered Brightness Function

The scattered brightness distribution can be recovered from the secondary spectrum if the intensity scintillations are weak, or if they are highly anisotropic [13]. In this case the scintillations are highly anisotropic and we can make one-dimensional, strip integrated brightness distributions, $B_1(\theta_\parallel)$, by strip integrating the two dimensional distribution over $\theta_\perp$. Then we have

$$B_1(\theta_1)B_1(\theta_2) = A(\tau, f_{\rm D})|J| \tag{2.12}$$

where $\tau = (\theta_1^2 - \theta_2^2)D_{\rm eff}/2c$, and $f_{\rm D} = (\theta_1 - \theta_2)V_{\rm eff}\cos\alpha/\lambda$ and the Jacobian $|J| = f_{\rm D}D_{\rm eff}/c$. Then by sampling $A(\tau, f_{\rm D})$ along the main arc where $\theta_2 = 0$, we can estimate $B_1(\theta)$. This estimate is plotted in Figure 6 without the 1 ms feature,

which cannot be represented on this plot since it is not on the main parabola.

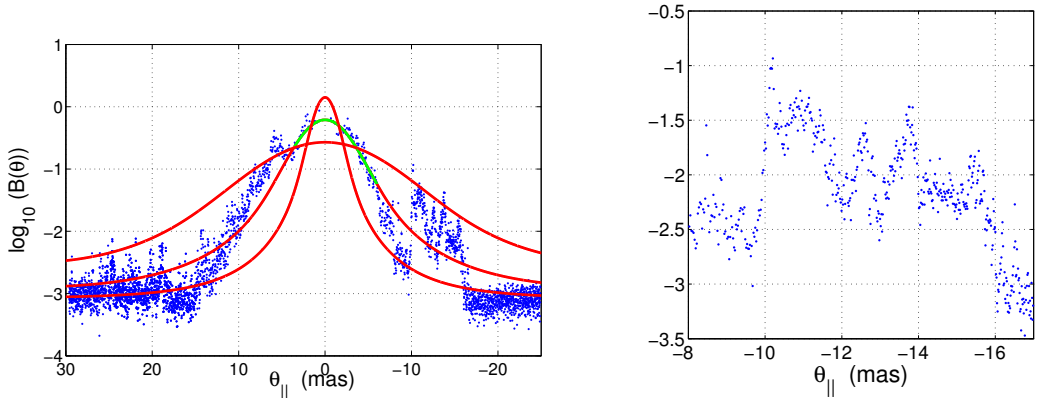

Figure 2.6: *Left:*Scattered brightness against $\theta_\parallel$ obtained for points along the main arc via the back-mapped astrometry in §2.5.4, averaged from all four sub-bands (blue). The individual peaks are as narrow as 0.1 mas as shown in the expanded view in the *right* panel. The three overplotted theoretical curves (red) are for a one-dimensional Kolmogorov model. The middle curve was fitted to the observations over the range shown in green. The other two curves have the same total flux density for the pulsar but are wider and narrower as discussed in the text.

If the scattering comes from homogeneous anisotropic Kolmogorov turbulence then the strip integrated brightness distribution is the Fourier transform of the one-dimensional correlation function of the electric field, $B_1(\theta_\parallel)$ = FT $[\exp(-(s_\parallel/s_0)^{5/3})]$. We have plotted three such models over the observations in Figure 2.6, each with a different value of s_0, the coherence scale of the electric field. The middle model fits the data near the origin ($s_0 \sim 10^4$ km) and the other two give a rough estimate of the range of s_0 necessary to match the measurements. They correspond to changing the root mean square (RMS) electron density by a factor of 2 (wider curve) or 0.5 (narrower curve). One can see in the expanded view on the right that near $\theta_\parallel$ = -10 mas there is a change in the RMS electron density by a factor of 4 in a very small distance.

The finest structure has an angular scale of about 0.1 mas, which corresponds to 0.05 AU. This plot can also be made using the VLBI astrometric $\theta_\parallel$. In this case the large scale structure is the same but the small scale structures seen clearly in Figure 2.6 are smoothed out by the larger error bars in the VLBI

astrometry.

2.5.6 Axial Ratio

While we have clear evidence for highly anisotropic scattering, it is difficult to estimate the axial ratio R, which is usually defined by a contour at, say, half power in the two-dimensional scattered brightness distribution. Estimates of the width in $\theta_\parallel$ can be made from the one-dimensional brightness in Figure 2.6. However, the width at the same level in $\theta_\perp$ is harder to estimate, since we have no information on brightness versus $\theta_\perp$. As an alternative, we can define an apparent axial ratio $R_{\rm ap}$ from the scatter of the points in Figure 2.2 independent of their brightness. Here we define $R_{\rm ap}$ as the ratio of the RMS width in $\theta_\perp$ to that in $\theta_\parallel$. The observed scatter in $\theta_\perp$ will of course be broadened by the astrometric errors, so that only an upper bound can be found on $\theta_\perp$ due to interstellar scattering.

We apply these ideas to Figure 2.7, which shows the astrometry from the main arc as a scatter plot of $\theta_\perp$ against $\theta_\parallel$ superimposed from all four sub-bands. The black error bars show $\theta_\perp$ averaged into 0.5 mas bins in $\theta_\parallel$ where the length of the bar is the standard deviation in each average. Taken as a group the black points from the inner ± 5 mas are consistent with a Gaussian distribution with zero mean and 0.38 mas RMS; there are no points more than $\pm 2\sigma$ from zero and their error bars, which have not been corrected for the measurement error, have a mean value of 0.3 mas. Thus the true scatter in $\theta_\perp$ is smaller than these errors, implying an intrinsic perpendicular RMS width less than ~ 0.3 mas. Taking the half width at half power in $\theta_\parallel$ to be 3 mas from Figure 2.6 gives a lower bound on the axial ratio $R \gtrsim 10$. Similar estimates can be made from the ratios of the parallel to the perpendicular RMS widths of the apex astrometry from both the VLBI and back-mapping methods. These yield $R_{\rm ap} \gtrsim 27$ and $R_{\rm ap} \gtrsim 20$, respectively.

The scattering axis is neither parallel nor perpendicular to the Galactic plane. However, according to the Virginia Tech Spectral-Line Survey[3] the pulsar lies $\sim 1^\circ$ from a 5° long bright Hα filament at a position angle within about 10° of our scattering axis. Although there is a rough agreement in position angle we

[3]See `http://www.phys.vt.edu/halpha/` for more information about this survey.

have no other evidence to support an association with our 30 mas long filament.

2.6 Physical Models of the Scattering

While our main focus is the presentation of the remarkable results found from the observations, we now briefly consider what physical structures could be responsible for the scattering. Following previous analyses of the ISS phenomena, we assume that the basic cause is scattering by random (presumably turbulent) structures in the plasma density. The scale of such turbulence must extend down to well below the diffractive scale, $\sim \lambda/2\pi\theta_{\|}$. To obtain scattering angles of 25 mas requires microstructure of the order of 1000 km. However, the turbulence is inhomogeneous over scales of 0.1 to 10 AU as mentioned above and we must also account for the highly elongated shape of the main scattered image.

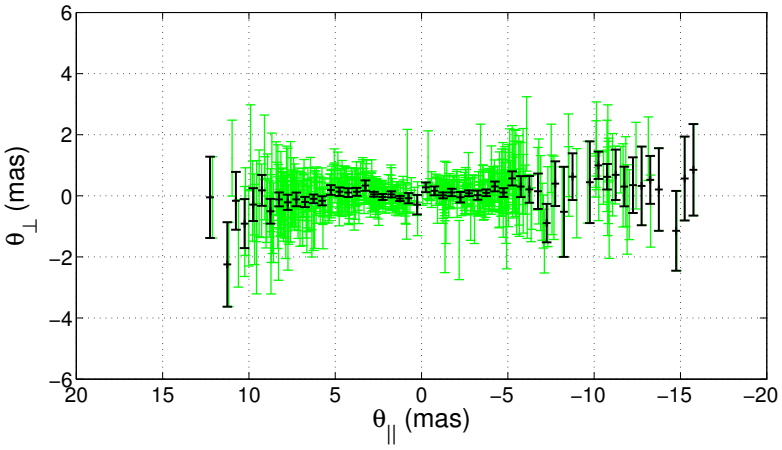

Figure 2.7: Astrometry referred to axes parallel and perpendicular to the main scattering axis. Pale color superimposes scatter plots from the main arc in all four sub-bands. The black points show the average $\theta_{\perp}$ from bins 0.5 mas wide in $\theta_{\|}$ with vertical bars giving the error in the average. The bars have not been corrected for the astrometric errors. Note that only the inner portion of the primary scattering disk where high S/N points are located is included in this plot.

First we ask whether the peaks in our scattered image, due to the arclets, could be the equivalent of "speckles". Discrete arclets are visible in the simulated secondary spectrum in Figure 11 of Cordes et al. (2006), who computed the SS

for a realization of a layer with a Kolmogorov spectrum and an axial ratio 4:1 parallel to the simulated velocity. That figure shows very many fine arclets with apexes centered on a pronounced forward parabola. In independent realizations the arclet apexes appear at random locations, showing that they are the equivalent of speckles in a snapshot scattered image through a turbulent scattering layer. Thus they do not map to deterministic structures in the layer.

In contrast the discrete nature of the arclets and their sparser distribution in our observation suggests deflection by discrete structures, possibly similar to those responsible for extreme scattering events (ESEs). The two basic models proposed for ESEs have been an enhancement in $n_{\rm e}$ that causes a diverging "lens" [32] or an enhancement in plasma turbulence that causes extra scattering [18]. The result that the angle of arrival from the arclets is essentially independent of frequency implies that the waves are deflected at a fixed transverse distance from the pulsar line-of-sight by either refraction or scattering. This reinforces the conclusion that specific isolated structures in the line of sight are responsible. The observed frequency independence constrains the angular size of a lens, based on the law of plasma refraction, to be a small fraction of the angle of deflection which we observe up to ± 20 mas. Similarly the size of a scattering center would have to be much smaller than this angle of deflection.

The very high apparent axial ratio we observe strongly suggests that an ordered magnetic field determines the geometry of the scattering. The lack of any magneto-ionic signature (i.e., the exact match between the dynamic spectra in right and left circular polarizations) implies that the radio frequency phase imposed by the plasma is simply proportional to the column density of the local electron density $n_{\rm e}$. We expect that plasma structures will be more tightly confined transverse to a magnetic field than parallel to it, i.e., the density irregularities will be field-aligned as they are in the solar corona. Since we expect such structures to scatter preferentially in their narrow dimension, our initial idea is that the major axis of the angular scattering would be orthogonal to the mean magnetic field. Thus one scenario for the main image is a roughly parallel set of filaments (or sheets), controlled by a magnetic field at right angles to the axis of scattering and

extending at least over the projected length of the image ($\sim$ 15 AU). Waves passing through a filament are scattered by 10-30 mas due to a locally enhanced column density of electrons (and presumably higher plasma turbulence) which would be seen as a single arclet. We call this first scenario the orthogonal geometry. The axial ratio R would then correspond to the axial ratio of the micro-turbulence (i.e., at the diffractive scale).

There is however, an alternative scenario in which a dense filament of plasma is confined by the local magnetic field, which is parallel to the axis of scattering. We call this the parallel geometry. Such a filament must have denser knots of micro-turbulence, which are responsible for the discrete arclets. The flux ropes seen in the solar wind are a possible plasma structure (see [5] and references therein). The denser knots could scatter isotropically and so the filament would not have to be located exactly in front of the pulsar. In such a case the major axis of the scattered image (about 3 mas) would be determined by diffractive scattering caused by microstructures of the order of 3000 km in scale, but the minor axis would be set by the thickness of the filament. Such scattering has been observed in the solar corona [16] and discussed in the context of interstellar scattering by [11]. We assume that the thickness of such a filament would be of the order of the size of a "knot", on the order of 0.05 AU or 0.1 mas. Thus the filament is at least 16 AU long, about 0.05 AU in diameter, but not straight. The perpendicular RMS angle of 0.4 mas would correspond to an RMS irregularity in the filament of 0.2 AU or 4 times its thickness. Because the scattering is caused by a very thin structure in this model, the electron density in the filament would have to be considerably higher than normally expected (about 5 cm^{-3}) to cause the observed angular scattering.

In the parallel filament model the 1 ms feature is readily explained as a separate offset filament of about the same density which is approximately parallel to the main filament. However, in the orthogonal geometry the observer would not detect the anisotropic scattering from a concentration of filaments nearly parallel to those causing the main arc. Thus the basic simplicity of this geometry, that assumes the scattering is so anisotropic that the angles of scattering are transverse

to the long spatial axis, must be augmented by an independent process of scattering or refraction to explain the 1 ms feature. A possible process is a localized plasma structure in that part of the sight line that refracts the scattered waves towards the observer. In this case the angular position of the 1 ms feature should have a λ^2 wavelength dependence, which is inconsistent with that observed as shown in §2.4.3.

In either geometry the existence of many sub-AU sized discrete structures passing within 15 AU of the line of sight to our pulsar raises the more general question of their distribution in interstellar space. The fact that the structures responsible lie at a common distance suggests that the pulsar happens to lie behind a single larger region consisting a cluster of many filaments of plasma or a single filament with very compact condensations (knots). Further the fact that [21] observed similar arclets 22 months earlier suggests a region bigger than 40 AU. Two ideas that seem possible are a shock with multiple nearly parallel subshocks seems and the flux rope idea already mentioned. The number density of such regions can only be crudely constrained by the sparse statistical sampling of pulsars with similar multiple arclets. We hope to distinguish between these two basic geometries by detailed modeling of the propagation.

2.7 Conclusions

This paper describes a novel VLBI technique resulting in a two-dimensional image of the scattering screen of pulsar B0834+06. The baseband data that were recorded allowed high resolution dynamic spectra to be produced. The secondary spectra produced with the two-hour dynamic spectra could allow sharply defined arclets to be identified with delays as high as 1 ms.

The scattered image was developed by astrometrically mapping points chosen from the secondary spectrum to bright points in the sky plane. These points were clustered in two clearly defined groups: a primary scattering disk which is elongated and inclined $27 \pm 2^\circ$ to the pulsar proper motion direction and a second, non-colinear, feature corresponding to the 1 ms feature of the secondary spectrum.

Diagnostic measurements place the two features at essentially the same distance, 65% of the way to the pulsar. The two-dimensional distribution of points in the scattered image allows both transverse components of the effective velocity to be determined via relationships connecting the Doppler frequency with location in the image.

The discrete feature at 1 ms delay contains about 4% of the total received power. This feature is expected to to be visible only for a few weeks during which time its delay should drift as the pulsar moves; the impact on timing this pulsar at ~ 327 MHz due to such a feature is a time variable wander with magnitude ~ 40 μs. This should come as a caution to those aiming to perform precision pulsar timing at low frequencies on pulsars that exhibit the extreme forms of scintillation that are characteristic of B0834+06. Further, pulsars with sub-microsecond structure may experience apparent pulse profile evolution yielding additional complications in their timing.

We were able to estimate the effective scintillation velocity vector, which depends on a distance-weigthed sum of the velocities of the pulsar, the Earth and the scattering plasma. By using the published proper motion we estimated the velocity of the scattering plasma to be 16 ± 10 km s^{-1}approximately parallel to the scattering axis. Since the errors in this interesting result are dominated by the uncertainty in the pulsar proper motion, we have undertaken a new set of VLBI measurements to improve its precision.

The interpretation of ISS in pulsars has often assumed isotropy in the scattering. The extremely anisotropic scattering found here would substantially alter any quantitative modeling of the plasma were it to be a common feature in other regions on the interstellar medium. A description of the underlying plasma physics must await a resolution of the two possible geometries mentioned in the previous section, but the results and the method provide an exciting new glimpse of the ionized ISM at scales of 0.1 to 10 AU.

Chapter 2, in full, is a reprint of the material as it appears in ApJ 2010. W. F. Brisken, J.-P. Macquart, J. J. Gao, B. J. Rickett, W. A. Coles, A. T. Deller, S. J. Tingay, C. J. West, 2010. The dissertation author was the primary investigator

and author of this paper.

Chapter 3

2-D core image model with point offset source

There are two main models introduced in this chapter to reconstruct core brightness image from reversed sub-arcs. We will refer to these as the instantaneous model and the ensemble-averaging model. In this chapter, two models are represented in details, both simulation and observation data analysis are done. Comparison of those two models' performances are also discussed, and perpendicular width of core image is also estimated. We also estimate the perpendicular width of core image using forward method and compare it with the previous result.

3.1 Reconstruct core image from reversed sub-arcs using the instantaneous model

The algorithm developed in this section was not used in the final interpolation, detailed discussion is in section 3.2.3.

The previous brightness image we achieved is based on the astrometric imaging technique. We successfully determine the positions of offset point sources by finding apexes of reversed sub-arcs, but the brightness of each single point hasn't been estimated. Also, we can't find apex of individual sub-arc when it's close to the

origin since they are overlapped with each other, so the center part is still invisible.

In this chapter, we developed a new technique to reconstruct the entire 2-D brightness distribution of the core from reversed sub-arcs. This idea comes from the weak scattering situation where the primary arc is interference between a single central bright point and an extended source. Detailed theory of brightness image recovery from secondary cross spectra will be presented. The simulation which is used to confirm the theory is also discussed. The simulation result convinces us that the center brightness image can be re-constructed from reversed sub-arcs with little distortion. Then this technique is applied to the observed data and we achieved some satisfying result.

Secondary cross spectrum can be mainly divided into two parts: primary component and reversed sub-arcs. Primary component is due to the interference between the central brightness image and itself. It's hard to recover the center brightness image from primary component because in general each point of Secondary cross spectrum comes from many pairs of scattered waves. Reversed sub-arcs are due to the interference between the central brightness image and a bright offset source (Fig 3.1 shows the Brightness model, the center brightness image is marked as CenterSource and a bright offset source is marked as PointSource, $\boldsymbol{V}_{eff}$ direction is also marked). If we assume that offset source is a point source, then each pixel of a reversed sub-arcs maps mainly from two angular positions in the core brightness, and we can use the amplitude and phase information of that pixel to recover the brightness intensity in those two angular positions. Furthermore, under condition that there are multiple offset sources, each a point source, then the corresponding reversed sub-arcs are identical because they are derived from the same core image. If these reversed sub-arcs do not overlap significantly then making use of all of them can improve the signal to noise ratio in the recovered core image. In the rest of this section, we will focus on the theory of position mapping and brightness intensity reconstruction from reversed sub-arcs to core brightness image.

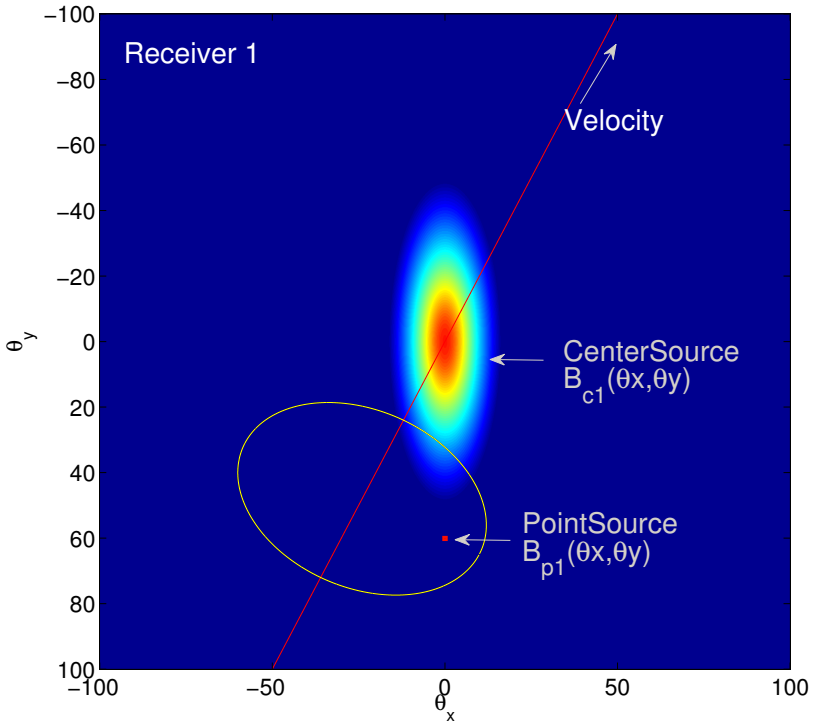

Figure 3.1: Brightness image input, the red line shows the effective velocity direction, the yellow ellipse shows the regions which has four ambiguities, which will be explained later. All unit in angle is *mas*

The secondary cross spectrum is defined as,

$$C(f_D, \tau, \boldsymbol{b}) = \tilde{V}(f_D, \tau, \boldsymbol{b})\tilde{V}(-f_D, -\tau, \boldsymbol{b}) \tag{3.1}$$

$\tilde{V}(f_D, \tau, \boldsymbol{b})$ is the complex two-dimensional Fourier transform of the complex visibility spectrum $V(t, \nu, \boldsymbol{b})$. Each point in secondary cross spectrum is due to interference between pairs of scattered waves at $\boldsymbol{\theta}_1$ and $\boldsymbol{\theta}_2$. Differential delay (τ) and differential Doppler frequency (f_D) are

$$f_D = \frac{(\boldsymbol{\theta}_1 - \boldsymbol{\theta}_2) \cdot \boldsymbol{V}_{\mathit{eff}}}{\lambda} \tag{3.2}$$

$$\tau = \frac{(\theta_1^2 - \theta_2^2) D_{\mathit{eff}}}{2c} \tag{3.3}$$

where

$$\boldsymbol{V}_{\mathit{eff}} = ((1-s)\boldsymbol{V}_P + s\boldsymbol{V}_E - \boldsymbol{V}_{screen})/s \tag{3.4}$$

$$D_{\mathit{eff}} = L(1-s)/s = z_e/s^2 \tag{3.5}$$

Those terms are explained earlier in Chapter 2, just as a reminder, $\boldsymbol{V_P}$, $\boldsymbol{V}_E$ and $\boldsymbol{V}_{screen}$ are velocity of pulsar, Earth and scattering screen. L is the distance between Pulsar and the Earth, s is the ratio of distance between pulsar and scattering screen and distance between pulsar and the Earth. Fourier transform of complex visibility can be expressed in integral form as

$$\begin{aligned}\tilde{V}(\boldsymbol{b},\tau,f_D) = {} & \iiiint g^+(\boldsymbol{\theta}_1,\nu_o)g^{+*}(\boldsymbol{\theta}_2,\nu_o)\exp[-jk(\boldsymbol{b}_1\cdot\boldsymbol{\theta}_1 - \boldsymbol{b}_2\cdot\boldsymbol{\theta}_2)] \\ & \delta(\tau'-\tau)\delta(f'_D - f_D)\mathrm{d}^2\boldsymbol{\theta}_1\,\mathrm{d}^2\boldsymbol{\theta}_2\end{aligned} \tag{3.6}$$

where $g^+(\boldsymbol{\theta},\nu_o)$ is complex angular field spectrum at central frequency ν_o with bandwidth $B << \nu_o$. $g^+(\boldsymbol{\theta},\nu_o)$ doesn't change between two telescopes, it's the same wherever the receiver is. In the rest part of this note, central frequency ν_o is omitted. We define

$$g^+(\boldsymbol{\theta}) \triangleq \varepsilon(\boldsymbol{\theta})\exp[j\phi(\boldsymbol{\theta})] \tag{3.7}$$

$$\begin{aligned}h(\boldsymbol{b},\boldsymbol{\theta}) &\triangleq g^+(\boldsymbol{\theta})\exp[-jk\boldsymbol{b}\cdot\boldsymbol{\theta}] \\ &= \varepsilon(\boldsymbol{\theta})\exp[j\phi(\boldsymbol{\theta}) - jk\boldsymbol{b}\cdot\boldsymbol{\theta}]\end{aligned} \tag{3.8}$$

where $\varepsilon(\boldsymbol{\theta})$ and $\phi(\boldsymbol{\theta})$ represent brightness amplitude and random phase respectively, and $h(\boldsymbol{b},\boldsymbol{\theta})$ includes baseline phase. Eq(3.6) becomes

$$\tilde{V}(\boldsymbol{b},\tau,f_D) = \iiiint h(\boldsymbol{b}_1,\boldsymbol{\theta}_1)h^*(\boldsymbol{b}_2,\boldsymbol{\theta}_2)\delta(\tau'-\tau)\delta(f'_D - f_D)\mathrm{d}^2\boldsymbol{\theta}_1\,\mathrm{d}^2\boldsymbol{\theta}_2 \tag{3.9}$$

And scattered brightness distribution is

$$B(\boldsymbol{\theta}) = |g^+(\boldsymbol{\theta})|^2 = |h(\boldsymbol{b}_1,\boldsymbol{\theta})|^2 = \varepsilon^2(\boldsymbol{\theta}) \tag{3.10}$$

Brightness image can be divided into two components

$$h_1(\boldsymbol{\theta}) \triangleq h_{1c}(\boldsymbol{\theta}) + h_{1p}(\boldsymbol{\theta}) \tag{3.11a}$$

$$h_2(\boldsymbol{\theta}) \triangleq h_{2c}(\boldsymbol{\theta}) + h_{2p}(\boldsymbol{\theta}) \tag{3.11b}$$

'c' stands for center part and 'p' stands for offset part. '1' stands for receiver 1 and '2' stands for receiver 2. There are four terms after putting Equation 3.11a and 3.11b into Equation 3.9. The two self-terms are related with primary component, while the two cross-terms are related with reversed sub-arc. The self-terms will be ignored since we are particularly interested in reversed sub-arc.

$$\begin{aligned}
\tilde{V}(\boldsymbol{b},\tau,f_D) &= \iiiint \{h_{1c}(\boldsymbol{\theta}_1)h^*_{2p}(\boldsymbol{\theta}_2)) + h^*_{2c}(\boldsymbol{\theta}_2)h_{1p}(\boldsymbol{\theta}_1)\} \\
&\quad \delta(\tau'-\tau)\delta(f'_D - f_D)\mathrm{d}\boldsymbol{\theta}_1\,\mathrm{d}\boldsymbol{\theta}_2 \\
&= \underbrace{\iiiint h_{1c}(\boldsymbol{\theta}_1)h^*_{2p}(\boldsymbol{\theta}_2)\delta(\tau'-\tau)\delta(f'_D - f_D)\mathrm{d}\boldsymbol{\theta}_1\,\mathrm{d}\boldsymbol{\theta}_2}_{\tilde{V}_1(\boldsymbol{b},\tau,f_D)} \\
&+ \underbrace{\iiiint h^*_{2c}(\boldsymbol{\theta}_2)h_{1p}(\boldsymbol{\theta}_1)\delta(\tau'-\tau)\delta(f'_D - f_D)\mathrm{d}\boldsymbol{\theta}_1\,\mathrm{d}\boldsymbol{\theta}_2}_{\tilde{V}_2(\boldsymbol{b},\tau,f_D)}
\end{aligned} \tag{3.12}$$

The first term

$$\begin{aligned}
\tilde{V}_1(\boldsymbol{b},\tau,f_D) &= \iiiint h_{1c}(\theta_{1\|_V},\theta_{1\perp_V})h^*_{2p}(\theta_{2\|_V},\theta_{2\perp_V}) \\
&\quad \delta(\tau'-\tau)\delta(f'_D - f_D)\mathrm{d}\theta_{1\|_V}\,\mathrm{d}\theta_{1\perp_V}\,\mathrm{d}\theta_{2\|_V}\,\mathrm{d}\theta_{2\perp_V}
\end{aligned} \tag{3.13}$$

Represent Eq 3.1 in $\|_V$ and $\perp_V$ coordinate. $\|_V$ means its direction is parallel to effective velocity, and $\boldsymbol{V}_{\mathit{eff}} = (V_{\mathit{eff}}, 0) = (V_x, V_y)$.

$$\tau' = ((\theta^2_{1\|_V} + \theta^2_{1\perp_V}) - (\theta^2_{2\|_V} + \theta^2_{2\perp_V}))\frac{D_{\mathit{eff}}}{2c} \tag{3.14}$$

$$f'_D = (\theta_{1\|_V} - \theta_{2\|_V})\frac{V_{\mathit{eff}}}{\lambda} \tag{3.15}$$

By assuming $\theta_{2\|_V}$ and $\theta_{2\perp_V}$ are known and solving variables $\theta_{1\|_V}$ and $\theta_{1\perp_V}$, we get

$$\theta_{1\|_V} = f'_D \frac{\lambda}{V_{eff}} + \theta_{2\|_V} \tag{3.16}$$

$$\theta_{1\perp_V} = \pm\sqrt{\tau' \frac{2c}{D_{eff}} - f'^2_D \frac{\lambda^2}{{V_{eff}}^2} - 2f'_D \frac{\lambda}{V_{eff}}\theta_{2\|_V} + \theta^2_{2\perp_V}} \tag{3.17}$$

The Jacobian of the transform is given by

$$\mathrm{d}\theta_{1\|_V}\mathrm{d}\theta_{1\perp_V} = \frac{c\lambda}{D_{eff}V_{eff}\sqrt{\tau' \frac{2c}{D_{eff}} - f'^2_D \frac{\lambda^2}{{V_{eff}}^2} - 2f'_D \frac{\lambda}{V_{eff}}\theta_{2\|_V} + \theta^2_{2\perp_V}}}\mathrm{d}\tau'\mathrm{d}f'_D \tag{3.18}$$

After Applying the Jacobian factor, replacing $\theta_{1\|_V}$ and $\theta_{1\perp_V}$, removing $\delta()$ function, and replacing $h^*_{2p}(\theta_{2\|_V}, \theta_{2\perp_V})$ with $\delta(\theta_{2\|_V} - \theta_{o\|_V})\delta(\theta_{2\perp_V} - \theta_{o\perp_V})h^*_{2p}(\theta_{o\|_V}, \theta_{o\perp_V})$ since those are point source in assumption, Then the $\tilde{V}_1(\boldsymbol{b}, \tau, f_D)$ becomes

$$\tilde{V}_1(\boldsymbol{b}, \tau, f_D) = \{h_{1c}(\theta_f + \theta_{o\|_V}, U_1) + h_{1c}(\theta_f + \theta_{o\|_V}, -U_1\}\frac{C_0}{U_1}h^*_{2p}(\theta_{o\|_V}, \theta_{o\perp_V}) \tag{3.19}$$

where

$$U_1 \triangleq \sqrt{\tau \frac{2c}{D_{eff}} - f^2_D \frac{\lambda^2}{{V_{eff}}^2} - 2f_D \frac{\lambda}{V_{eff}}\theta_{o\|_V} + \theta^2_{o\perp_V}} \tag{3.20}$$

$$\theta_f \triangleq f_D \frac{\lambda}{V_{eff}} \tag{3.21}$$

$$C_0 \triangleq \frac{2c\lambda}{D_{eff}V_{eff}} \tag{3.22}$$

Equation 3.19 shows that every point of $\tilde{V}_1(\boldsymbol{b}, \tau, f_D)$ comes from the one pair of interferences which are symmetric to the velocity axis. U_1 represents the distance of those two interferences to the velocity axis, it's also proportional to the inverse of Jacobian factor. θ_f is the angular shift in $\|_V$ which determines those two interferences" position in $\|_V$.

Apply the same procedure to $\tilde{V}_2(\boldsymbol{b}, \tau, f_D)$ and use the same definition of τ' and f'_D, we get

$$\theta_{2\|_V} = -f'_D \frac{\lambda}{V_{eff}} + \theta_{1\|_V} \tag{3.23}$$

$$\theta_{2\perp_V} = \pm\sqrt{-\tau' \frac{c}{D_{eff}} - f'^2_D \frac{\lambda^2}{{V_{eff}}^2} + 2f'_D \frac{\lambda}{V_{eff}} \theta_{1\|_V} + \theta^2_{1\perp_V}} \tag{3.24}$$

And

$$\tilde{V}_2(\boldsymbol{b}, \tau, f_D) = \{h^*_{2c}(-\theta_f + \theta_{o\|_V}, U_2) + h^*_{2c}(-\theta_f + \theta_{o\|_V}, -U_2\} \frac{C_0}{U_2} h_{1p}(\theta_{o\|_V}, \theta_{o\perp_V}) \tag{3.25}$$

where

$$U_2 \triangleq \sqrt{-\tau \frac{2c}{D_{eff}} - f^2_D \frac{\lambda^2}{{V_{eff}}^2} + 2f_D \frac{\lambda}{V_{eff}} \theta_{o\|_V} + \theta^2_{o\perp_V}} \tag{3.26}$$

Hence, reversed sub-arc can be expressed in $\|_V$ and $\perp_V$ coordinates as below

$$\begin{aligned} \tilde{V}(\boldsymbol{b}, \tau, f_D) &= \{h_{1c}(\theta_f + \theta_{o\|_V}, U_1) + h_{1c}(\theta_f + \theta_{o\|_V}, -U_1)\} \frac{C_0}{U_1} h^*_{2p}(\theta_{o\|_V}, \theta_{o\perp_V}) \\ &+ \{h^*_{2c}(-\theta_f + \theta_{o\|_V}, U_2) + h^*_{2c}(-\theta_f + \theta_{o\|_V}, -U_2)\} \frac{C_0}{U_2} h_{1p}(\theta_{o\|_V}, \theta_{o\perp_V}) \end{aligned} \tag{3.27}$$

This is the most fundamental equation in this section, it shows that, based on the point offset model, every point of the Fourier transform of complex visibility comes from two pairs of interferences.

3.1.1 Position mapping

According to the mathematical derivation above, each (τ, f_D) in a reversed sub-arc maps to four possible points in the center brightness image. Both U_1 and U_2 must be real, which makes a closed region where two pairs of solutions can only co-exist inside that region, and anywhere outside that region have two solutions. Each pair is symmetric to the velocity line which is marked as the red straight

line in Figure 3.1. The yellow ellipse in Figure 3.1 demonstrates the four-solutions region, if the part of the image we want to recover is outside of that yellow ellipse region, then we only need to consider the two solutions. In our case, we only recover the core image and there is only a small overlapping between the core image and the yellow ellipse. As the offset sources go further away from the center part, there will be less and less overlapping. Thus we only consider the last two terms in Eq(3.27) for $\tilde{V}(f_D, \tau, \mathbf{b})$ and the first two terms in Eq(3.27) for $\tilde{V}(-f_D, -\tau, \mathbf{b})$.

In $\|_V$ and $\perp_V$ coordinate, Eq(3.27) becomes

$$\tilde{V}(\boldsymbol{b}, \tau, f_D) = \{h^*_{1c}(\boldsymbol{\theta}_\alpha) + h^*_{1c}(\boldsymbol{\theta}_\beta)\}\frac{C_0}{U_2}h_{2p}(\boldsymbol{\theta}_0) \tag{3.28}$$

where

$$\begin{aligned}
\boldsymbol{\theta}_\alpha &= (-\theta_f + \theta_{o\|_V}, U_2) && (3.29a)\\
\boldsymbol{\theta}_\beta &= (-\theta_f + \theta_{o\|_V}, -U_2) && (3.29b)\\
\boldsymbol{\theta}_0 &= (\theta_{ox}, \theta_{oy}) && (3.29c)
\end{aligned}$$

If it's in Dec-RA coordinate, a simple conversion is needed, then the positions are

$$\begin{aligned}
\boldsymbol{\theta}_\alpha &= ((Q_1V_x + Q_2V_y), (Q_1V_x - Q_2V_y)) && (3.30a)\\
\boldsymbol{\theta}_\beta &= ((Q_1V_x - Q_2V_y), (Q_1V_x + Q_2V_y)) && (3.30b)\\
\boldsymbol{\theta}_0 &= (\theta_{ox}, \theta_{oy}) && (3.30c)\\
Q_1 &\triangleq \frac{(f_{Do} - f_D)\lambda}{{V_{eff}}^2} && (3.30d)\\
Q_2 &\triangleq \sqrt{\frac{(\tau_o - \tau)2c}{D_{eff}{V_{eff}}^2} - Q_1^2} && (3.30e)\\
& && (3.30f)
\end{aligned}$$

3.1.2 Brightness intensity reconstruction

In the last section, position mapping from the Fourier transform of visibility spectrum to brightness Image has been discussed. In this section, more discussion will be made on the relationship between the amplitude phase of $C(f_D, \tau, \boldsymbol{b})$ and the brightness intensity $B(\boldsymbol{\theta})$.

In each baseline, two receivers receive (but they couldn't because no telescope has such a fine angular resolution to resolve the brightness image) the same angular spectrum $g^+(\boldsymbol{\theta})$, but different baseline phase $k\boldsymbol{b}\cdot\boldsymbol{\theta}$.

In receiver 1

$$\begin{cases} h_{1c}(\boldsymbol{\theta}_\alpha) = \varepsilon_\alpha e^{j\phi_\alpha} & \text{point } \alpha \text{ in center brightness image} \\ h_{1c}(\boldsymbol{\theta}_\beta) = \varepsilon_\beta e^{j\phi_\beta} & \text{point } \beta \text{ in center brightness image} \\ h_{1p}(\boldsymbol{\theta}_0) = \varepsilon_p e^{j\phi_p} & \text{offset point source} \end{cases}$$

In receiver 2

$$\begin{cases} h_{2c}(\boldsymbol{\theta}_\alpha) = \varepsilon_\alpha e^{j\phi_\alpha - j\phi_{b\alpha}} & \text{point } \alpha \text{ in center brightness image} \\ h_{2c}(\boldsymbol{\theta}_\beta) = \varepsilon_\beta e^{j\phi_\beta - j\phi_{b\beta}} & \text{point } \beta \text{ in center brightness image} \\ h_{2p}(\boldsymbol{\theta}_0) = \varepsilon_p e^{j\phi_p - j\phi_{bp}} & \text{offset point source} \end{cases}$$

The unknown amplitudes we wish to estimate are ε_α ε_β, the random phases which we wish to remove are ϕ_α ϕ_β ϕ_p. $\phi_{b\alpha}(\triangleq k\boldsymbol{b}\cdot\boldsymbol{\theta}_\alpha)$, $\phi_{b\beta}(\triangleq k\boldsymbol{b}\cdot\boldsymbol{\theta}_\beta)$ is baseline phase which are already known. ϕ_{bp} can be directly achieved from the phase on an apex of reversed sub-arc.

$$\tilde{V}(\boldsymbol{b}, \tau, f_D) = C_0\{\varepsilon_\alpha e^{j\phi_\alpha - j\phi_{b\alpha}} + \varepsilon_\beta e^{j\phi_\beta - j\phi_{b\beta}}\}^* \varepsilon_p e^{j\phi_p}/U_2 \quad (3.31)$$

$$\tilde{V}(\boldsymbol{b}, -\tau, -f_D) = C_0\{\varepsilon_\alpha e^{j\phi_\alpha} + \varepsilon_\beta e^{j\phi_\beta}\}(\varepsilon_p e^{j\phi_p - j\phi_{bp}})^*/U_2 \quad (3.32)$$

Where constant C_0 is irrelevant to f_D and τ. Normalizing ($C_0\varepsilon_p = 1$) and multiplying $\tilde{V}(\boldsymbol{b}, \tau, f_D)$ and $\tilde{V}(\boldsymbol{b}, -\tau, -f_D)$, yields

$$\begin{aligned} C(\boldsymbol{b}, \tau, f_D) &= \tilde{V}(\boldsymbol{b}, \tau, f_D)\tilde{V}(\boldsymbol{b}, -\tau, -f_D) \\ &= e^{j\phi_p}\{\varepsilon_\alpha e^{j\phi_\alpha - j\phi_{b\alpha}} + \varepsilon_\beta e^{j\phi_\beta - j\phi_{b\beta}}\}^* \\ &\quad \times\{\varepsilon_\alpha e^{j\phi_\alpha} + \varepsilon_\beta e^{j\phi_\beta}\}(\varepsilon_p e^{j\phi_p - j\phi_{bp}})^*/U_2^2 \\ &= e^{j\phi_{bp}}\{\varepsilon_\alpha^2 e^{j\phi_{b\alpha}} + \varepsilon_\beta^2 e^{j\phi_{b\beta}} + \varepsilon_\alpha\varepsilon_\beta \\ &\quad (e^{j\phi_{b\alpha}}e^{j\phi_\beta - j\phi_\alpha} + e^{j\phi_{b\beta}}e^{j\phi_\alpha - j\phi_\beta})\}/U_2^2 \end{aligned} \tag{3.33}$$

In order to remove random phase, more than one baseline is required. Define the other baseline phase as $\phi'_{b\alpha} \triangleq k\boldsymbol{b}' \cdot \boldsymbol{\theta}_\alpha$, $\phi'_{b\beta} \triangleq k\boldsymbol{b}' \cdot \boldsymbol{\theta}_\beta$ and $\phi'_{bp} \triangleq k\boldsymbol{b}' \cdot \boldsymbol{\theta}'_0$.

$$\begin{aligned} C(\boldsymbol{b}, \tau, f_D) &= {\varepsilon_p}^2 e^{j\phi_{bp}}(\varepsilon_\alpha e^{-j(\phi_\alpha - \phi_{b\alpha})} + \varepsilon_\beta e^{-j(\phi_\beta - \phi_{b\beta})}) \\ &\quad (\varepsilon_\alpha e^{j\phi_\alpha} + \varepsilon_\beta e^{j\phi_\beta})/U_2^2 \end{aligned} \tag{3.34a}$$

$$\begin{aligned} C(\boldsymbol{b}', \tau, f_D) &= {\varepsilon'_p}^2 e^{j\phi'_{bp}}(\varepsilon_\alpha e^{-j(\phi_\alpha - \phi'_{b\alpha})} + \varepsilon_\beta e^{-j(\phi_\beta - \phi'_{b\beta})}) \\ &\quad (\varepsilon_\alpha e^{j\phi_\alpha} + \varepsilon_\beta e^{j\phi_\beta})/U_2^2 \end{aligned} \tag{3.34b}$$

and define

$$G_\alpha \triangleq (\varepsilon_\alpha e^{j\phi_\alpha} + \varepsilon_\beta e^{j\phi_\beta})\varepsilon_\alpha e^{-j\phi_\alpha} = \alpha + j\gamma \tag{3.35a}$$

$$G_\beta \triangleq (\varepsilon_\alpha e^{j\phi_\alpha} + \varepsilon_\beta e^{j\phi_\beta})\varepsilon_\beta e^{-j\phi_\beta} = \beta - j\gamma \tag{3.35b}$$

G_α and G_β share the same imaginary part with opposite sign. By the definition of G_α and G_β, Brightness intensity at $\boldsymbol{\theta}_\alpha$ and $\boldsymbol{\theta}_\beta$ can be expressed as

$$B(\boldsymbol{\theta}_\alpha) = \varepsilon_\alpha^2 = \frac{\alpha^2 + \gamma^2}{\alpha + \beta} \tag{3.36a}$$

$$B(\boldsymbol{\theta}_\beta) = \varepsilon_\beta^2 = \frac{\beta^2 + \gamma^2}{\alpha + \beta} \tag{3.36b}$$

Multiple sub-arcs can be used at once by solving the normal equations below to get better estimate

$$\begin{pmatrix} \cos\phi_{b\alpha} & \cos\phi_{b\beta} & -\sin\phi_{b\alpha}+\sin\phi_{b\beta} \\ \sin\phi_{b\alpha} & \sin\phi_{b\beta} & \cos\phi_{b\alpha}-\cos\phi_{b\beta} \\ \cos\phi'_{b\alpha} & \cos\phi'_{b\beta} & -\sin\phi'_{b\alpha}+\sin\phi'_{b\beta} \\ \sin\phi'_{b\alpha} & \sin\phi'_{b\beta} & \cos\phi'_{b\alpha}-\cos\phi'_{b\beta} \\ \vdots & \vdots & \vdots \end{pmatrix} \begin{pmatrix} \alpha \\ \beta \\ \gamma \end{pmatrix} = \begin{pmatrix} \mathbb{R}(C(\boldsymbol{b},\tau,f_D)e^{-j\phi_{bp}}) \\ \mathbb{I}(C(\boldsymbol{b},\tau,f_D)e^{-j\phi_{bp}}) \\ \mathbb{R}(C(\boldsymbol{b}',\tau,f_D)e^{-j\phi'_{bp}}) \\ \mathbb{I}(C(\boldsymbol{b}',\tau,f_D)e^{-j\phi'_{bp}}) \\ \vdots \end{pmatrix} Q_2^2$$

Use equation above with multiple baselines, random phase (ϕ_α, ϕ_β) can be completely removed with secondary cross spectra provided by multiple baselines (three telescopes at least).

3.1.3 Simulation

Simulation has been used to test and confirm the scattered image reconstruction algorithm. We first create the interferometer visibility function using a Kolmogorov model with 3:1 axis ratio, and take the Fourier transform to get the input brightness image. Figure 3.2 shows the simulated input core image with an offset bright point marked. Then we use this input image to create the secondary spectrum. The reversed sub-arc associated with the offset bright point is simulated and plotted in Figure 3.3. Random phase in the scattering screen and baseline phase are included. Two baselines are simulated to remove the random phase. Figure 3.4 shows the reconstructed core image which is achieved from the reversed sub-arcs of two baselines according to the algorithm above. It is accurately recovered with a small gap along the velocity vector. The velocity vector in brightness domain maps from the upper-edge of reversed sub-arc, where the factor U_2 becomes zero, which makes the normal equation un-resolvable and causes the distortion. This simulation confirms that the algorithm is successful.

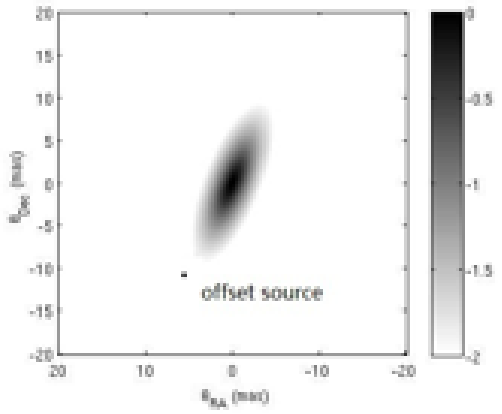

Figure 3.2: Input core image for simulation, y-axis is θ_{Dec}[-20mas 20mas] and x-axis is θ_{RA}[-20mas 20mas]

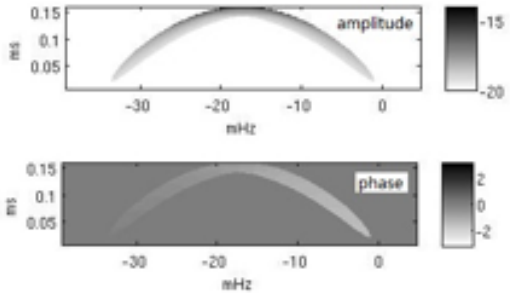

Figure 3.3: Reversed sub-arc from input core image of baseline 1, y-axis is delay[0ms 0.15ms], x-axis is Doppler frequency[-40mHz 5mHz], the upper panel is amplitude in $\log_{10}$, and the lower panel is phase in radian

3.1.4 Apply to pulsar B0834+06 observation data and discussion

We applied this algorithm to the same observation data set which is discussed in Chapter 2. We choose a reversed sub-arc with high S/N from the secondary cross spectra and plot this sub-arc's amplitude and phase in Figure 3.5 and Figure 3.6 with GBT-AO (left panel) and Westbork-AO (right panel) baselines respectively. This specific dataset includes all 4 sub-channels which provides higher resolution in secondary cross spectrum. The area between those two black parabolic arc is used to converted into the core brightness image.

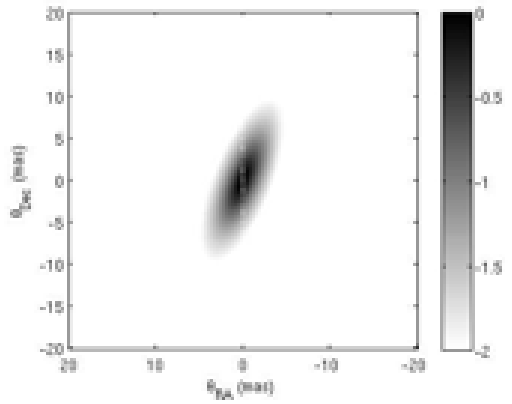

Figure 3.4: Reconstructed core image from simulated secondary cross spectrum, y-axis is θ_{Dec}[-20mas 20mas] and x-axis is θ_{RA}[-20mas 20mas], the gap along the velocity vector is because its Jacobian factor U_2 becomes zero at velocity axis which makes the normal equation un-resolvable and causes the distortion

There are a few parameters that we need to estimate.

1. Normalization factor: This is the most important parameter, which is the normalization ratio between two different baseline, due to the different gain of antenna in each baseline. Here we choose 1.65 which comes from the average of ratio of secondary auto spectra between two different baselines.

2. sub-arc's apex position: or the offset point source's position. According to the algorithm and simulation, each sub-arc has a really sharp parabolic upper edge with curvature bc.

$$bc = \frac{\lambda^2 D_{eff}}{2cV_{eff}{}^2} \tag{3.37}$$

and when we do strip integration along the forward arc's apex, the curvature is different

$$c = \frac{\lambda^2 D_{eff}}{2cV_{eff}{}^2 \cos^2 \alpha} \tag{3.38}$$

where α is the angle between the velocity and the main axis of the primary linear feature. Sub-arc's apex lies on the top of parabolic edge. In Figure 3.5, the sub-arc we chose doesn't have a sharp edge as seen in simulation, which makes it really hard to estimate the sub-arc's apex position, especially the

delay of it. Here we choose the top of the black sub-arc in Figure 3.5 as a possible position of this sub-arc.

3. Phase on apex: A small fluctuation on the baseline phase of the offset point would shift the value the entire brightness. We can calculate the phase if based on the offset point source's position. In order to avoid the estimate error propagation on apex position, we estimate it by averaging the phase around the apex position in secondary cross spectrum.

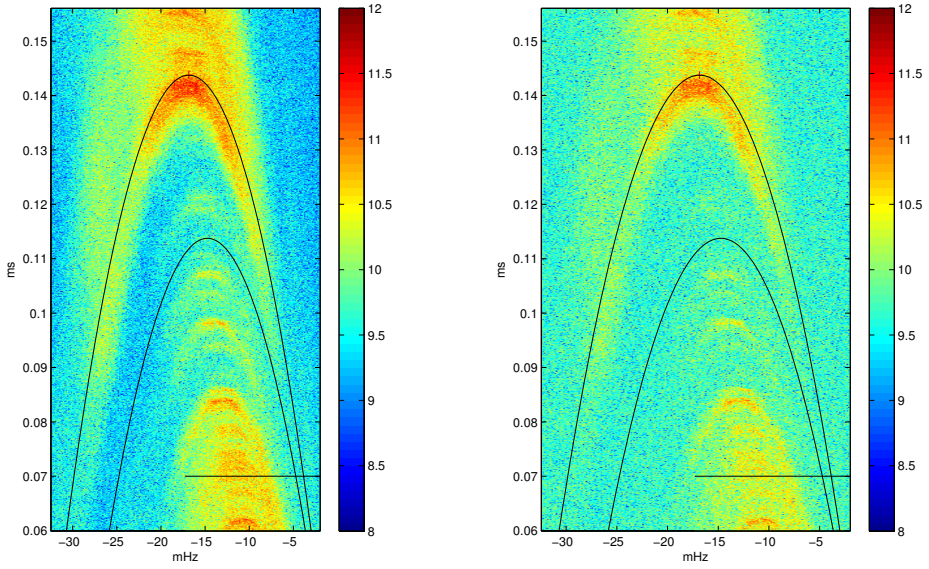

Figure 3.5: Amplitude of reversed sub-arc 1, GBT-AO baseline (left) and Westbork-AO baseline (right)

Figure 3.7 shows the reconstructed core image using one baseline (GBT-AO baseline). Figure 3.8 shows the reconstructed core image using multiple baselines (both GBT-AO baseline and Westbork-AO baseline). Both of them show a gap along the vertical axis which is coincidence with the velocity vector is due to the finite size of pixel along the upper-edge of the sub-arc. Each pair of points ($\boldsymbol{\theta}_\alpha$, $\boldsymbol{\theta}_\beta$) are symmetric to the velocity vector, and this technique is supposed to distinguish the brightness of those two points. However for multiple baseline case, it

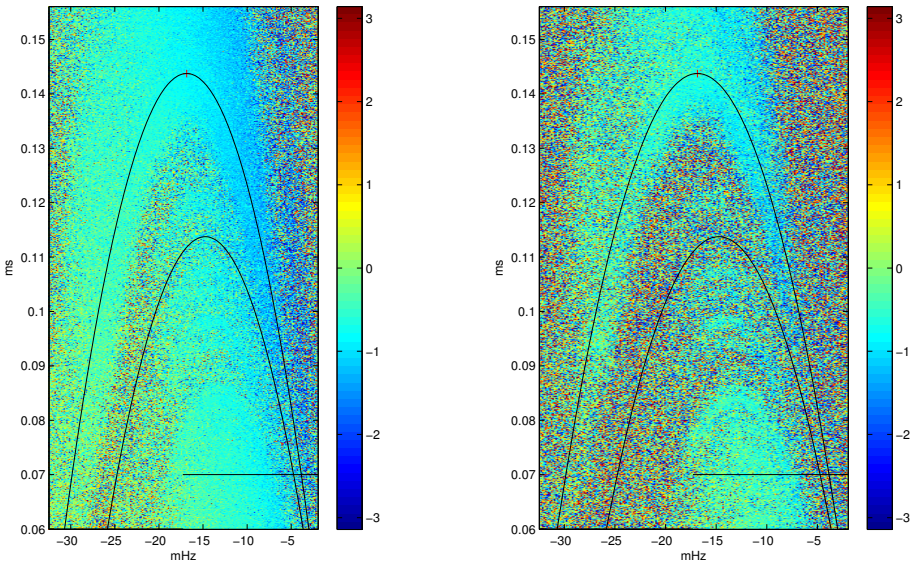

Figure 3.6: Phase of reversed sub-arc 1, GBT-AO baseline (left) and Westbork-AO baseline (right)

doesn't distinguish brightness around -2 mas along Dec axis. Both images show some brightness structure which is roughly parallel with the linear structure we found in previous chapter. Those bright area further from the origin doesn't mean the brightness in that area is high, it's due to the error introduced by low S/N in the tail region of reversed sub-arc.

We also observe that there is a null in the center of the reconstructed core image which disagrees with the hump at the center of Brightness estimated from 1-D linear model. We found similar results using data from other sub-arcs. After considering various assumptions in the reconstruction, we have concluded that the explanation is that the offset source might be slightly extended as we discuss in the next section.

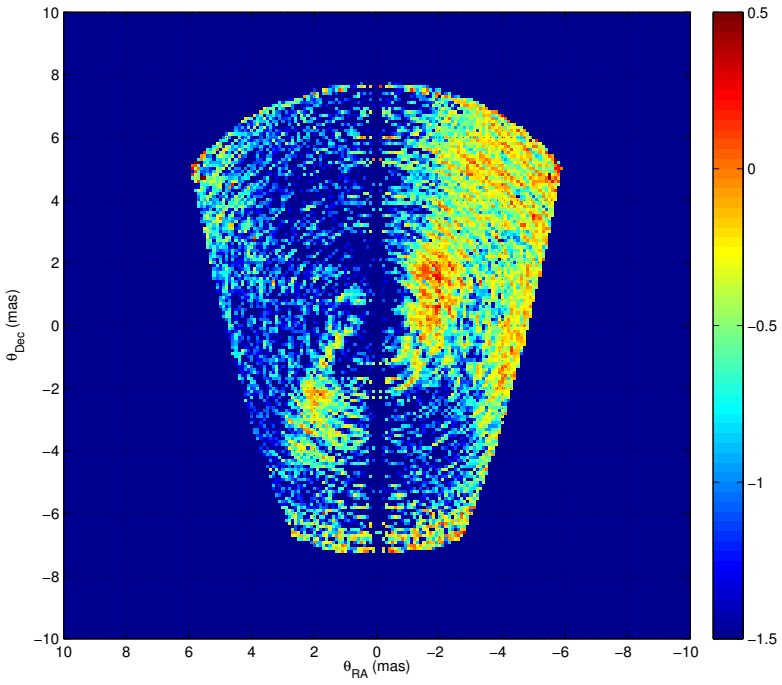

Figure 3.7: Reconstructed core image using one baseline (GBT-AO)

3.2 Reconstruct core image from reversed sub-arcs using ensemble-averaging model

Section 3.1 presents a method to reconstruct core image based on Equation 3.1 which means that the secondary cross spectrum is the instantaneous product of $\tilde{V}(f_D, \tau, \boldsymbol{b})$ and $\tilde{V}(-f_D, -\tau, \boldsymbol{b})$. Our observation data is recorded in the time span of 1 hour, it's reasonable that ensemble-averaging should be considered.

3.2.1 Theory

In this case, Equation 3.1 becomes

$$C(f_D, \tau, \boldsymbol{b}) = \langle \tilde{V}(f_D, \tau, \boldsymbol{b}) \tilde{V}(-f_D, -\tau, \boldsymbol{b}) \rangle \tag{3.39}$$

Use Eq 3.6, Secondary Cross Spectrum is

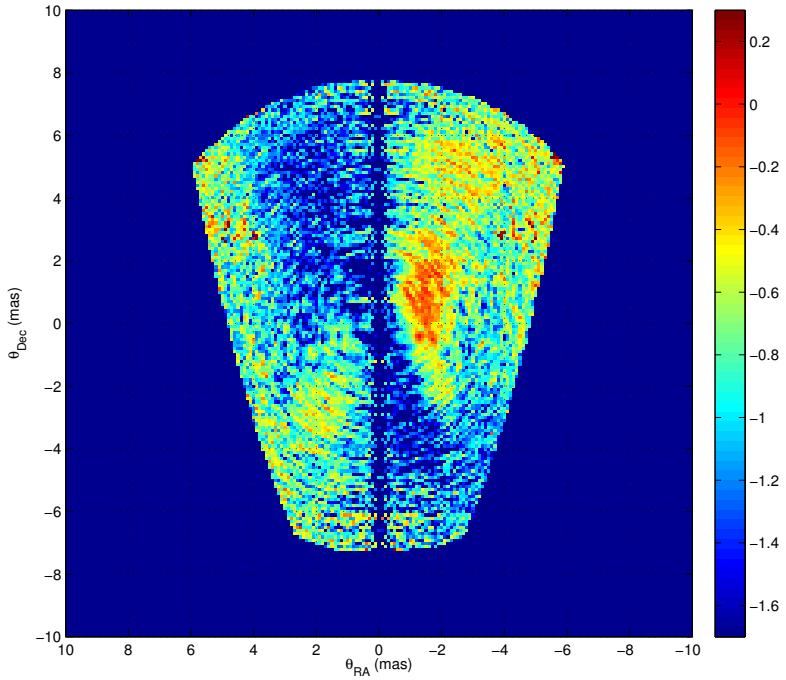

Figure 3.8: Reconstructed core image using two baselines (GBT-AO and Westbork-AO)

$$
\begin{aligned}
C(f_D, \tau, \boldsymbol{b}) \;=\; & \iiiint \langle g^{+}(\boldsymbol{\theta}_1) g^{+*}(\boldsymbol{\theta}_2) g^{+}(\boldsymbol{\theta}_3) g^{+*}(\boldsymbol{\theta}_4) \rangle \\
& \exp[-jk(\boldsymbol{b}_1 \cdot (\boldsymbol{\theta}_1 + \boldsymbol{\theta}_3) - \boldsymbol{b}_2 \cdot (\boldsymbol{\theta}_2 + \boldsymbol{\theta}_4))] \delta(\tau' - \tau) \delta(\tau'' + \tau) \\
& \delta(f'_D - f_D) \delta(f''_D + f_D) \mathrm{d}^2\boldsymbol{\theta}_1 \, \mathrm{d}^2\boldsymbol{\theta}_2 \mathrm{d}^2\boldsymbol{\theta}_3 \, \mathrm{d}^2\boldsymbol{\theta}_4 \qquad (3.40)
\end{aligned}
$$

Where

$$
\begin{aligned}
f'_D &= \frac{(\boldsymbol{\theta}_1 - \boldsymbol{\theta}_2) \cdot \boldsymbol{V}_{\mathit{eff}}}{\lambda} && (3.41) \\
f''_D &= \frac{(\boldsymbol{\theta}_3 - \boldsymbol{\theta}_4) \cdot \boldsymbol{V}_{\mathit{eff}}}{\lambda} && (3.42) \\
\tau' &= \frac{(\theta_1^2 - \theta_2^2) D_{\mathit{eff}}}{2c} && (3.43) \\
\tau'' &= \frac{(\theta_3^2 - \theta_4^2) D_{\mathit{eff}}}{2c} && (3.44)
\end{aligned}
$$

Assume $g^{+}(\boldsymbol{\theta}_1)$ $g^{+*}(\boldsymbol{\theta}_2)$ $g^{+}(\boldsymbol{\theta}_3)$ $g^{+*}(\boldsymbol{\theta}_4)$ are zero mean, gaussian random complex variables, with both real and imaginary part independent and of the same variances.

$$\begin{aligned}\langle g^{+}(\boldsymbol{\theta}_1)g^{+*}(\boldsymbol{\theta}_2)g^{+}(\boldsymbol{\theta}_3)g^{+*}(\boldsymbol{\theta}_4)\rangle &= \langle g^{+}(\boldsymbol{\theta}_1)g^{+*}(\boldsymbol{\theta}_2)\rangle\langle g^{+}(\boldsymbol{\theta}_3)g^{+*}(\boldsymbol{\theta}_4)\rangle + \\ \langle g^{+}(\boldsymbol{\theta}_1)g^{+}(\boldsymbol{\theta}_3)\rangle\langle g^{+*}(\boldsymbol{\theta}_2)g^{+*}(\boldsymbol{\theta}_4)\rangle &+ \langle g^{+}(\boldsymbol{\theta}_1)g^{+*}(\boldsymbol{\theta}_4)\rangle\langle g^{+*}(\boldsymbol{\theta}_2)g^{+}(\boldsymbol{\theta}_3)\rangle \quad (3.45)\end{aligned}$$

For any complex random variable $g = x + jy$, if x and y are independent with the same variances σ^2, then

$$\langle gg^{*}\rangle = \langle x^2\rangle + \langle y^2\rangle = 2\sigma^2 \quad (3.46)$$

$$\langle gg\rangle = \langle x^2\rangle - \langle y^2\rangle + 2j\langle x\rangle\langle y\rangle = 0 \quad (3.47)$$

If $g^{+}(\boldsymbol{\theta})$ is complex stationary random process (gaussian white noise)

$$\langle g^{+}(\boldsymbol{\theta}_1)g^{+*}(\boldsymbol{\theta}_2)\rangle = \langle g^{+}(\boldsymbol{\theta}_1)g^{+*}(\boldsymbol{\theta}_1)\rangle\delta^2(\boldsymbol{\theta}_1 - \boldsymbol{\theta}_2) = B(\boldsymbol{\theta}_1)\delta^2(\boldsymbol{\theta}_1 - \boldsymbol{\theta}_2) \quad (3.48)$$

Then Equation 3.45 becomes

$$\begin{aligned}\langle g^{+}(\boldsymbol{\theta}_1)g^{+*}(\boldsymbol{\theta}_2)g^{+}(\boldsymbol{\theta}_3)g^{+*}(\boldsymbol{\theta}_4)\rangle &= B(\boldsymbol{\theta}_1)B(\boldsymbol{\theta}_3)\delta^2(\boldsymbol{\theta}_1 - \boldsymbol{\theta}_2)\delta^2(\boldsymbol{\theta}_3 - \boldsymbol{\theta}_4) \\ &+B(\boldsymbol{\theta}_1)B(\boldsymbol{\theta}_3)\delta^2(\boldsymbol{\theta}_1 - \boldsymbol{\theta}_4)\delta^2(\boldsymbol{\theta}_3 - \boldsymbol{\theta}_2) \quad (3.49)\end{aligned}$$

Secondary cross spectrum can be shown as

$$\begin{aligned}C(f_D, \tau, \boldsymbol{b}) &= \iint B(\boldsymbol{\theta}_1)B(\boldsymbol{\theta}_3)\exp[-jk\boldsymbol{b}\cdot(\boldsymbol{\theta}_1 + \boldsymbol{\theta}_3)]\mathrm{d}^2\boldsymbol{\theta}_1\,\mathrm{d}^2\boldsymbol{\theta}_3\delta^2(\tau)\delta^2(f_D) \\ &+ \iiiint B(\boldsymbol{\theta}_1)B(\boldsymbol{\theta}_3)\exp[-jk(\boldsymbol{b}_1\cdot(\boldsymbol{\theta}_1 + \boldsymbol{\theta}_3) - \boldsymbol{b}_2\cdot(\boldsymbol{\theta}_2 + \boldsymbol{\theta}_4))]\delta^2(\boldsymbol{\theta}_1 - \boldsymbol{\theta}_4) \\ &\delta^2(\boldsymbol{\theta}_3 - \boldsymbol{\theta}_2)\delta(\tau' - \tau)\delta(\tau'' + \tau)\delta(f'_D - f_D)\delta(f''_D + f_D)\mathrm{d}^2\boldsymbol{\theta}_1\,\mathrm{d}^2\boldsymbol{\theta}_2\mathrm{d}^2\boldsymbol{\theta}_3\,\mathrm{d}^2\boldsymbol{\theta}_4\end{aligned} \quad (3.50)$$

$\iint B(\boldsymbol{\theta}_1)B(\boldsymbol{\theta}_3)\exp[-jk\boldsymbol{b}\cdot(\boldsymbol{\theta}_1 + \boldsymbol{\theta}_3)]\mathrm{d}^2\boldsymbol{\theta}_1\,\mathrm{d}^2\boldsymbol{\theta}_3$ is a constant S_0. When $\boldsymbol{\theta}_1 = \boldsymbol{\theta}_4$, $\boldsymbol{\theta}_2 = \boldsymbol{\theta}_3$ makes $f'_D = -f''_D$, $\tau' = -\tau''$, and define $\boldsymbol{b} = \boldsymbol{b}_1 - \boldsymbol{b}_2$.

$$\begin{aligned}C(f_D, \tau) &= S_0\delta^2(\tau)\delta^2(f_D) + \iint B(\boldsymbol{\theta}_1)B(\boldsymbol{\theta}_2) \\ &\exp[-jk\boldsymbol{b}\cdot(\boldsymbol{\theta}_1 + \boldsymbol{\theta}_2)]\delta^2(\tau' - \tau)\delta^2(f'_D - f_D)\mathrm{d}^2\boldsymbol{\theta}_1\mathrm{d}^2\boldsymbol{\theta}_2 \quad (3.51)\end{aligned}$$

The first term is a DC term which is only at origin. If we ignore this term, the secondary spectrum can be expressed as a form similar to the fundamental Equation 8 of [13], except two differences. Firstly, Equation 3.51 has phase term while Equation 8 of [13] doesn't. This is not an inconsistency since Equation 3.51 is secondary cross spectrum while the other is secondary auto spectrum. Secondly, Equation 3.51 has $\delta^2(\tau' - \tau)\delta^2(f'_D - f_D)$ while the other has $\delta(\tau' - \tau)\delta(f'_D - f_D)$. This is an inconsistency which goes back to the formulation of the visibility from the scattered image in Equation 3.6, where a δ function is introduced to constrain the angles so that they give a specific Doppler frequency and delay. That δ function becomes δ^2 after we form Equation 3.40 using Equation 3.6 and two same δ functions become δ^2 in Equation 3.51. δ^2 leads to infinity if we integrate δ^2 out in Equation 3.58. While we have not yet resolved this inconsistency mathematically, we replace δ^2 by δ which is then consistent with Equation 8 of [13] when the baseline goes to zero.

$$C(f_D, \tau, \boldsymbol{b}) = \iint B(\boldsymbol{\theta}_1)B(\boldsymbol{\theta}_2)\exp[-jk\boldsymbol{b}\cdot(\boldsymbol{\theta}_1 + \boldsymbol{\theta}_2)]\delta(\tau' - \tau)\delta(f'_D - f_D)\mathrm{d}^2\boldsymbol{\theta}_1\mathrm{d}^2\boldsymbol{\theta}_2 \tag{3.52}$$

It's actually a four-dimensional integral.

$$\begin{aligned} C(f_D, \tau, \boldsymbol{b}) &= \iiiint B(\theta_{1\parallel_V}, \theta_{1\perp_V})B(\theta_{2\parallel_V}, \theta_{2\perp_V})\exp[-jk\boldsymbol{b}\cdot(\boldsymbol{\theta}_1 + \boldsymbol{\theta}_2)] \\ &\quad \delta(\tau' - \tau)\delta(f'_D - f_D)\mathrm{d}\theta_{1\parallel_V}\mathrm{d}\theta_{1\perp_V}\mathrm{d}\theta_{2\parallel_V}\mathrm{d}\theta_{2\perp_V} \end{aligned} \tag{3.53}$$

Where

$$\begin{aligned} \tau' &= ((\theta^2_{1\parallel_V} + \theta^2_{1\perp_V}) - (\theta^2_{2\parallel_V} + \theta^2_{2\perp_V}))\frac{D_{\mathit{eff}}}{2c} \\ f'_D &= (\theta_{1\parallel_V} - \theta_{2\parallel_V})\frac{V_{\mathit{eff}}}{\lambda} \end{aligned}$$

$\parallel_V$ is parallel to effective velocity, and $\boldsymbol{V}_{\mathit{eff}} = (V_{\mathit{eff}}, 0)$. By solving $\theta_{2\parallel_V}$ and $\theta_{2\perp_V}$, we get

$$\theta_{2\parallel_V} = -f'_D\frac{\lambda}{V_{eff}} + \theta_{1\parallel_V} \tag{3.55}$$

$$\theta_{2\perp_V} = \pm\sqrt{-\tau'\frac{2c}{D_{eff}} - f'^2_D\frac{\lambda^2}{{V_{eff}}^2} + 2f'_D\frac{\lambda}{V_{eff}}\theta_{1\parallel_V} + \theta^2_{1\perp_V}} \tag{3.56}$$

And Jacobian transform is

$$\mathrm{d}\theta_{2\parallel_V}\mathrm{d}\theta_{2\perp_V} = \frac{c\lambda}{D_{eff}V_{eff}\sqrt{-\tau'\frac{2c}{D_{eff}} - f'^2_D\frac{\lambda^2}{{V_{eff}}^2} + 2f'_D\frac{\lambda}{V_{eff}}\theta_{1\parallel_V} + \theta^2_{1\perp_V}}}\mathrm{d}\tau'\mathrm{d}f'_D \tag{3.57}$$

After integrating out the $\delta()$ functions it becomes a double integral

$$\begin{aligned} C(f_D,\tau,\boldsymbol{b}) = \iint (B(-f_D\frac{\lambda}{V_{eff}} + \theta_{1\parallel_V}, U_2)\exp[-jk(\boldsymbol{b}_{\parallel_V}(-f_D\frac{\lambda}{V_{eff}} + \theta_{1\parallel_V}) + \\ \boldsymbol{b}_{\perp_V}U_2)] + B(-f_D\frac{\lambda}{V_{eff}} + \theta_{1\parallel_V}, -U_2)\exp[-jk(\boldsymbol{b}_{\parallel_V}(-f_D\frac{\lambda}{V_{eff}} + \theta_{1\parallel_V}) - \boldsymbol{b}_{\perp_V}U_2)]) \\ B(\theta_{1\parallel_V},\theta_{1\perp_V})\exp[-jk(\boldsymbol{b}_{\parallel_V}\theta_{1\parallel_V} + \boldsymbol{b}_{\perp_V}\theta_{1\perp_V})]\frac{2c\lambda}{D_{eff}V_{eff}U_2}\mathrm{d}\theta_{1\parallel_V}\mathrm{d}\theta_{1\perp_V} \end{aligned} \tag{3.58}$$

Similar to the previous section, offset source is a point source

$$\begin{aligned} B(\theta_{1\parallel_V},\theta_{1\perp_V})\exp[-jk(\boldsymbol{b}_{\parallel_V}\theta_{1\parallel_V} + \boldsymbol{b}_{\perp_V}\theta_{1\perp_V})] = \\ B(\theta_{0\parallel_V},\theta_{0\perp_V})\exp[-jk(\boldsymbol{b}_{\parallel_V}\theta_{0\parallel_V} + \boldsymbol{b}_{\perp_V}\theta_{0\perp_V})]\delta(\theta_{1\parallel_V} - \theta_{0\parallel_V})\delta(\theta_{1\perp_V} - \theta_{0\perp_V}) \end{aligned} \tag{3.59}$$

After Integrating Equation 3.58

$$\begin{aligned} C(f_D,\tau,\boldsymbol{b}) &= \{B(-\theta_f + \theta_{0\parallel_V}, +U_2)e^{-j\phi_{b\alpha}} + B(-\theta_f + \theta_{0\parallel_V}, -U_2)e^{-j\phi_{b\beta}}\} \\ &\quad B(\theta_{0\parallel_V},\theta_{0\perp_V})e^{-j\phi_{bp}}\frac{C_0}{U_2} \end{aligned} \tag{3.60}$$

where

$$\phi_{b\alpha} = k(-\boldsymbol{b}_{\parallel_V}\theta_f + \boldsymbol{b}_{\perp_V}U_2) \quad (3.61)$$

$$\phi_{b\beta} = k(-\boldsymbol{b}_{\parallel_V}\theta_f - \boldsymbol{b}_{\perp_V}U_2) \quad (3.62)$$

$$\phi_{bp} = k(\boldsymbol{b}_{\parallel_V}\theta_{0\parallel_V} + \boldsymbol{b}_{\perp_V}\theta_{0\perp_V}) \quad (3.63)$$

Compare this equation with Equation 3.27 in the previous section. They are similar, but Equation 3.27 is the Fourier transform of visibility function, and Equation 3.60 is the secondary cross spectrum. After ensemble averaging, there is only one pair of interferences, and there is no random phase noise either. In this case, only one baseline is enough to resolve $B(\theta_f, +U_1)$ and $B(\theta_f, -U_1)$, and there is no approximation of losing another pair of interferences. The solution for this complex function is

$$\begin{pmatrix} \cos\phi_{b\alpha} & \cos\phi_{b\beta} \\ \sin\phi_{b\alpha} & \sin\phi_{b\beta} \end{pmatrix} \begin{pmatrix} B_1 \\ B_2 \end{pmatrix} = \begin{pmatrix} \mathbb{R}(C(\boldsymbol{b},\tau,f_D)e^{-j\phi_{bp}}) \\ \mathbb{I}(C(\boldsymbol{b},\tau,f_D)e^{-j\phi_{bp}}) \end{pmatrix} U_2$$

3.2.2 Apply to observation data and discussion

We again apply this algorithm above to the same observed data set. The same sensitive parameters are used in this realization as the instantaneous model. Figure 3.9 shows the reconstructed core image from the same sub-arc using ensemble averaging model with GBT-AO baseline and Figure 3.10 shows the reconstructed core image with Westbork-AO baseline

Reconstructed core image using ensemble averaging model is not similar with Figure 3.8 which is based on instantaneous model. Although the vertical gap is still in the brightness image using ensemble averaging, the null in the center disappears. There are still a few small holes inside the core image but it's not as bad as the instantaneous case.

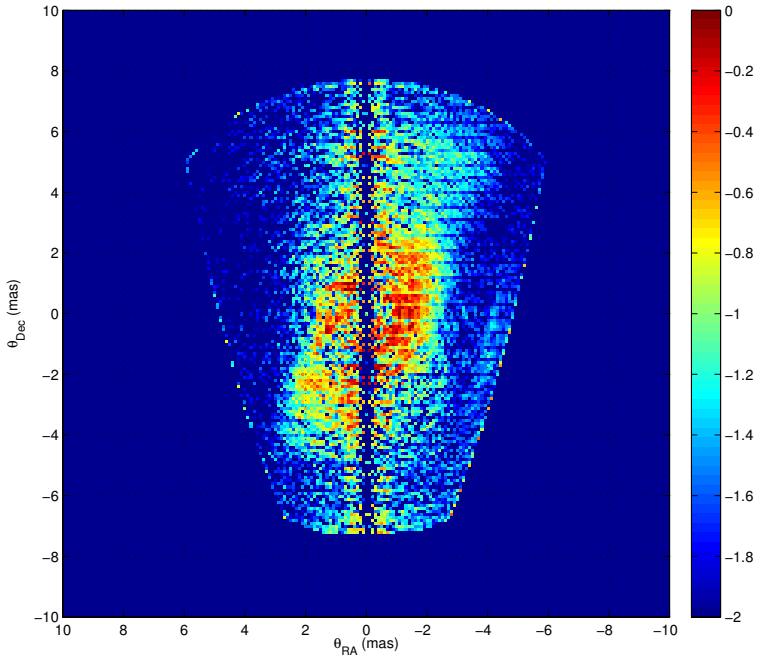

Figure 3.9: Reconstructed core image from sub-arc 1, ensemble averaging model, GBT-AO baseline

Although averaging seems have better brightness core image result, It's still hard to tell which model is more close to the reality, just based on the reconstructed core image from those two models. There is some parameter which might not be set up correctly, such as the antenna gain ratio between different baseline, and core image reconstruction using ensemble averaging doesn't need this parameter since it only needs one baseline.

We rotate the core image to its main axis and sum both along parallel direction and perpendicular direction, to get its 1-D brightness in both directions, and they are shown in Figure 3.11, in log scale($log10$). The upper panel shows the 1-d brightness in parallel direction $B(\theta_{\parallel})$ and the lower panel shows the 1-d brightness in perpendicular direction $B(\theta_{\perp})$. Here $\parallel$ and $\perp$ are relative to the image axis, not velocity.

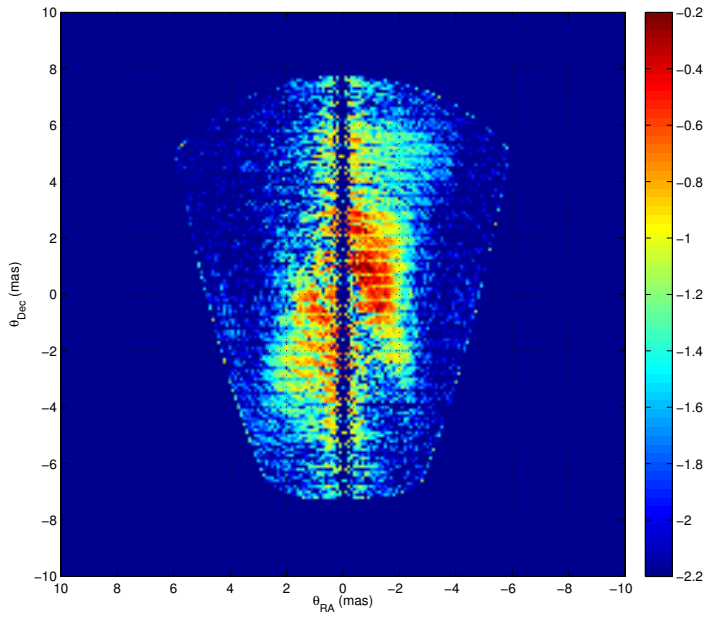

Figure 3.10: Reconstructed core image from sub-arc 1, ensemble averaging model, Westbork-AO baseline

In order to compare with our previous result, we plot both the directly-sampled 1-d brightness from secondary spectrum which is shown in Chapter2 and this new 1-d $B(\theta_{\parallel})$ in Figure 3.12, in blue and red respectively. They match very precisely, especially in the center region between -5 has to 3 mas. It's a strong proof that that this reconstructed core brightness image shown in Figure 3.9 and Figure 3.10 are reasonable estimation.

This is our first time to obtain the perpendicular information of the brightness image. There is a small dent at origin next to two little bumps in $B(\theta_{\perp})$ plot at roughly 1 mas and -1 mas. We believe that dent is due to the null shown in the 2-D reconstructed core image. It affects $B(\theta_{\perp})$ much more than $B(\theta_{\parallel})$ because the null is more vertical to the perpendicular direction and it only distorts the center part of $B(\theta_{\parallel})$, while it distorts almost evenly everywhere in $B(\theta_{\parallel})$. $B(\theta_{\parallel})$ is more homogeneous, and the distribution is very exponential since it is in log scale and it shows linear distribution in the plot.

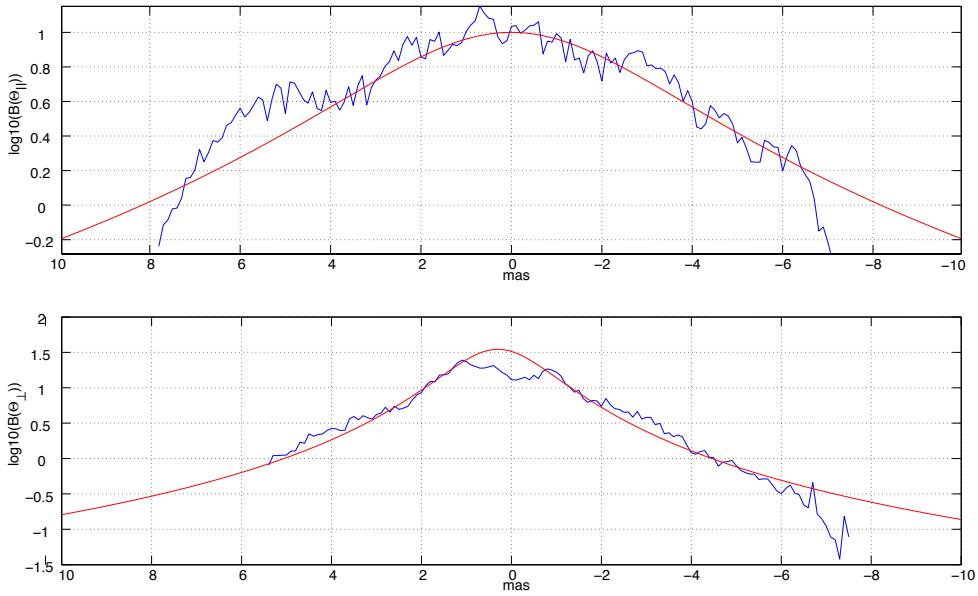

Figure 3.11: 1-d brightness along the parallel direction (upper) and perpendicular direction (lower)

We fit a 1-D kolmogorov model to both $B(\theta_{\|})$ and $B(\theta_{\perp})$ using equation below,

$$B(\theta) = \frac{C}{(1 + (\frac{\theta - \theta_0}{\theta_p})^2)^{\frac{8}{6}}} \tag{3.64}$$

This equation is based on 2-D kolmogorov model integrated over one axis, that's why the index is 8/6 instead of 11/6. When fitting $B(\theta_{\|})$, we didn't include the bump at 6 mas, while When fitting $B(\theta_{\perp})$, we didn't include the dent in the center. Both constant C, offset θ_0 and characteristic width θ_p are fitted. The fitting result is over plotted in red.

For $B(\theta_{\|})$, there is no offset and $\theta_p \sim 3.85$ mas. For $B(\theta_{\perp})$, offset $\theta_0 \sim 0.3$ mas and $\theta_p \sim 1.3$ mas, which is much bigger than the intrinsic perpendicular RMS width we estimated in Chapter2 (less than 0.3 mas).
The estimated axial ratio is ~ 3

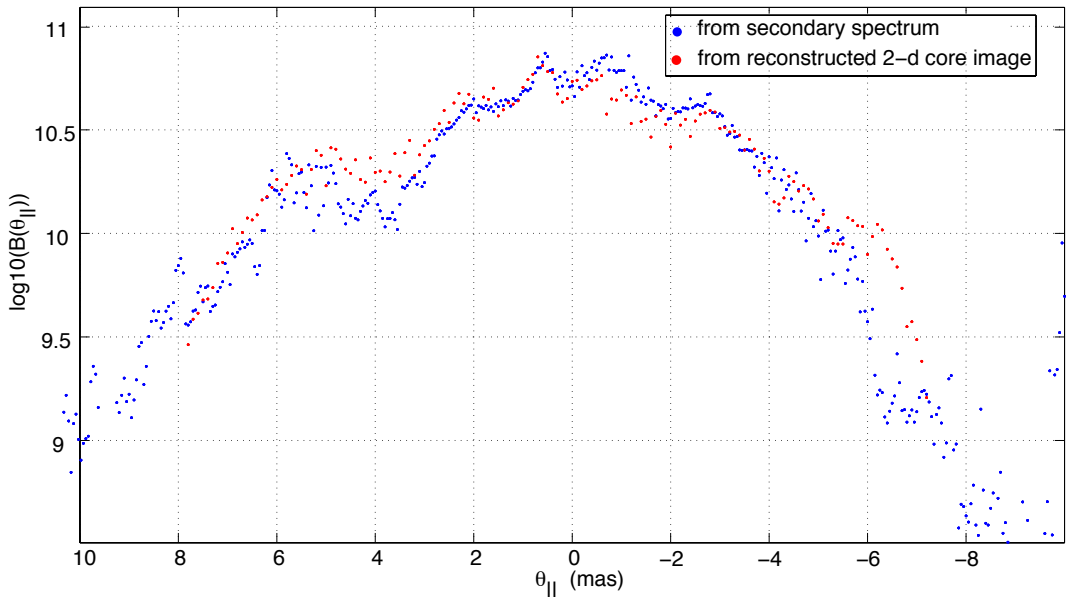

Figure 3.12: 1-D brightness along the parallel direction, the blue dots are estimated from sampling along the forward arcs in secondary spectrum, the red dots are estimated from integrating the reconstructed 2-D core image obtained using ensemble-averaging model

The rotated core image is also plotted in Figure 3.13 and we plot the half-power contour on it using 2-D kolmogorov model. The reason we chose 2-D kolmogorov model is that it's widely used to model the homogeneous scattering in the ISM.

3.2.3 Relationship between Instantaneous model and ensemble averaging model

Sections 3.1 and 3.2 present different theoretical relations for the secondary cross spectrum $C(f_D, \tau, \boldsymbol{b})$ in Equations 3.33 and 3.60, respectively. These lead to reconstruction algorithms that differ in detail. Here we compare them and conclude that the ensemble average method is more appropriate.

Our analysis in paper [2] discusses $\tilde{V}(f_D, \tau, \boldsymbol{b})$ as a summation over products of pairs of waves j & k, each one having its 'screen phase', which contribute to

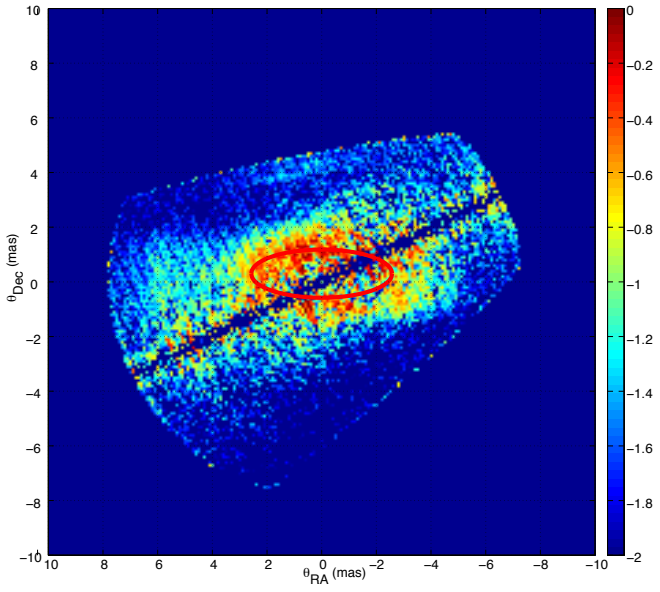

Figure 3.13: The rotated core image with half-power contour (red)

$\tilde{V}(f_D, \tau, \boldsymbol{b})$ via their difference $\phi_j - \phi_k$. The Secondary cross spectrum $C(f_D, \tau, \boldsymbol{b})$ should then involve products of 4 waves summed over pairs j,k and l,m. If you take the ensemble average of the 4-way product (and assume independent complex gaussian random fields) the delta functions enforce the $\theta_j = \theta_l$ and $\theta_k = \theta_m$ condition, so there are no contributions to $C(f_D, \tau, \boldsymbol{b})$ from the cross interference between wave pairs j,k or between l,m. In other words the secondary cross spectrum $C(f_D, \tau, \boldsymbol{b})$ comes down to a sum of the products of the Brightness from θ_j and the Brightness from θ_k. There are no contributions from the cross interference of fields from θ_j and θ_k. This justifies omitting the 3rd and 4th terms in Equation 3.33 and makes the instantaneous model the same as the ensemble average expression, except their Jacobian terms. In our observation data, the dynamic spectrum is recorded in the time span of 1 hour, it makes more sense to consider ensemble-average in our case.

Two models' Jacobian terms are different. For instantaneous model, we work with density function for the electric field components (ϵ), and $C(f_D, \tau, \boldsymbol{b}) = \tilde{V}(f_D, \tau, \boldsymbol{b})\tilde{V}(-f_D, -\tau, \boldsymbol{b})$. Both $V(f_D, \tau, \boldsymbol{b})$ and $V(-f_D, -\tau, \boldsymbol{b})$ have a Jacobian term U_2, which makes the total Jacobian U_2^2. In contrast, for ensemble-averaging

model, $C(f_D, \tau, \boldsymbol{b})$ is expressed in terms of the scattered brightness density function, Jacobian term U_2 is only used once. Instantaneous model's Jacobian term is square of ensemble-averaging model's, and Jacobian term tends to lower the brightness estimation when it's closer to the velocity axis, that's why there is a big hole in the center of the reconstructed core image using instantaneous model. This inconsistency in the Jacobians comes from the same reason as the inconsistency in δ that we address in section 3.2.1. Both of those inconsistency goes back to the formulation of the visibility from the scattered image in Equation 3.6. This is a more fundamental problem, Equation 3.6 is introduced without explicit justification and all the difficulties go back to that point. We still haven't resolved this inconsistency mathematically, and this is definitely the most important part of the further work.

3.3 The size of the offset scattering point

It's probably true that the size of the offset bright source is not small enough to be treated as point source and we need to estimate its size and revise the image reconstruction algorithm to take this size effect into account. It's easy to tell that this sub-arc doesn't have as sharp upper-edge as the simulated sub-arc in Figure 3.3, which is a sign that it's not point source. Some simulation work has been done to analyze this size effect by using simulation.

We first create an input brightness image with the same core image as the previous simulation, and the extended offset source with one tenth of the core image in size. Then we use this input image to create the secondary spectrum and reconstruct the core image from the secondary spectrum using the same algorithm. Figure 3.14 shows the reconstructed core image. We observe that there is a null in the center which splits the core image into two parts, just like the one being observed in the last section. We change the size of the offset source and do the same procedure, and the null becomes wider as the size of the offset source increases.

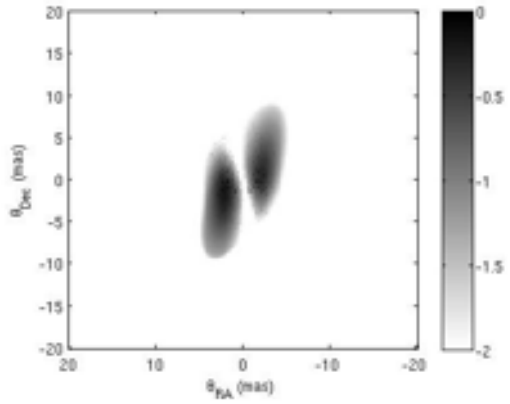

Figure 3.14: Reconstructed core image from extended offset source

For better comparison, we plot the smoothed reconstructed core image using ensemble averaging in Figure 3.15. Both of them show some null which looks very similar as the way that the simulated core image splits.

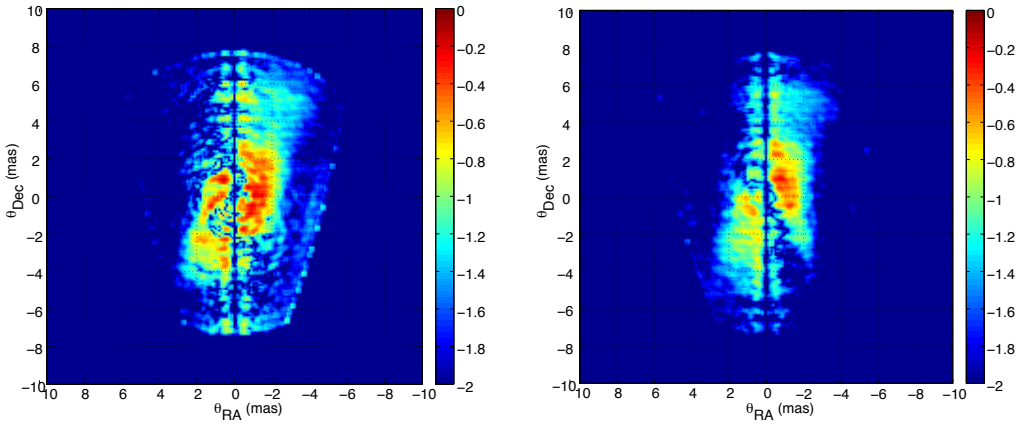

Figure 3.15: *Left:*Smoothed reconstructed core image from sub-arc 1, ensemble averaging model, GBT-AO baseline. *Right:* Same analysis applied to the Westerbork-AO baseline.

3.4 Estimation of perpendicular width of core image

In the previous section, we used reversed sub-arc to reconstruct the core image and estimated the 1-d brightness distribution in both parallel and perpendicular direction. The reversed sub-arc is due to the cross-interference between the offset bright source and the core image, if we assume the offset source is a point source we can reconstruct the core image in a backward way, which means from secondary spectrum domain to the angular domain, but the offset source isn't a perfect point and its size splits the core image and distorts the 1-d brightness distribution along perpendicular direction.

Can we make use of the center part of the secondary spectrum to estimate the 2-D brightness core image? The center part is due to the self-interference of the core image and there is no way to reconstruct core image in the backward way like we did to the reversed sub-arc, since each point in secondary spectrum in that region comes from multiple possible self-interference paris. But it is possible for us to generate secondary spectrum using a given 2D brightness image in a forward way.

In this section, we use forward method to generate the center part of secondary spectrum, compare it with the observation, and fit the width of the core image, to estimate the axial ratio.

3.4.1 Theory

This theory is based on ensemble averaging model. The idea is similar to the 2D core image reconstruction, but instead of solving complex Equation 3.60 and mapping brightness and position back from secondary spectrum, we generate the secondary spectrum layer by layer in a forward way, each layer is due to the 'cross-interferences' of one point $(\theta_{0\parallel}, \theta_{0\perp})$ in 2D brightness with the rest of it.

We convert Equation 3.60 to a summation form.

$$C(f_D,\tau,\boldsymbol{b}) = \sum_{\theta_{0\parallel},\theta_{0\perp}} \{B(\theta_f,+U_1)e^{-j\phi_{b\alpha}} + B(\theta_f,-U_1)e^{-j\phi_{b\beta}}\} B(\theta_{0\parallel},\theta_{0\perp})e^{-j\phi_{bp}}\frac{C_0}{U_1} \quad (3.65)$$

In each secondary spectrum layer, each pixel (f_D,τ) can be mapped to one pair of interference positions $(\theta_f,+U_1)$ and $(\theta_f,-U_1)$ in angular domain, given $(\theta_{0\parallel},\theta_{0\perp})$, and use Equation 3.60 to get one secondary spectrum layer, given the known 2-D brightness distribution. Summarize all the layers with different $(\theta_{0\parallel},\theta_{0\perp})$, we can get the entire secondary spectrum.

3.4.2 Estimate perpendicular width using forward fitting

We first generate the input 2-D brightness distribution model as below

$$B(\theta_\parallel,\theta_\perp) = B(\theta_\parallel)\frac{1}{(1+(\frac{\theta_\perp}{\theta_p})^2)^{11/6}} \quad (3.66)$$

or

$$B(\theta_\parallel,\theta_\perp) = B(\theta_\parallel)e^{-(\frac{\theta_\perp}{\theta_p})^2} \quad (3.67)$$

Where $B(\theta_\parallel)$ is the directly-sampled brightness distribution that we estimated in Chapter 2. The other term could be approximated 1-D kolmogorov distribution in Equation 3.66 , or gaussian distribution as in Equation 3.67. We assume brightness distribution in parallel direction and perpendicular direction are independent with each other, since two dimensional gaussian distribution can be separated into two 1-d gaussian distribution, we only use model described in Equation 3.67 in this section. We set up a threshold to eliminate layers with small $B(\theta_{0\parallel},\theta_{0\perp})$, to decrease the computation. Non-linear least mean squared fitting is used to fit θ_p. Since this is based on the self-interference between the core image, the fitting requires a lot of computation, but we only deal with the center part of the secondary spectrum so it's still acceptable.

The same observation data set of B0834+06 is used here. We used three data set which have high SNR: two secondary auto spectrum observed at GBT and AO and secondary cross spectrum observed in GBT-AO baseline. Only a small region close to the origin is used for fitting since we only consider the self-interference of the core image. We chose the region between 0 to 0.1 ms in delay and -10 to 10 mHz in Doppler. We fit θ_p by minimizing the sum of squared of normalized residuals between the data and the model. The normalization factor we used is the modeled brightness so those residuals with higher SNR has bigger weights.

The fitting results for two secondary auto spectrum and secondary cross spectrum are very similar. They are all very close to 1.25 mas. Although we didn't use the the kolmogorov model here so it's easy to compare with the perpendicular width we estimated in the previous section, we can still convert both θ_p to their half-power half-width by using $\theta_h = 0.8326\theta_p$ for gaussian model and $0.8257\theta_p$ for kolmogorov model, we get half-power half-width $\theta_h = 1.04\ mas$ for forward fitting which matches the conclusion about the half-power half-width ($\sim 1.07\ mas$) of the reconstructed core image using kolmogorov model from reversed sub-arc in the last section.

Figure 3.16 presents the modeled 2D brightness image with $\theta_p = 1.25\ mas$. The color dynamic range is set to be the same as the reconstructed core image from reversed sub-arc in Figure 3.9 for easy comparison. Figure 3.17 shows the amplitude of modeled (left) and observed (right) secondary cross spectrum.

3.4.3 Summary

In this section, we fit the perpendicular width of the brightness image by using the center part of the secondary spectrum, and get an approximated half-power half-width ($\sim 1\ mas$) which matches the result in the previous section. It provides another strong proof that the reconstructed 2-D core image is believable. ($\sim 1\ mas$) half-power half-width is still very narrow comparing to the brightness distribution along the parallel direction.

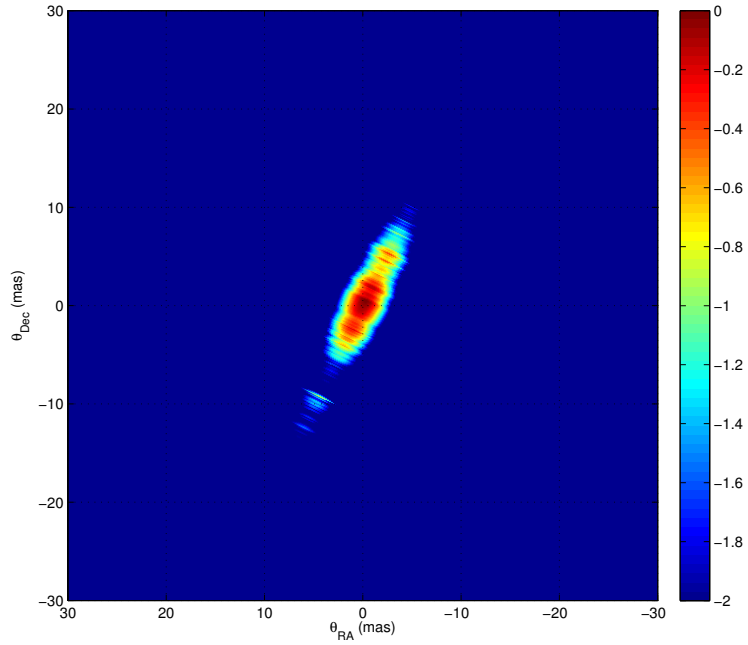

Figure 3.16: 2-D brightness image model using fitted θ_p

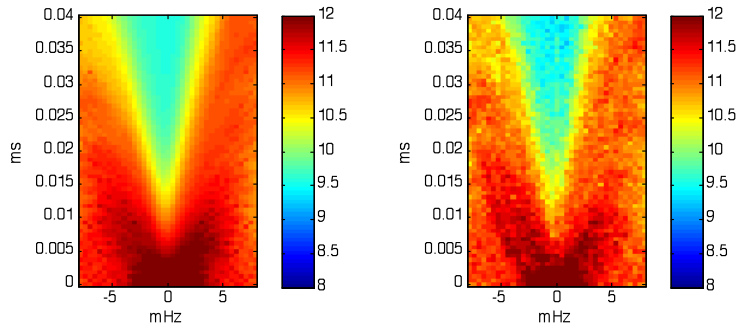

Figure 3.17: Amplitude of modeled (left) and observed (right) secondary cross spectrum

3.5 Conclusions

In chapter 2, we used astrometric imaging technique to determine the positions of offset point sources by finding apexes of reversed sub-arcs, but the center part, or called core image, is still invisible. In this chapter, We have developed a new technique to reconstruct the 2-D scattered brightness core image of pulsar

B0834+06.

We find that each point of a reversed sub-arc maps mostly from two points in core image which are symmetric to the effective velocity vector, and we invented an image recovering algorithm to reconstruct the brightness distribution of the core image from the entire sub-arc, both using instantaneous model and ensemble averaging model. Simulation shows that this technique can effectively reconstruct the scattered image with only a narrow gap along the velocity. We have applied it to the observed data and get a good estimation of constructed image from a chosen sub-arcs with high SNR. 1-dimensional brightness distribution along both parallel and perpendicular direction are estimated too, the brightness distribution along parallel direction matched the directly-sampled brightness we achieved in Chapter 2, which provides a strong proof that the way we reconstructed the core image is correct. Half-power half-width in the perpendicular direction is estimated too ($\sim 1\ mas$). We also use forward method to estimate perpendicular width of the core image, and get a similar half-power half-width.

There are some existing problems we need to solve in the future. The technique is based on the assumption that each offset bright source is infinitely small. Both data analysis and simulation result shows that some bright points must be extended and we must modify the analysis to take this size effect into account. Carefully applying this technique to multiple sub-arcs will improve the S/N of the reconstructed image as well.

Chapter 4

2-D image reconstruction based on electric field representation

In the previous chapters, we work on pulsar's secondary cross spectra, which is the 2-D Fourier transform of complex dynamic cross spectra. Pulsar dynamic spectra itself exhibit high-visibility fringes arising from interference between scattered waves, and [41] invented a method to decompose pulsar dynamic spectra into their constituent scattered waves components - amplitude $|\tilde{\mu_j}|$, Doppler shift f_{Dj} and delay τ_j. There is a direct relationship between (f_{Dj}, τ_j) and the apparent positions $\boldsymbol{\theta}$ of the scattered waves, based on the assumption that the scattering occurs in a single thin screen. We invented a method to convert the plot of $|\tilde{\mu_j}(f_D, \tau)|^2$ into a scattered brightness B($\boldsymbol{\theta}$). Since this data bypass the effect of the size of offset source, it becomes extremely interesting in the 2-D scattered image reconstruction project. The dataset we used in this chapter is from the same pulsar (B0834+06) and at the similar frequency (321MHz instead of 326MHz) as the chapter 2, but it was observed on 2004 Jan 05 with the Arecibo Radio Telescope, while the dataset in chapter 2 was observed on 2005 Nov 12 with four largest telescopes in the VLBI network.

4.1 Electric field representation of pulsar intensity spectra

Walker and Stinebring [41] defined the total electric field as $U(\nu, t)$, the total electric field intensity (or called dynamic spectra) as $I = U^*(\nu, t)U(\nu, t)$, and each of the discrete scattered waves as $\tilde{\mu_j}$, which is a complex number, and the relationship between electric field and scattered waves is defined as

$$U(\nu, t) = \sum_j \tilde{\mu_j} e^{2\pi i(\nu\tau_j + f_{Dj}t)} \tag{4.1}$$

In this equation, [41] states that the expansion sums components waves scattered with delay τ_j and Doppler shift f_{Dj} over a narrow range of t and ν, and they also assume that $\tilde{\mu_j}$ are independent of ν and t. The 2-D Fourier transform of $U(\nu, t)$

$$\tilde{U}(f_D, \tau) = \iint U(\nu, t) e^{-2\pi i(\nu\tau + f_D t)} \mathrm{d}\nu \mathrm{d}t \tag{4.2}$$

it connects to their scattered wave expansion

$$\tilde{U}(f_D, \tau) = \sum_j \tilde{\mu_j} \delta(\tau - \tau_j)\delta(f_D - f_{Dj}) \tag{4.3}$$

Beware that $\tilde{U}(f_D, \tau)$ is not secondary spectra $\tilde{I}(\Delta f_D, \Delta\tau)$ which is discussed in the other chapters. $\tilde{U}(f_D, \tau)$ is the Fourier transform of the total electric field $U(\nu, t)$ while $\tilde{I}_2(\Delta f_D, \Delta\tau)$ is from the Fourier transform of the electric field intensity $I(\nu, t)$. $I(\nu, t)$ is observable while $U(\nu, t)$ is not, and the phenomenon of scintillation arcs was recognized in the secondary spectrum $\tilde{I}(\Delta f_D, \Delta\tau)$. The arguments of $\tilde{I}_2$ are the differential delay $\Delta\tau$ ($\Delta\tau = \tau_j - \tau_k$) and differential Doppler shift Δf_D ($\Delta f_D = f_{Dj} - f_{Dk}$)between pairs of scattered waves. To simply the notation, Δ sign is usually ignored in other discussion ($\tilde{I}_2(f_D, \tau)$). In sections 4.2, the connection between secondary spectra $\tilde{I}_2(\Delta f_D, \Delta\tau)$ and the total electric filed $\tilde{U}(f_D, \tau)$ is discussed in details, so is the connection between the brightness distribution B($\boldsymbol{\theta}$) and $\tilde{U}(f_D, \tau)$

In order to represent the electric field $U(\nu, t)$ from the observed pulsar intensity spectra $I(\nu, t)$, [41] takes an iterative approach to determine $\tilde{U}(f_D, \tau)$, given $I(\nu, t)$. In this model, the individual scattered waves that make up $\tilde{U}(f_D, \tau)$ are completely specified by their delay τ_j, Doppler shift f_{Dj} , amplitude and phase $\tilde{\mu_j}$. Given a good model of electric field $U_0(\nu, t)$ they compute the corresponding intensity pattern$I_0(\nu, t)$. It wont match the observed Intensity exactly, and they improve the model by investigating the residual $R_0(\nu, t)$ between the model and the data. Assuming the existing model is a good one ($|\delta U_0| << |U_0|$) and ΔU_0 is dominated by a single scattered wave, they found a simple form

$$\delta\tilde{U}_0(f_D, \tau) = FFT(R_0(\nu, t)U_0(\nu, t)) \tag{4.4}$$

This result shows the direct relationship between the intensity residual $R_0(\nu, t)$ and $\delta\tilde{U}_0(f_D, \tau)$ given a good electric field model $U_0(\nu, t)$. They start with a good model $U_0(\nu, t)$, and keep updating $\delta\tilde{U}_0(f_D, \tau)$ by using the equation above, take the Inverse Fourier transform to get better model of $U_0(\nu, t)$, update the intensity residual $R_0(\nu, t)$, and repeat the procedure again and again, until they find a good estimate of of $\delta\tilde{U}_0(f_D, \tau)$.

Figure 4.1 shows the observed dynamic spectrum $I(\nu, t)$ [21] on the left-upper panel, and its secondary spectrum $\tilde{I}_2(\Delta f_D, \Delta\tau)$ on the left-down panel. Those reversed sub-arcs on the positive doppler side were observed to move (with pulsar proper motion) over 20 days. This is the same pulsar at different time. The right side of Figure 4.1 are calculated from the modeled 8720 decomposed scattered wave components. There is no visible difference between the observation and model which means that those 8720 scattered wave components are good estimation. Figure 4.2 shows the plot of $|\tilde{\mu_j}|^2$ versus Doppler shift and delay, the amplitudes $|\tilde{\mu_j}|^2$ of the 8720 scattered wave components was identified by the decomposition algorithm. There are no reversed sub-arc shown in Figure 4.2, because it is not secondary spectrum, it shows the scattered wave's amplitude at each each Doppler and delay. There are four individual blobs on the right side of the plot, at (15 mHz, 150 μs) , (18 mHz, 170 μs) , (22 mHz, 250 μs) and (25 mHz, 270

μs) respectively, which corresponds to those four sub-arcs in the same position of Figure 4.1.

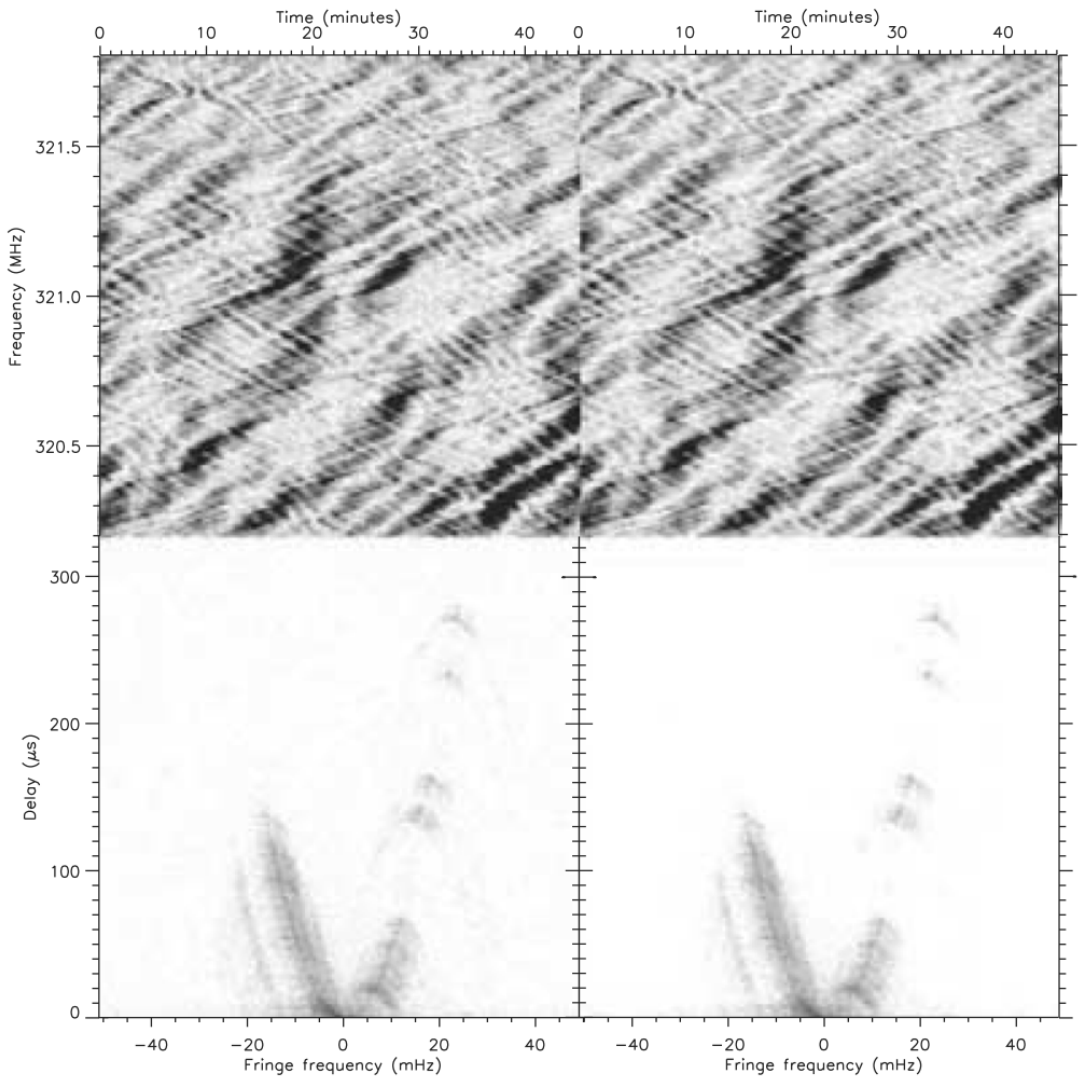

Figure 4.1: original dynamic spectrum (left-upper) of B0834+06 and its calculated secondary spectrum (left-down), the right side are calculated from the modeled 8720 decomposed scattered wave components [41]

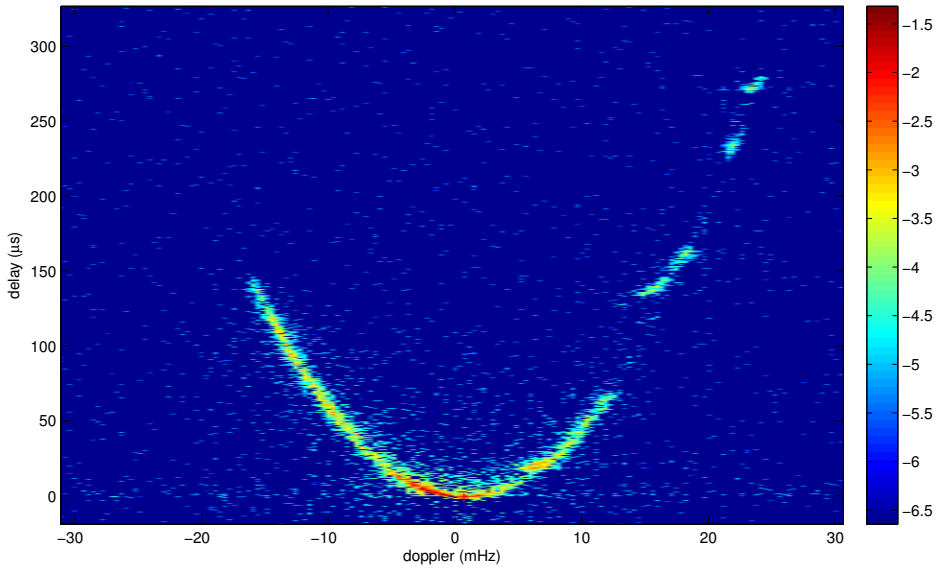

Figure 4.2: amplitudes of the 8720 scattered wave components

4.2 Converting electric field to brightness

Here we demonstrate that the coefficients $|\tilde{\mu_j}|^2$ are directly related to the scattered brightness $B(\boldsymbol{\theta}_j)$ and so we can use the amplitude obtained from the Figure 4.2 and map the position from (f_{Dj}, τ_j) to $\boldsymbol{\theta}_j$ to re-construct the 2-D brightness distribution $B(\boldsymbol{\theta})$.

To compute the secondary spectrum $\tilde{I}_2(f_D, \tau)$, we first do the 2-D Fourier transform of $I(\nu, t)$.

$$\tilde{I}(f_D, \tau) = \iint U^*(\nu, t)U(\nu, t)e^{-2\pi i(\nu\tau + f_D t)}\mathrm{d}\nu\mathrm{d}t \tag{4.5}$$

Making use of the preceding equations we get

$$\tilde{I}(f_D, \tau) = \sum_j \sum_k \tilde{\mu_j}\tilde{\mu_k}^*\delta(\tau - \tau_j + \tau_k)\delta(f_D - f_{Dj} + f_{Dk}) \tag{4.6}$$

Hence the secondary spectra $I_2(f_D, \tau) = \tilde{I}(f_D, \tau)\tilde{I}^*(f_D, \tau)$ becomes

$$\tilde{I}_2(f_D,\tau) = \sum_j \sum_k \sum_l \sum_m \tilde{\mu_j}\tilde{\mu_k}^*\tilde{\mu_l}^*\tilde{\mu_m}\delta(\tau-\tau_j+\tau_k)\delta(\tau-\tau_l+\tau_m) \\ \delta(f_D-f_{Dj}+f_{Dk})\delta(f_D-f_{Dl}+f_{Dm}) \quad (4.7)$$

The delta functions only contribute where j=l and k=m then it reduces to a double summation

$$\tilde{I}_2(f_D,\tau) = \sum_j \sum_k \tilde{\mu_j}^2\tilde{\mu_k}^2\delta(\tau-\tau_j+\tau_k)\delta(f_D-f_{Dj}+f_{Dk}) \quad (4.8)$$

By comparing this equation with the Equation 8 of [13], which expresses the secondary spectrum as a double integral over pairs of scattering angles

$$\tilde{I}_2(f_D,\tau) = \iint B(\boldsymbol{\theta}_1)B(\boldsymbol{\theta}_2)\mathrm{d}^2\boldsymbol{\theta}_1\mathrm{d}^2\boldsymbol{\theta}_2\delta(\tau-\tau_1+\tau_2)\delta(f_D-f_{D1}+f_{D2})) \quad (4.9)$$

We conclude that

$$|\tilde{\mu_j}|^2 \propto B(\boldsymbol{\theta}_j)\mathrm{d}^2\boldsymbol{\theta}_j \quad (4.10)$$

The Jacobian transform factor between $\mathrm{d}^2\boldsymbol{\theta}_j$ (or $\mathrm{d}\theta_\parallel\mathrm{d}\theta_\perp$) and $\mathrm{d}\tau\mathrm{d}f_D$ can be derived from the relationship of (τ, f_D) and $(\theta_\parallel, \theta_\perp)$

$$f_D = \frac{\boldsymbol{\theta}_j\cdot\boldsymbol{V}_{eff}}{\lambda} = \frac{\theta_\parallel V_{eff\,\parallel}+\theta_\perp V_{eff\,\perp}}{\lambda} \quad (4.11)$$

$$\tau = \frac{\theta_j^2 D_{eff}}{2c} = \frac{(\theta_\parallel^2+\theta_\perp^2)D_{eff}}{2c} \quad (4.12)$$

Before solving the Jacobian transform, we can first determine the position mapping from (τ, f_D) to $(\theta_\parallel, \theta_\perp)$ by solving the two equations above, and we get two solutions:

$$\boldsymbol{\theta}_1 = (\theta_\parallel,\theta_\perp) = (\frac{f_D\lambda}{V_{eff}}, \sqrt{U}) \quad (4.13)$$

$$\boldsymbol{\theta}_2 = (\theta_\parallel,\theta_\perp) = (\frac{f_D\lambda}{V_{eff}}, -\sqrt{U}) \quad (4.14)$$

$$U = \frac{\tau 2c}{D_{eff}} - \frac{f_D^2\lambda^2}{V_{eff}^2} \quad (4.15)$$

Where $\sqrt{U}$ is also the Jacobian factor.

In general the relationship involves the sum of brightness terms at $\boldsymbol{\theta}_1$ and $\boldsymbol{\theta}_2$. There is no baseline information in the data, so we could not solve the ambiguities of the two angular positions ($\boldsymbol{\theta}_1$ or $\boldsymbol{\theta}_2$). In our we can use the extra information from the VLBA modeling to determine, for that particular(τ, f_D) , which $\boldsymbol{\theta}$ should be used. The Jacobian transform is then

$$\mathrm{d}\theta_{\parallel}\mathrm{d}\theta_{\perp} \propto \frac{\mathrm{d}\tau \mathrm{d}f_D}{U_1} \tag{4.16}$$

So we can get

$$B(\theta_{\parallel}, \theta_{\perp}) \propto (\frac{|\tilde{\mu_j}|^2}{\mathrm{d}\tau \mathrm{d}f_D})U_1 \tag{4.17}$$

Where

$$\frac{|\tilde{\mu_j}|^2}{\mathrm{d}\tau \mathrm{d}f_D}$$

is basically the electric field amplitude in unit area, and ignore the constant, we can represent the form as

$$B(\theta_{\parallel}, \theta_{\perp}) = |\tilde{\mu_j}(f_D, \tau)|^2 \sqrt{\frac{\tau 2c}{D_{eff}} - \frac{f_D^2 \lambda^2}{{V_{eff}}^2}} \tag{4.18}$$

The data themselves can carry information about the relative Doppler-shifts, delays and phases amongst the various wave components, the choice of origin is arbitrary. In practice, the origin in time and frequency actually corresponds to the component which contains the largest flux. If there is only a single scattered term then it will be the smallest delay. However, if there are multiple scattered terms, the brightest of these might well not be the path with the smallest delay. In order to compensate this factor, a small shift (τ_0, f_{D0}) should be applied to (τ, f_D). Then some equations are changed:

$$\boldsymbol{\theta}_1 = (\theta_{\parallel}, \theta_{\perp}) = (\frac{(f_D - f_{D0})\lambda}{V_{\mathit{eff}}}, \sqrt{U}) \tag{4.19}$$

$$\boldsymbol{\theta}_2 = (\theta_{\parallel}, \theta_{\perp}) = (\frac{(f_D - f_{D0})\lambda}{V_{\mathit{eff}}}, -\sqrt{U}) \tag{4.20}$$

$$U = \frac{(\tau - \tau_0)2c}{D_{\mathit{eff}}} - \frac{(f_D - f_{D0})^2\lambda^2}{{V_{\mathit{eff}}}^2} \tag{4.21}$$

In order to make sure that $\sqrt{U}$ is real, mapping to non-negative U is valid.

4.3 Apply this algorithm to the electric field representation results

[41] achieved good estimate of the amplitudes $|\tilde{\mu_j}|^2$ of the 8720 scattered wave components. We apply our algorithm to convert $|\tilde{\mu_j}|^2$ into scattered brightness image.

According to the equations above, the position mapping depends on D_{eff}, V_{eff}, f_{D0} and τ_0. Because the data is from the same pulsar you adopted the values of D_{eff} and V_{eff} from chapter 2. We carefully adjust f_{D0} and τ_0 so that U is non-negative for all f_D and τ and chose ($f_{D0} = 0.7mHz, \tau_0 = -1.5\mu s$).

Both Figure 4.3 and Figure 4.4 show the reconstructed image. The difference between those two is that Figure 4.4 is uniformly sampled in (τ, f_D) domain while Figure 4.4 is uniformly sampled in angular domain.

In Figure 4.5, each position in angular domain is mapped to a particular position (τ, f_D). In order to estimate$|\tilde{\mu_j}|^2$, bi-linear interpolation is used. If (τ, f_D) is very close to recovery boundary, the interpolation does not work very well which makes the brightness value of the very center in Figure 4.4 lower than it should be. In Figure 4.3, no interpolation is involved, some pixels in the very center are

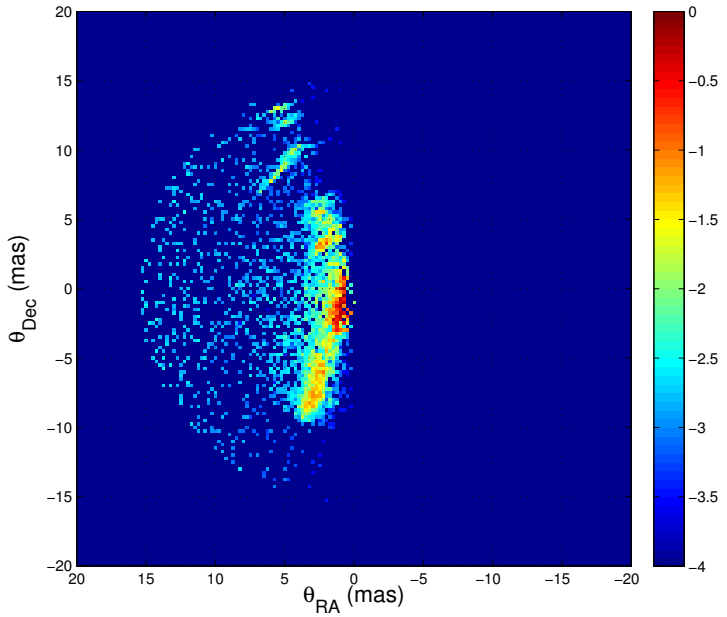

Figure 4.3: Brightness distribution $B(\boldsymbol{\theta})$, uniformly sampled in (τ, f_D) domain

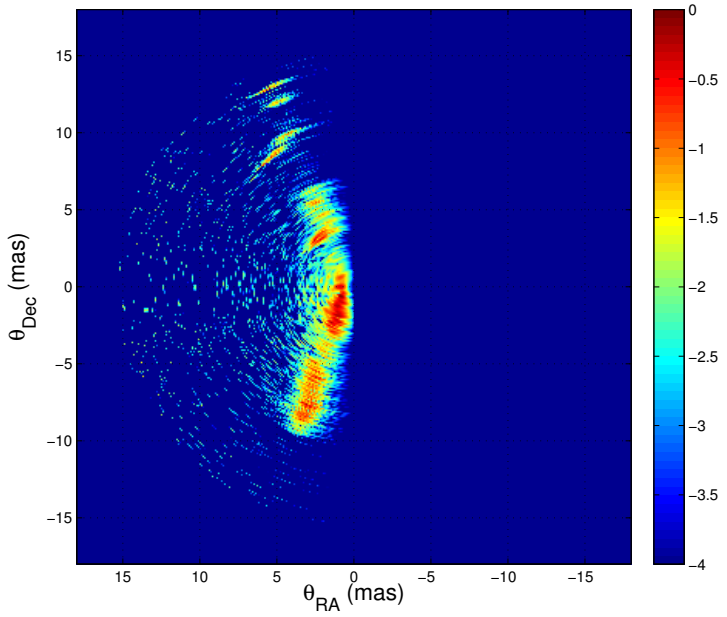

Figure 4.4: Brightness distribution $B(\boldsymbol{\theta})$, uniformly sampled in angular domain

empty which we believe is a better estimate, the bottom line is it doesnt give us the false information of the core image.

Since there is no phase information in $|\tilde{\mu_j}(f_D, \tau)|^2$, we can't solve the ambiguity. But it's the same pulsar as the one in chapter 2, just observed 22 months earlier. The estimated angle of the primary linear feature from chapter 2 matches the reconstructed primary feature in negative Dec direction. Assuming that the ISM properties are similar in those two observation, we believe that the the brightness image in the positive Dec should be flipped with axis of the parallel velocity. Since the effective velocity is very close to Dec axis, after flipping, most brightness image in the positive Dec is now on the right side. In the aid of the pre-estimated angle, ambiguity is partially solved and the corrected brightness distribution is shown in Figure 4.5. In this figure, black line presents the parallel axis estimated in Chapter 2. That black line goes through the main axis of this reconstructed brightness image after flipping. It could be possible that scattered image main axis probably didn't change much in the time span of 22 months, or they happens to be similar at those two different times.

There are some small perpendicular fluctuations along parallel axis. For example, we can see four blobs which correspond to the blobs in Figure 4.2, the one which is the most close to the origin shows a significant displacement from the axis of the image [21].

The pre-estimated angle can't help us to solve the position ambiguity of the image in the center part, because there is no phase information from this dataset and when it's close to the center, flipping can't help any more.

4.4 Conclusions

In this chapter, we use the electric field representation results from M.A. Walker and D.R.Stinebring, and convert the plot of $|\tilde{\mu_j}(f_D, \tau)|^2$ into a scattered

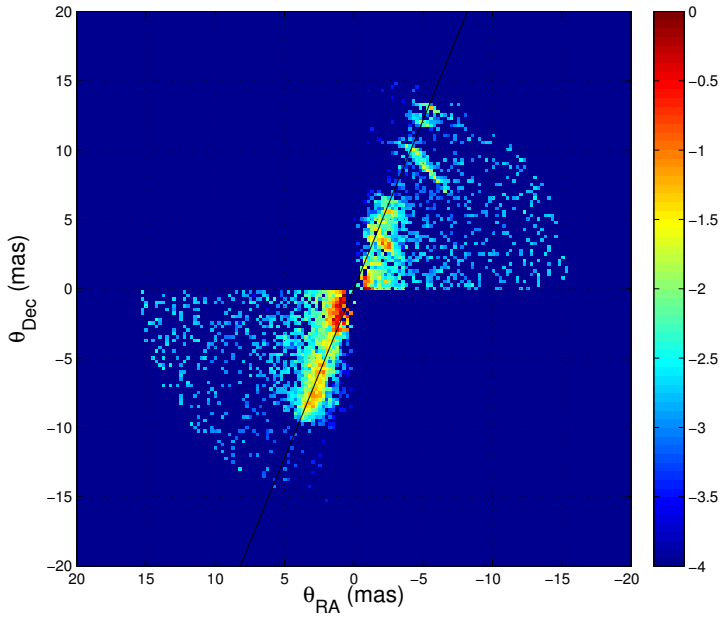

Figure 4.5: Brightness distribution $B(\boldsymbol{\theta})$, uniformly sampled in (τ, f_D) domain, flipped version of Figure 4.3

brightness B($\boldsymbol{\theta}$). Ambiguity is partially solved except the center part of the scattered brightness image, and the final brightness is shown in Figure 4.5.

The reconstructed brightness is obviously unbalanced (much brighter in the left side than the right side). We dont have a good model to fit this image yet. Its definitely not kolmogorov, nor Guassian. We are still working on it so we can estimate the axial ratio of this image.

Based on the elongated image found in chapter 2 and the knowledge that two ambiguities are symmetric to the velocity axis, we flipped the upper part of the brightness image about the velocity axis. The flipped brightness image's parallel axis shows a very tight match with the original estimated axis angle from chapter 2, which implies that the scattered image main axis didn't change much in the time span of 22 months. The perpendicular fluctuation is shown, specially by the blob at (RA=-5mas, Dec=9mas). This perpendicular fluctuation phenomenon is

observed also in the other data set that we worked in Chapter 2, 3 and 5. In Chapter 5, we work on the model with perpendicular information in it.

Chapter 5

1-D (linear) brightness image model

Both two data set of the pulsar 0834+06 implies elongated brightness images. In this chapter, we take extreme case of the model to make it a 1-dimensional, both straight-line brightness model and its modified curvi-line model are introduced. Based on those models, both primary feature and offset feature are analyzed, and their brightness distribution in both parallel $\theta_{\parallel}$ and perpendicular $\theta_{\perp}$ direction is estimated from secondary spectrum domain. Deepest gradient method and cleaning method are applied and modified to estimate brightness and $\theta_{\perp}$. $\theta_{\parallel}$ in this chapter is the same definition of Chapter 2, which is relative to the the main axis of elongated brightness image, and the dataset we use in this chapter is also the same as Chapter 2.

5.1 1-D straight-line brightness model

The easiest and most straightforward model is the 1-D straight-line brightness model. In this case, the backward position mapping from each pair of (f_D, τ) to two corresponding interference positions ($\boldsymbol{\theta}_1$,$\boldsymbol{\theta}_2$) has no ambiguity, which makes it possible to re-construct the entire secondary spectrum based on a given brightness distribution.

There are two linear components in this model: Primary linear feature and an offset linear feature. The self-interference of primary linear feature contributes the most part of the secondary spectrum except some reversed sub-arcs located around $(-40mHz, 1ms)$ in Figure 2.1 which is caused by the interference between primary linear feature and offset linear feature. Those two linear features are shown in Figure 5.1 in RA-Dec coordinate. The angle between those features and velocity is α_1 ($\alpha_1 = 25.4^o$)and $\alpha_2(\alpha_2 = 51.3^o)$ respectively which are from the estimate in Chapter 2.5.4 . The primary linear feature goes through the origin with its center at the origin. The offset features center is marked as O' in Figure 5.1 which is the closest point to the origin.

Doppler and Delay of primary feature can be expressed as

$$f_D = \frac{(\theta_{2\parallel} - \theta_{1\parallel}) \cos\alpha_1 V_{eff}}{\lambda} \tag{5.1}$$

$$\tau = \frac{(\theta_{2\parallel}^2 - \theta_{1\parallel}^2) D_{eff}}{2c} \tag{5.2}$$

Where $\theta_{1\parallel}$ and $\theta_{2\parallel}$ are two interference points along the primary feature. Doppler and Delay of offset features can be expressed as

$$f_D = \frac{(\theta_{3\parallel} \cos\alpha_2 - \theta_{1\parallel} \cos\alpha_1) V_{eff}}{\lambda} \tag{5.3}$$

$$\tau = \frac{((\theta_{3\parallel} \cos\alpha_2)^2 + (\theta_{3\parallel} \sin\alpha_2 + \theta_{\perp 0} \cos\alpha_2)^2 - \theta_{1\parallel}^2) D_{eff}}{2c} \tag{5.4}$$

Where $\theta_{1\parallel}$ is along the primary feature and $\theta_{3\parallel}$ is along the offset feature, and $\theta_{\perp 0}$ is the distance between origin and O'.

Each pair of (f_D, λ) in secondary spectrum can be treated as the integration of all interference between any legitimate pairs of B($\boldsymbol{\theta}_1$) and B($\boldsymbol{\theta}_2$). From Equation 3.52 with zero baseline, we can get the formula which relates brightness and secondary spectrum (see Equation (8) in [13]).

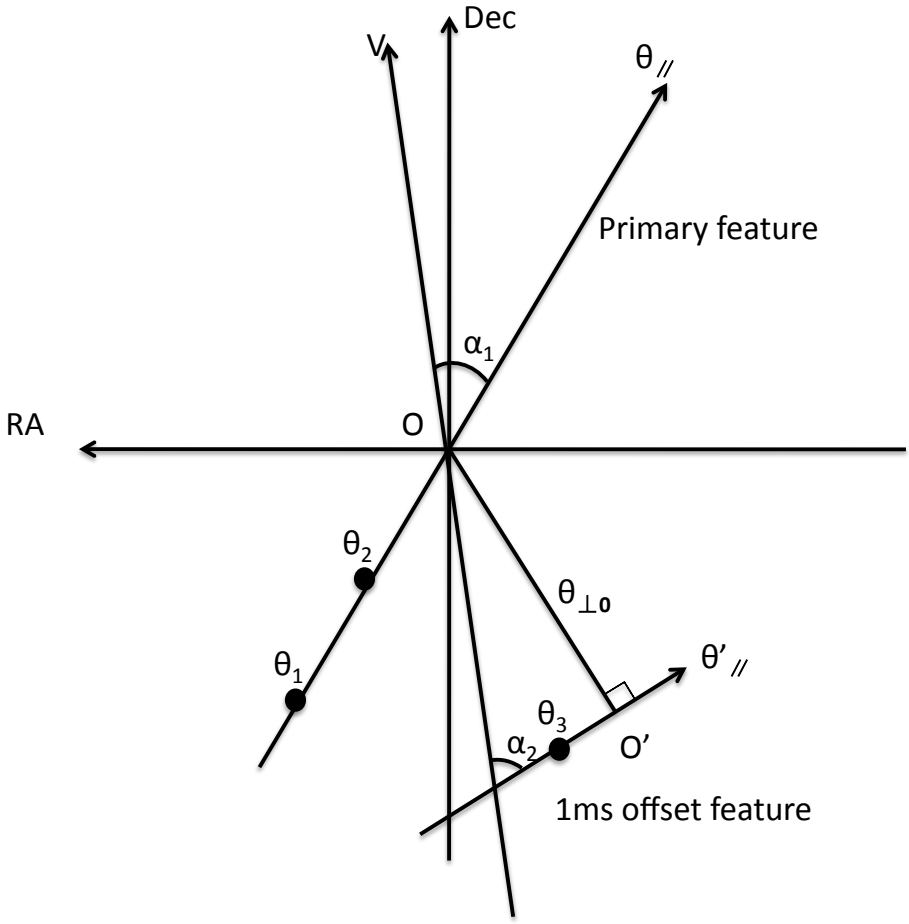

Figure 5.1: Straight-line features: A primary linear feature and an offset linear feature, the angles between those two features and velocity is α_1 ($\alpha_1 = 25.4^o$)and $\alpha_2(\alpha_2 = 51.3^o)$ respectively. The primary linear feature goes through the origin with its center at the origin. The offset features center is marked as O'.

$$\tilde{I}(f_D, \tau) = \iiiint B(\boldsymbol{\theta}_1) B(\boldsymbol{\theta}_2) \delta^2(f'_D - f_D) \delta^2(\tau' - \tau) \mathrm{d}\boldsymbol{\theta}_1 \, \mathrm{d}\boldsymbol{\theta}_2 \tag{5.5}$$

Since this is 1-D brightness model without $\theta_\perp$ fluctuation, brightness in 2-D coordinate can be expressed as $B(\boldsymbol{\theta}) = B(\theta_\parallel)\delta(\theta_\perp)$. Then equation 5.5 becomes

$$\tilde{I}(f_D, \tau) = \iint B(\theta_{1\parallel}) B(\theta_{2\parallel}) \delta(f'_D - f_D) \delta(\tau' - \tau) \mathrm{d}\theta_{1\parallel} \, \mathrm{d}\theta_{2\parallel} \tag{5.6}$$

5.1.1 Primary Linear Feature Model

For primary feature, by solving Equations 5.1 and 5.2, we get the backward position mapping equations as below

$$\theta_{1\parallel} = \frac{\tau' V_{eff} \cos\alpha_1}{f'_D D_{eff} \lambda} - \frac{f'_D \lambda}{2V_{eff} \cos\alpha_1} \tag{5.7}$$

$$\theta_{2\parallel} = \frac{\tau' V_{eff} \cos\alpha_1}{f'_D D_{eff} \lambda} + \frac{f'_D \lambda}{2V_{eff} \cos\alpha_1} \tag{5.8}$$

Based on the equations above, Jacobian J_{pf} is

$$J_{pf} = \begin{vmatrix} \frac{\delta\theta_{1\parallel}}{\delta f'_D} & \frac{\delta\theta_{1\parallel}}{\delta\tau'} \\ \frac{\delta\theta_{2\parallel}}{\delta f'_D} & \frac{\delta\theta_{2\parallel}}{\delta\tau'} \end{vmatrix} = \frac{c}{D_{eff} f'_D} \tag{5.9}$$

After applying Jacobian and integrating over $\delta()$, secondary spectrum has this very simple form based on the assumption that this is 1-dimensional structure.

$$\tilde{I}(f_D, \tau) = B(\theta_{1\parallel}) B(\theta_{2\parallel}) \frac{c}{D_{eff} f_D} \tag{5.10}$$

It shows that amplitude of each pair of (f_D, τ) comes from interference of two points at ($\theta_{1\parallel}$,$\theta_{2\parallel}$) with brightness $B(\theta_{1\parallel})$ and $B(\theta_{2\parallel})$.

5.1.2 Offset Linear Feature Model

For offset feature, by solving Equations 5.3 and 5.4, we get the backward position mapping equations as below

$$\theta_{1\parallel} = A_1 + \theta_{\perp 0} \sin\alpha_1 \cos\alpha_2 + \frac{\sqrt{A_1^2 - A_2(r^2-1) + A_3}}{r^2 - 1} \tag{5.11}$$

$$\theta_{3\parallel} = A_1 + r\theta_{\perp 0} \sin\alpha_1 \cos\alpha_2 + \frac{r\sqrt{A_1^2 - A_2(r^2-1) + A_3}}{r^2 - 1} \tag{5.12}$$

where

$$r = \frac{\cos\alpha_2}{\cos\alpha_1} \tag{5.13}$$

$$A_1 = \frac{f_D\lambda}{V_{\mathit{eff}}\cos\alpha_1} \tag{5.14}$$

$$A_2 = \frac{2\tau c}{D_{\mathit{eff}}} \tag{5.15}$$

$$A_3 = \theta_{\perp 0}^2(r^2-\cos^2\alpha_2)\cos\alpha_2^2 + \theta_{\perp 0}A_1\sin 2\alpha_2 \tag{5.16}$$

Based on the equations above, Jacobian J_{1ms} can be expressed as

$$J_{1ms} = \begin{vmatrix} \frac{\delta\theta_{1\parallel}}{\delta f_D'} & \frac{\delta\theta_{1\parallel}}{\delta\tau'} \\ \frac{\delta\theta_{2\parallel}}{\delta f_D'} & \frac{\delta\theta_{2\parallel}}{\delta\tau'} \end{vmatrix} = \frac{\lambda c}{V_{\mathit{eff}}\cos\alpha_1 D_{\mathit{eff}}\sqrt{A_1^2 - A_2(r^2-1)+A_3}} \tag{5.17}$$

After applying Jacobian and integrating over $\delta()$, secondary spectrum for offset feature has this fairly complicated form

$$\tilde{I}(f_D,\tau) = B(\theta_{1\parallel})B(\theta_{3\parallel})\frac{\lambda c}{V_{\mathit{eff}}\cos\alpha_1 D_{\mathit{eff}}\sqrt{A_1^2 - A_2(r^2-1)+A_3}} \tag{5.18}$$

5.2 Estimate 1-D brightness by sampling secondary spectrum

For initial guess of the brightness, we can sample the secondary spectrum along the forward parabolic arc.

5.2.1 Primary feature

For primary feature, apexes of sub-arcs in secondary spectrum are due to interference between the center ($\theta_{1\parallel}=0$) and offset point $\theta_{2\parallel}$. Its known that the fluctuation in perpendicular direction is small, that makes the most apexes lie on the a parabolic arc which can be expressed as

$$\tau = \frac{D_{eff}\lambda^2}{2c{V_{eff}}^2 \cos^2 \alpha_1} f_D^2 \tag{5.19}$$

Sampling along the main forward arc gives a quick and reasonable first estimate of the brightness distribution, using formula

$$B(\theta_\parallel) = \frac{\tilde{I}(f_D, \tau) D_{eff} f_D}{B(0)c} \tag{5.20}$$

Although $B(0)$ is unknown, it is a constant, variation of brightness distribution is more interesting than actual intensity level. $B(0)$ can be carefully adjusted so brightness around the center is continuous and smooth.

Secondary spectrum can be equally sampled in delay τ, Doppler frequency f_D or $\theta_\parallel$. f_D is linearly proportional to $\theta_\parallel$ which makes them the same. Since our observation data has much finer resolution in delay, equal sampling in delay gives higher resolution, except the very central part where slope of parabolic forward arc is very small. In order to get highest possible resolution in brightness domain, both sampling methods are used.

Once the highest-resolution directly-sampled brightness is achieved, re-binning and interpolation can be used to get any desired resolution. Figure 5.2 is the directly-sampled brightness distribution from secondary spectrum of pulsar B0834+06 observed by Arecibo at 322.5 MHz. Re-binning is done to reduce variations and interpolation is done to get the uniform sampling rate in $\theta_\parallel$.

The abrupt change near -10 mas shows variations on a scale as small as 0.1 mas. Variation in $B(\theta_\parallel)$ shows the evidence for scattering from a highly anisotropic turbulent electron density which is inhomogeneous on scales as small as 0.05 AU. There are other strong scattering regions such as from 3.8 to 7.5 mas.

The homogeneous part can be fitted with kolmogorov model. There are two possible models. Since this 1-D brightness model presents 2-D scattering intensity integrated along the perpendicular direction.

$$B(\theta_{\parallel}) = \int B(\theta_{\parallel}, \theta_{\perp}) \mathrm{d}\theta_{\perp} \tag{5.21}$$

If $\theta_{\parallel}$ and $\theta_{\perp}$ are independent, then $B(\theta_{\parallel}, \theta_{\perp}) = B_{\parallel}(\theta_{\parallel}) B_{\perp}(\theta_{\perp})$. After integration, $B(\theta_{\perp})\mathrm{d}\theta_{\perp}$ becomes a constant, so the approximated form of 1-D kolmogorov model is

$$B(\theta_{\parallel}) = \frac{1}{(1 + (\frac{\theta_{\parallel}}{\theta_{\parallel 0}})^2)^{\frac{11}{6}}} \tag{5.22}$$

If $\theta_{\parallel}$ and $\theta_{\perp}$ are dependent, after integrating $B(\theta_{\parallel}, \theta_{\perp})$ over $\theta_{\perp}$, the approximated form of 1-D kolmogorov model is

$$B(\theta_{\parallel}) = \frac{1}{(1 + (\frac{\theta_{\parallel}}{\theta_{\parallel 0}})^2)^{\frac{8}{6}}} \tag{5.23}$$

Non-linear least squares routine is used to fit $\theta_{\parallel 0}$ using two different models above. Residuals are data minus model in natural scale, no weighting factor is used. Figure 5.2 shows fitted 1-D kolmogorov model with index 11/6 (red curve) and model with index 8/6 (blue curve). Both sampled brightness and models are plotted in logarithm. Model 1 with index 11/6 seem to fit observation better when $\theta_{\parallel}$ is further out, which implies that for 2-D model width in $\theta_{\parallel}$ and $\theta_{\perp}$ are independent.

5.2.2 Offset Feature

For offset feature, apexes of sub-arcs are also due to interference between the center ($\theta_{\parallel} = 0$) and offset point in offset linear feature. Apexes are mostly lying on a forward arc which can be expressed as

$$\tau = \frac{D_{\mathit{eff}} \lambda^2}{2c {V_{\mathit{eff}}}^2 \cos^2 \alpha_2} (f_D - f_{D1})^2 + \tau_1 \tag{5.24}$$

where (f_{D1},$\tau 1$) corresponds to the center point O'. And using Equation 5.18 gives us the estimate of offset feature's brightness which is shown in Figure 5.3.

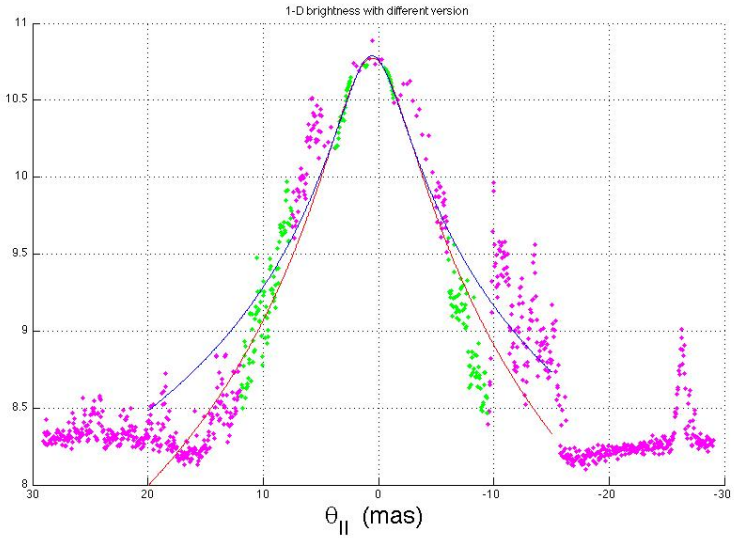

Figure 5.2: Directly sampled brightness of primary feature in logarithm ($log_{10}(B(\theta_{\|}))$), only green points are used for fitting. red curve is fitted 1-D kolmogorov model with index 11/6 and blue curve is fitted 1-D kolmogorov model with index 8/6 .

$$B(\theta_{\|}) = \frac{\tilde{I}(f_D, \tau) V_{eff} \cos\alpha_1 D_{eff} \sqrt{A_1^2 - A_2(r^2-1) + A_3}}{B(0)\lambda c} \tag{5.25}$$

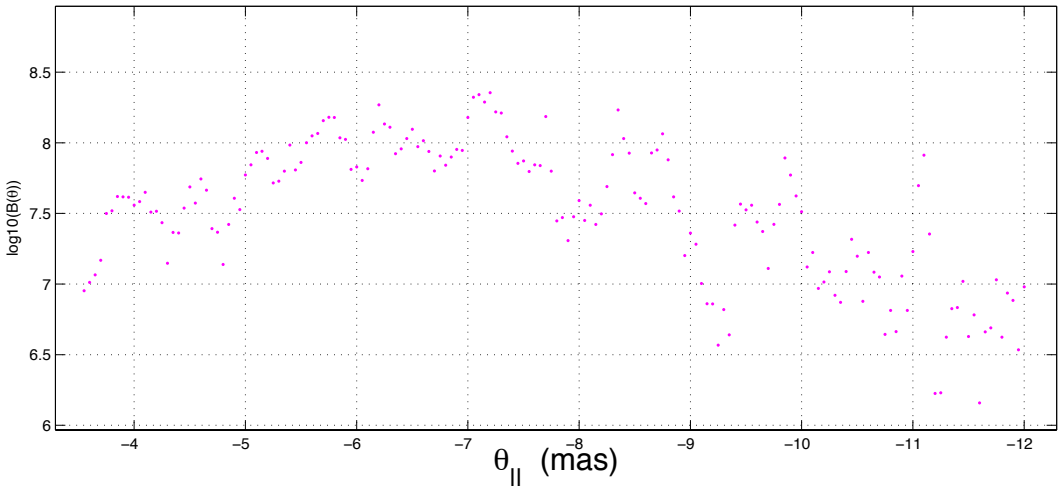

Figure 5.3: Directly sampled brightness of offset feature in logarithm ($log_{10}(B(\theta_{\|}))$), .

5.2.3 Secondary spectrum calculation from linear brightness

In this section, we calculate secondary spectrum from the directly sampled 1-D brightness from the last section. There are two steps to generate secondary spectrum from a model brightness distribution.

1. Position Mapping: Every (f_D, τ) can be mapped backward to two interference angle $(\theta_{1\parallel}, \theta_{2\parallel})$ using Equation 5.7 and 5.7 for primary feature and to $(\theta_{1\parallel}, \theta_{3\parallel})$ using Equation 5.11 5.12 for offset feature.

2. Brightness Interpolation: Linear interpolation is used to estimate the brightness at any particular $\theta_{\parallel}$ using the model brightness distribution. Using Equation 5.10 and Equation 5.18, secondary spectrum for both primary feature and offset feature can be calculated.

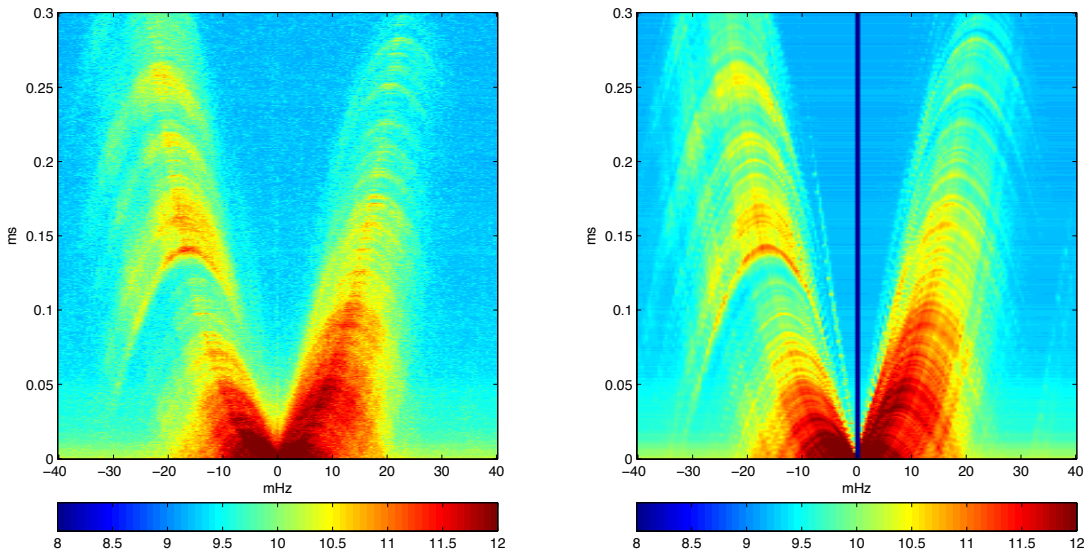

Figure 5.4: Observed Secondary Spectrum amplitude(left panel) and Modeled Secondary Spectrum amplitude(right panel), primary feature

Figure 5.4 shows the observed secondary spectrum amplitude in the left panel and calculated secondary spectrum amplitude in the right panel, both in primary feature region. They agree in considerable detail which confirms that the

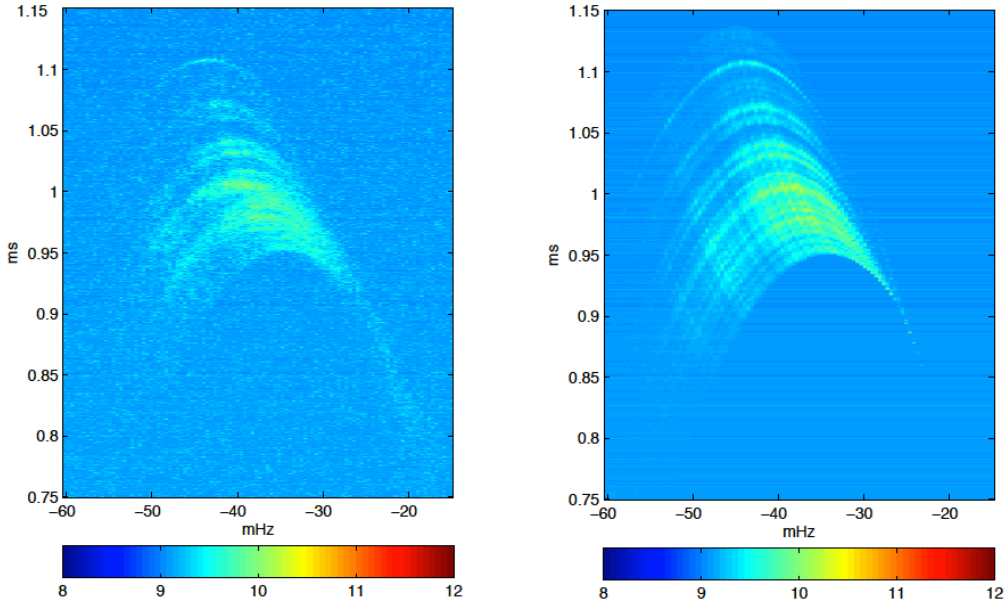

Figure 5.5: Observed secondary spectrum amplitude(left panel) and modeled secondary spectrum amplitude(right panel), offset feature

scattering is highly anisotropic. Except the central regions which have a slight difference which implies that primary linear feature have small width around the origin. Also some reversed sub-arcs are mis-matched, such as the one with apex at $(-16MHz, 0.138ms)$ which is slightly shifted to the left. It implies that the linear feature is not complete straight line.

Figure 5.5 shows the observed secondary spectrum amplitude in the left panel and calculated secondary spectrum amplitude in the right panel, both in offset feature region, at 314.5MHz. They agree in overall, but it's clear that the model still needs improvement to achieve higher agreement. For example, the observation has longer tail on the right side but the model has longer tail on the left side, and there is a small gap at $(-42MHz, 0.98ms)$ in the observation but it's filled in in the model.

5.3 1-D Curvi-line Brightness Model

By observing secondary spectrum, we notice that apexes of some sub-arcs do not lie on the main forward parabolic arc, hence that this 1 dimensional model can not be completely straight. There are some small fluctuations in perpendicular direction, as illustrated in Figure 5.6. In this section, $\theta_\perp$ is introduced to improve our linear model.

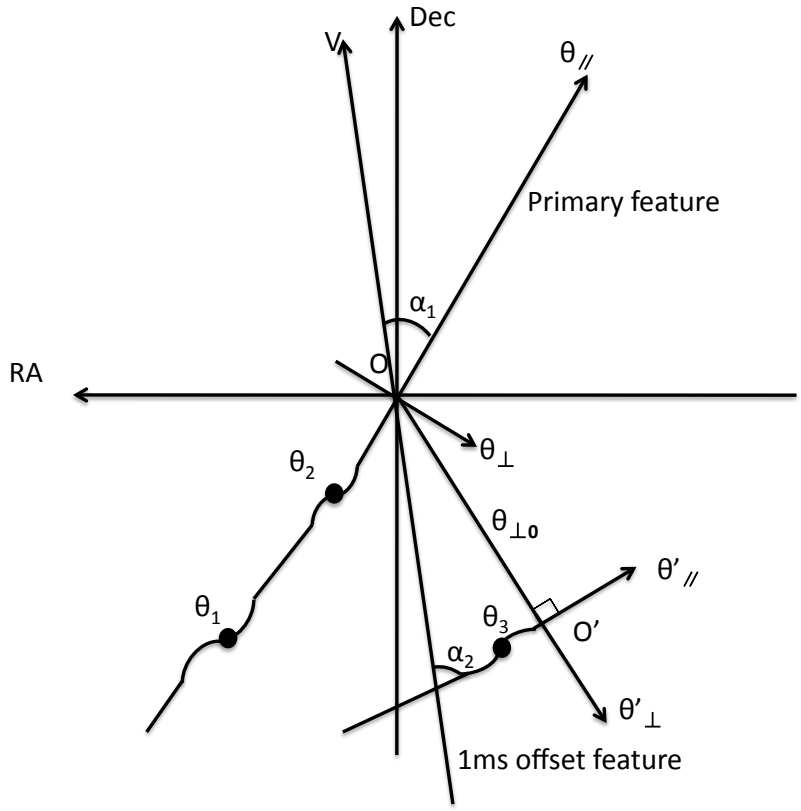

Figure 5.6: Curvi-linear features. It's the same as Figure 5.1 except that both linear features have small variation in their perpendicular direction.

Doppler and Delay of primary feature can be expressed as

$$
\begin{aligned}
f_{D2} &= \frac{(\theta_{2\parallel}-\theta_{1\parallel})\cos\alpha_1 V_{eff}}{\lambda} + \frac{-(\theta_{2\perp}-\theta_{1\perp})\sin\alpha_1 V_{eff}}{\lambda} \\
&= f_D + \Delta f_D \qquad (5.26) \\
\tau_2 &= \frac{(\theta_{2\parallel}^2-\theta_{1\parallel}^2)D_{eff}}{2c} + \frac{(\theta_{2\perp}^2-\theta_{1\perp}^2)D_{eff}}{2c} \\
&= \tau + \Delta\tau \qquad (5.27)
\end{aligned}
$$

Where $\theta_{1\perp}$ and $\theta_{2\perp}$ are small fluctuations at $\theta_{1\parallel}$ and $\theta_{2\parallel}$ along the primary linear feature.

Doppler and Delay of the offset features can be expressed as

$$
\begin{aligned}
f_{D2} &= \frac{(\theta_{3\parallel}\cos\alpha_2 - \theta_{1\parallel}\cos\alpha_1)V_{eff}}{\lambda} - \frac{(\theta_{3\perp}\sin\alpha_2 - \theta_{1\perp}\sin\alpha_1)V_{eff}}{\lambda} \\
&= f_D + \Delta f_D \qquad (5.28) \\
\tau_2 &= \frac{((\theta_{3\parallel}\cos\alpha_2)^2 + (\theta_{3\parallel}\sin\alpha_2 + \theta_{\perp 0})^2 - \theta_{1\parallel}^2)D_{eff}}{2c} \\
&\quad + \frac{(\theta_{3\perp}^2 + 2\theta_{3\perp}\theta_{\perp 0}\cos\alpha_2 - \theta_{1\perp}^2)D_{eff}}{2c} \\
&= \tau + \Delta\tau \qquad (5.29)
\end{aligned}
$$

Where $\theta_{1\perp}$ is small fluctuation along the primary feature and $\theta_{3\perp}$ is small fluctuation along the offset linear feature. The equations clearly shows the relationship between the deviation (Δf_D, $\Delta\tau$) in secondary spectrum domain and deviations ($\theta_{1\perp}, \theta_{2\perp}, \theta_{3\perp}$) in $\boldsymbol{\theta}$ domain.

5.3.1 Forward method and simulation

For straight-line brightness model, the backward position mapping from each pair of (f_D, τ) to two corresponding interference positions ($\theta_{1\parallel}$,$\theta_{2\parallel}$) has no ambiguity, but for curve-line brightness model, there is no way that backward position mapping can work, since two equations can't solve four unknown parameters. We tried simple curve-line model like sin() and without success.

The idea of forward method is, only include the effect of $\theta_\perp$ when it shifts sub-arcs, using Equation 5.26 and 5.27 . Here are the more specific steps:

1. Backward method: Start it as backward position mapping assuming there is no $\theta_\perp$. After that, a secondary spectrum is constructed based on a given straight-line linear brightness distribution using linear interpolation, as discussed in section 5.2.3

2. $\theta_\perp$ Interpolation: Using Equation 5.26 and 5.27, find the corresponding $(\Delta f_D, \Delta\tau)$ for each pair of $(f_D,\ \tau)$. During calculating $(\Delta f_D, \Delta\tau)$, interpolation is needed to estimate $\theta_\perp$ at any $\theta_\parallel$ based on a given discrete $\theta_\perp(\theta_\parallel)$ model function.

3. Shift pixel using 2-D interpolation in (f_D, τ): Shift each pixel by amount of $(\Delta f_D, \Delta\tau)$. Since $(\Delta f_D, \Delta\tau)$ are not necessarily integer times of pixel size $(\delta f_D, \delta\tau)$ and multiple pixels might be shifted to the same spot. For the first problem, we treat each original pixels as mesh grids, and after shifting a pixel, that pixel's value is relocated into those adjacent four pixel grids around (f_{D2}, τ_2), as demonstrated in Figure 5.7, by the areas of the pixel in those four adjacent pixel grids. For the second problem, make sure to accumulate the pixel value in each grid, don't do averaging, since no Jacobian effect is included.

For primary feature, according to Equation 5.26 and 5.27 , Δf_D is linear function of $\theta_\perp$, while $\Delta\tau$ is quadratic function of $\theta_\perp$, since $\theta_\perp$ is very small, then $\Delta\tau$ can be ignored compared to Δf_D. In other words, $\theta_\perp$ fluctuation along primary feature mainly moves the sub-arc horizontally.

Simulation is used to validate those equations and algorithm and is shown in Figure 5.8. The left panel shows the simulated secondary spectrum without $\theta_\perp$ after step 1, and the right panel shows the secondary spectrum after step 3. The bright sub-arc with apex located at $(-16.7mHz, 0.14ms)$ is shifted to the left side

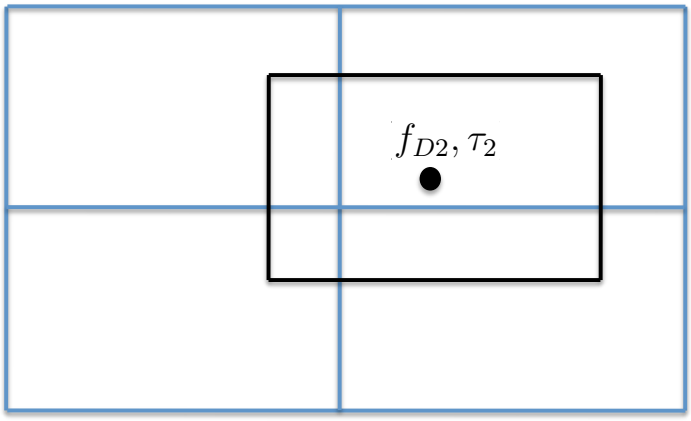

Figure 5.7: shifting pixels to (f_{D2}, τ_2)

after applying $(\Delta f_D, \Delta\tau)$. The good news about moving horizontally is that, when we continuously change $\theta_\perp$ at one specific $\theta_\parallel$, the overall change of secondary spectrum is smooth as well, so the sum of residual between the constructed secondary spectrum and observed secondary spectrum is also a continuous function of $\theta_\perp$. This is very important, since non-linear fitting algorithm use gradient to estimate the step size and and direction of the next iteration, and dis-continuous function would lead to very bad estimate of gradient and eventually blow up the fitting algorithm. For primary feature, gradient method works very well in estimating gradient, all details will be discussed in the following section.

5.4 Estimate primary feature's brightness and $\theta_\perp$

5.4.1 Least Mean Squares (LMS) Problem

Secondary spectrum generated by forward method can be treated as non-linear function of brightness distribution $B(\theta_\parallel)$ and $\theta_\perp$ distribution $\theta_\perp(\theta_\parallel)$. By minimizing the sum of square of difference between modeled secondary spectrum and observed secondary spectrum, or called evaluated function, $F(\mathbf{x})$, where $\mathbf{x}$ is a vector of discrete brightness and $\theta_\parallel$.

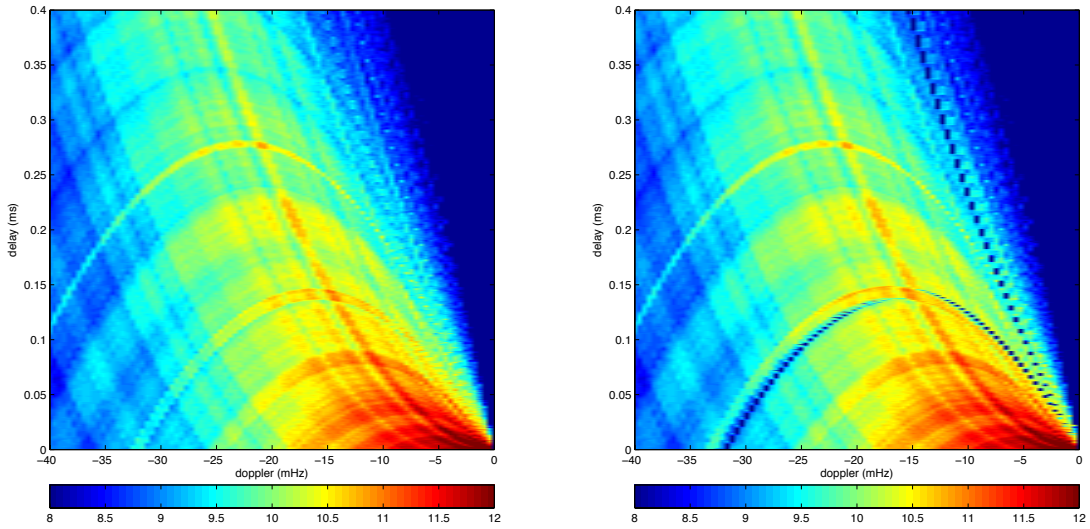

Figure 5.8: shifting pixels by$(\Delta f_D, \Delta\tau)$, the left panel is the calculated secondary spectrum using straight-line brightness and the right panel is the one using curve-line brightness.

$$minimize F(\mathbf{x}) = \sum_{i=1}^{m}(f_i(\mathbf{x}))^2 = \sum(\frac{\tilde{I}_{obs}(f_D,\tau) - \tilde{I}_{model}(f_D,\tau)}{\sigma(f_D,\tau)})^2 \tag{5.30}$$

The best estimated $B(\theta_\parallel)$ and $\theta_\perp(\theta_\parallel)$ can be achieved. Here $\tilde{I}_{obs}(f_D,\tau)$ and $\tilde{I}_{model}(f_D,\tau)$ are observed and modeled secondary spectrum respectively. Theoretically $\sigma(f_D,\tau)$ should be $\langle\tilde{I}_{obs}(f_D,\tau)\rangle$ since it's power spectrum and the standard deviation is the same as its expectation, but we only had one observation. As compromise, $\tilde{I}_{obs}(f_D,\tau)$ is used but it turned out it gives too much emphasis on the noise background. We chose to use uniform weighting in the end.

This is a non-linear least-square problem. Matlab provides a powerful tool called lsqnonlin, it includes a few common non-linear LMS algorithm, such as Gauss-Newton method and Levenberg-Marquardt method. Gauss-Newton method provides quadratic convergence and Levenberg-Marquardt method is a more efficient version of Gauss-Newton method. Both methods are good in the final stage of the iterative process. We got very convincing fitting result using lsqnonlin when straight-line brightness distribution is fitted. But when $\theta_\perp$ is included, lsqnonlin

doesn't work well. Quadratic convergence makes the small dis-continuousity even worse, Plus there isn't any easy way to adjust the step size using lsqnonlin, it might be true that the initial step size is too big. Lsqnonlin is an easy and reliable tool most of time, but it's clear that it can't deal with case like our curvi-line brightness model.

We used a gradient method combined with line search method. Gradient method works better if the initial guess $\mathbf{x}_0$ is far away from minimizer $\mathbf{x}^*$. And we can always change step size or stop criteria. Below is a detailed discussion on gradient method and line search method.

5.4.2 Gradient method

Gradient method, or called steepest descent methods, is a very common method to solve LMS non-linear problem. It's an iterative process: From a starting point $\mathbf{x}_0$, the method produces a series of vector $\mathbf{x}_1$, $\mathbf{x}_2$, ..., which converges to $\mathbf{x}^*$, a local minimizer. The descending condition is

$$F(\mathbf{x}_{k+1}) < F(\mathbf{x}_k) \tag{5.31}$$

Each iteration consists in:

1. Find a descent direction $\mathbf{h}$
2. Find a step length ratio α giving a good decrease in the F-value.
3. Update $\mathbf{x}$ with $\mathbf{x} + \alpha\mathbf{h}$ if the descending condition is satisfied.

We assume that $F(\mathbf{x})$ is differentiable and smooth so that the below Taylor expansion is valid

$$F(\mathbf{x} + \alpha h) = F(\mathbf{x}) + \alpha\mathbf{h}^T\mathbf{F}'(\mathbf{x}) + O(\alpha^2) \tag{5.32}$$

where gradient vector $\mathbf{F}'(\mathbf{x})$

$$\mathbf{F}'(\mathbf{x}) = \begin{bmatrix} \frac{\partial F(\mathbf{x})}{\partial x_1} \\ \frac{\partial F(\mathbf{x})}{\partial x_2} \\ \cdots \end{bmatrix} \tag{5.33}$$

The relative gain in function value $F(\mathbf{x})$ satisfies

$$\lim_{\alpha \to 0} \frac{F(\mathbf{x}) - F(\mathbf{x} + \alpha h)}{\alpha ||\mathbf{h}||} = -\frac{\mathbf{h}^T}{||\mathbf{h}||}\mathbf{F}'(\mathbf{x}) = -||\mathbf{F}'(\mathbf{x})|| \cos\theta \tag{5.34}$$

Where θ is the angle between vector $\mathbf{h}$ and $\mathbf{F}'(\mathbf{x})$. This means that the steepest descent direction $\mathbf{h}_{sd}$ is given when $\theta = \pi$

$$\mathbf{h}_{sd} = -\mathbf{F}'(\mathbf{x}) \tag{5.35}$$

Gradient method is often very slow since the convergence is linear, but it has good performance in the initial stage of iterative process since its more reliable and robust. We usually combine it with a line search method which is discussed later.

5.4.3 Line search method

Line search method is usually combined with gradient method to solve LMS nonlinear problem. In each iteration step, given a descent direction $\mathbf{h}_{sd}$, it moves from $\mathbf{x}$ in step size $\alpha\mathbf{h}_{sd}$. α is a really important parameter. When α is too small, the convergence is too slow, α should be increased. When α is too big, then its possible that the new $\mathbf{x}$ is too far from the other side of the minimum, descending condition wont be satisfied, α should be decreased. When α is close to the minimizer, accept this α value. Line search method provides a way with adaptive α.

While realizing this method with gradient method for our specific case, there are some parameters we need to choose carefully.

1. Gradient step size dx: dx is used when estimating $\frac{\partial F(\mathbf{x})}{\partial x_i} \approx \frac{F(x_i+dx)-F(x_i-dx)}{2dx}$, we find 0.1-0.3 mas for $\theta_\perp$ and 0.2-0.4 for $log_{10}(B(\theta_\parallel))$ are pretty reasonable

gradient step sizes.

2. Stop criteria: Maximum iteration times k_{max} and two thresholds (ε_1, ε_2). when gradient magnitude is smaller than ε_1, or the magnitude of change in $\mathbf{x}$ is smaller than ε_2, or the iterate reaches k_{max}, we terminate the iterations.

3. Initial step length ratio α: Step length ($\alpha\mathbf{h}$) is increment or decrement in $\mathbf{x}$ in each iteration, which is a totally different definition from step size dx which is used to estimate gradient.

The flowchart below shows how this method works with gradient method.

First initialize dx, α, k_{max},ε_1 and ε_2, and set v=2. v is used to control the step length in each iteration. When k is smaller than k_{max}, first estimate $\mathbf{F}'(\mathbf{x})$ and $\mathbf{h}_{sd}$.

If $||\mathbf{F}'(\mathbf{x})|| < \varepsilon_1$ or $||\mathbf{h}_{sd}|| < \varepsilon_2$, terminate the iteration. If not, check if the mean squared residual is lower than the previous valid one. If not, it means that the step length is too big, so decrease v by half and re-estimate $||\mathbf{F}'(\mathbf{x})||$ and $\mathbf{h}_{sd}$, and do it several times until the mean squared residual is lower. Then accept this new $\mathbf{x}$, reset v back to 2, and start another iteration again.

In our case, the initial step length ratio α is the most important parameter. Too small α needs too many iterations, since the convergence is too slow. If α is too big, then we waste a lot of iterations trying to decrease v by half.

5.4.4 Pre-scale

We need fit both both Brightness and $\theta_\perp$, and their value ranges are different from each other. Inside one parameter set, like Brightness at different $\theta_\parallel$, or $\theta_\perp$ at different $\theta_\parallel$, we want similar step lengths too, otherwise they converges at different speed and changing v (v is a scalar for all parameters) wont help us find an appropriate step length for all parameters in that set. In order to solve this problem, pre-scale is very important. Pre-scale factor can be applied to fitted parameter $\mathbf{x}$, or step length $\mathbf{h}_{sd}$. Here we apply it to step length.

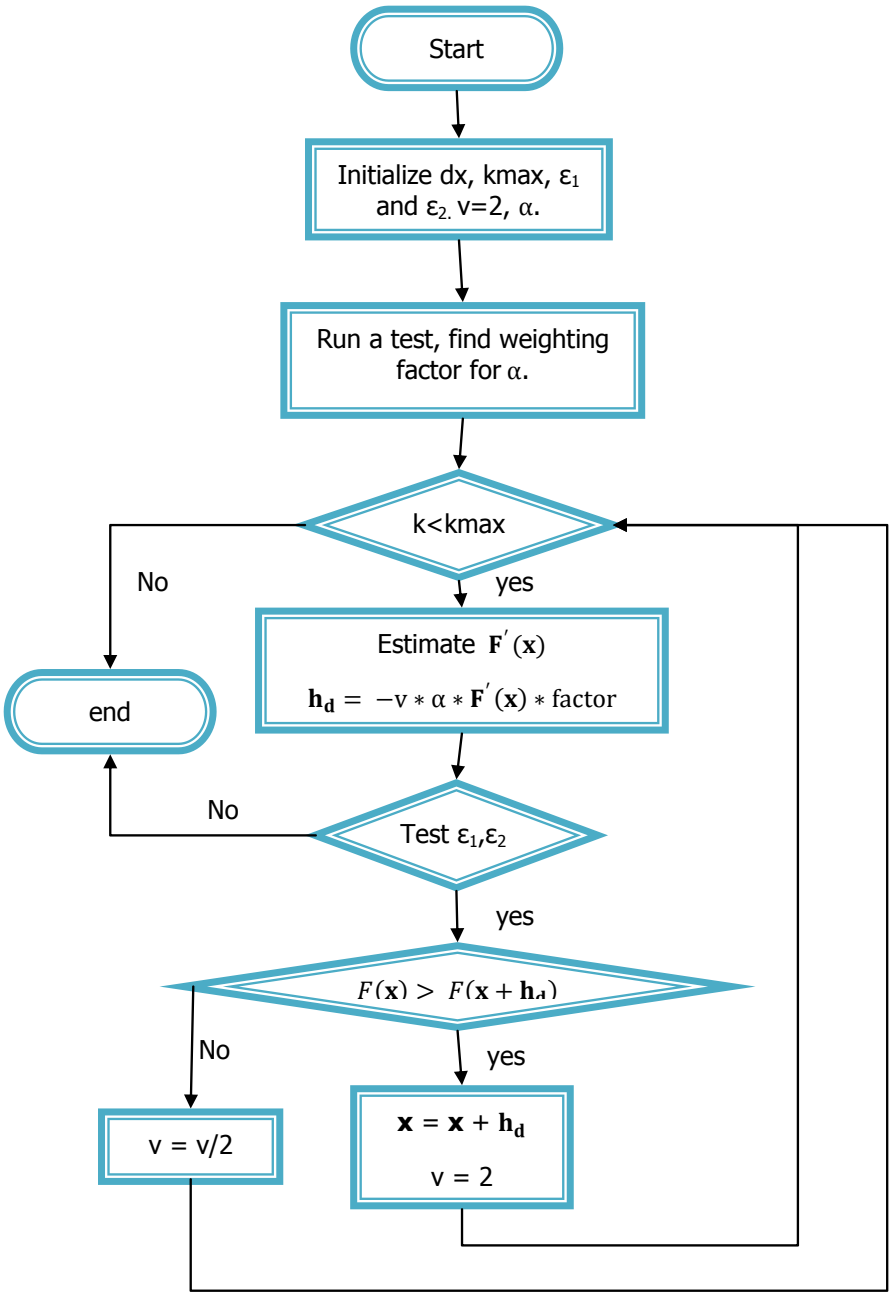

Figure 5.9: flowchart of gradient method

Step length can be expressed as

$$\mathbf{h}_{sd} = -v * \alpha * \mathbf{F}'(\mathbf{x}) * ScaleFactor \tag{5.36}$$

Scale factor is chosen so that based on the first estimate $\mathbf{F}'(\mathbf{x}_0)$, average

$\mathbf{h}_{sd}$ in each block with size of 10 parameters is equal to 0.1 for Brightness and 0.05 mas for $\theta_\perp$. The estimated $\mathbf{F}'(\mathbf{x}_0)$, using $\frac{F(x_i+dx)-F(x_i-dx)}{2dx}$ might not be accurate that's why averaging of size of 10 is used to decrease the variance of the estimate.

5.4.5 Simulation

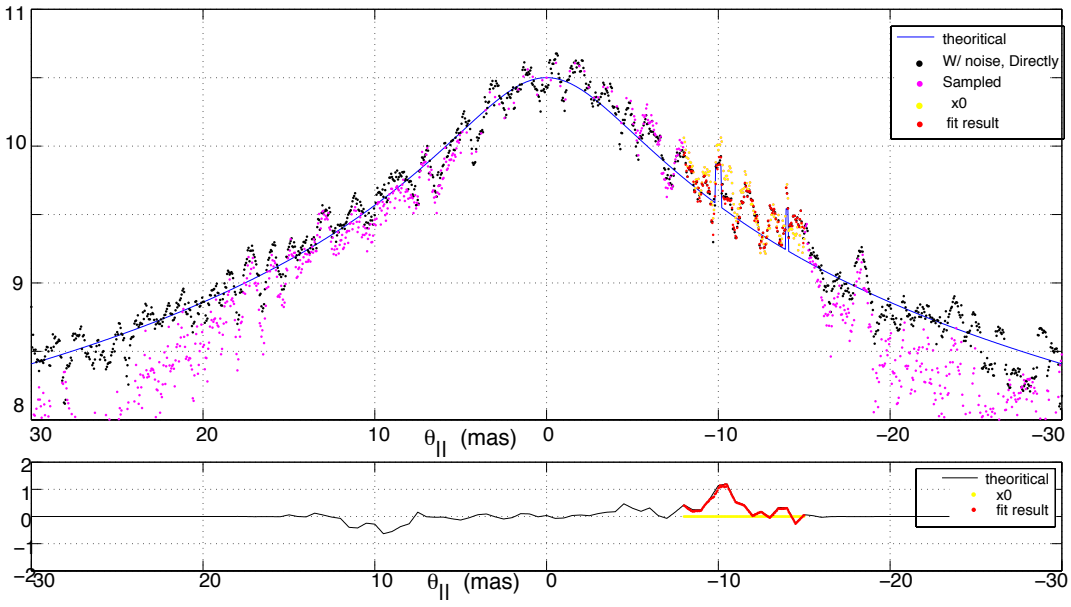

Figure 5.10: Brightness (upper panel, y axis is in logarithm scale($\log 10(B)$) and $\theta_\perp$ (lower panel, y-axis is in unit of mas)). Black line is the upper panel is the input theoretical 1-D kolmogrov model with two spikes and noise, magenta line is the directly-sampled brightness, yellow line is the initial guess and red line is the fitting result. In lower panel, black, yellow and red also represent the input, initial guess and fitting result of $\theta_\perp$

Since we don't know the actual $B(\theta_\parallel)$ and $\theta_\perp(\theta_\parallel)$, It's impossible to tell if the fitting is successful or not. That's why before we apply those algorithms directly to the observed data, simulation is needed to test the algorithms first. If the fitting result match the input $B(\theta_\parallel)$ and $\theta_\perp(\theta_\parallel)$, then the algorithm works.

A simulated 'observed' secondary spectrum is first generated using 'known' $B(\theta_\parallel)$ and $\theta_\perp(\theta_\parallel)$. Figure 5.10 shows the known $B(\theta_\parallel)$ in the upper panel and $\theta_\perp(\theta_\parallel)$ in the lower panel. The known $B(\theta_\parallel)$ which is marked in black is generated

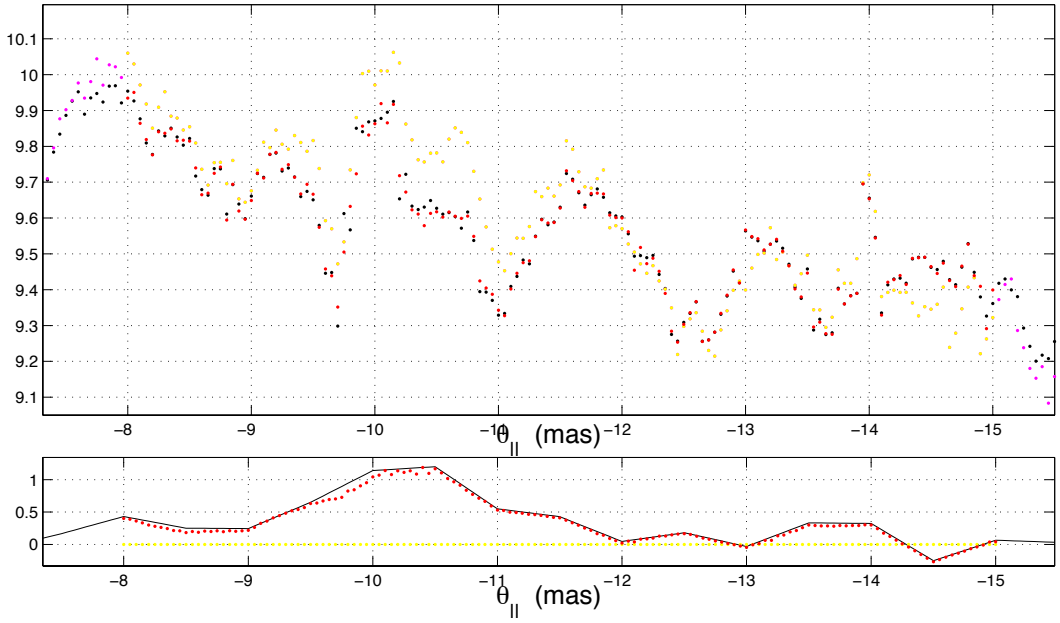

Figure 5.11: zoomed in version of Figure 5.10

by using a theoretical 1-D kolmogrov model with two spikes at -10 mas and -14 mas, and multiplied with chi-square noise of k=2 which is shown as ripples. The known $\theta_\perp(\theta_\parallel)$ is generated from a smoothed version of the individual identified apexes which are estimated in Chapter 2. we add a small fluctuation on brightness and use it as initial guess of brightness $\mathbf{x}0$, and zero as initial guess of $\theta_\perp(\theta_\parallel)$, both of them are marked in yellow. The fitting region is [-15 -8] mas. The fitting result is marked in red using gradient and line search method. Those red dots (fitting result) lays on black dots (input) which indicates that the gradient method with linear search method converge to the minimizer $\mathbf{x}^*$. Figure 5.11 is the zoomed in version of Figure 5.10 so details can be shown, fitting result is very close to the input $B(\theta_\parallel)$ and $\theta_\perp(\theta_\parallel)$.

Figure 5.12 shows the simulated 'observed' secondary spectrum and modeled secondary spectrum with fitted $\mathbf{x}^*$. They only show the region that corresponds to the fitting region in $B(\theta_\parallel)$ and $\theta_\perp(\theta_\parallel)$ as marked as Figure 5.10. simulated 'observed' secondary spectrum and modeled secondary spectrum with fitted

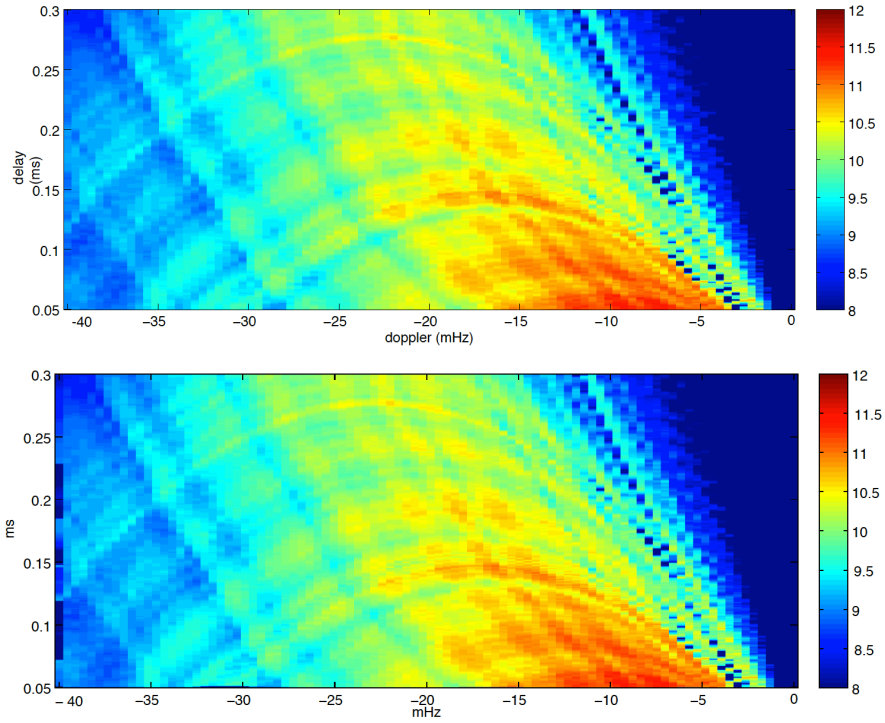

Figure 5.12: *upper:* simulated 'observed' secondary spectrum. *lower:* modeled secondary spectrum with fitted $\mathbf{x}^*$.

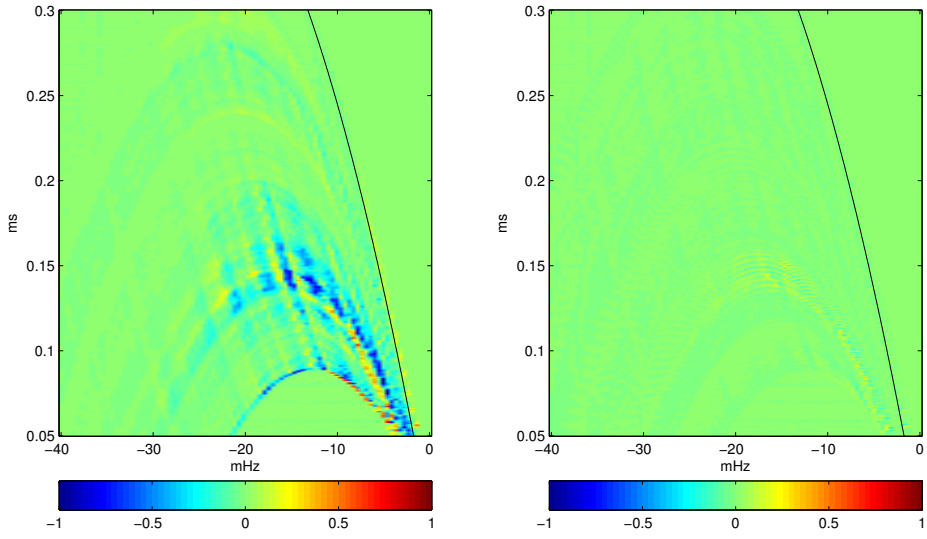

Figure 5.13: Residual before and after fitting

$\mathbf{x}^*$ are very much alike. Left panel in Figure 5.13 shows the normalized residual between 'observed' secondary spectrum and modeled secondary spectrum with $\mathbf{x}_0$ before fitting and right panel shows the residual after fitting. It's normalized by a constant so the residual is between -1 and 1. The mean of squared residual after fitting is reduced from 0.087 to 0.026.

5.4.6 Primary feature fitting result

Simulation proves that the fitting algorithm converges and we apply it to the real observed secondary spectrum data.

Figure 5.14 shows the amplitude of observed secondary spectrum of Pulsar B0834+06 at 326MHz with 4 channels of total 32MHz bandwidth.

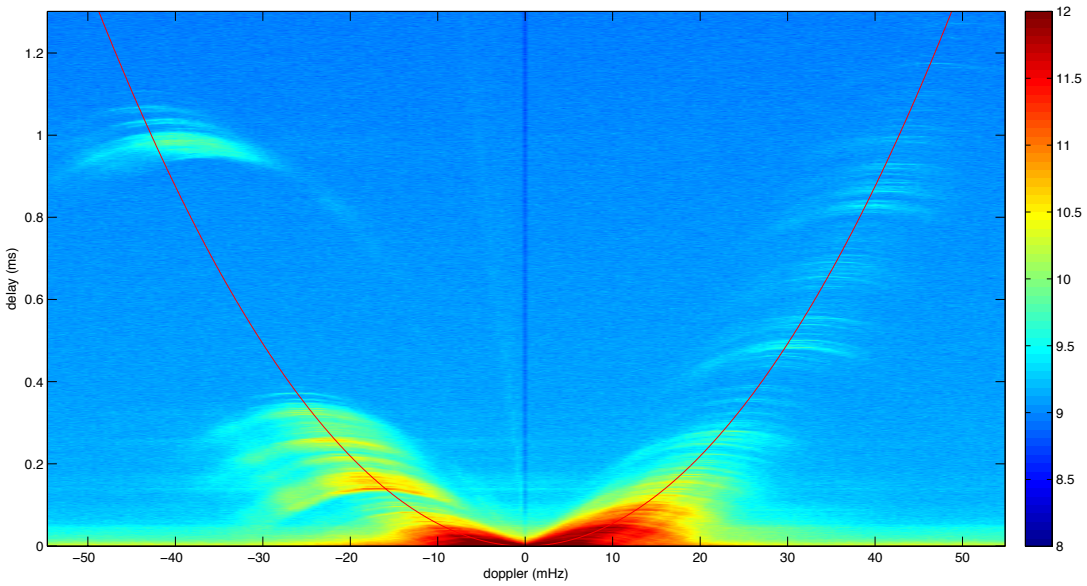

Figure 5.14: Observed Secondary spectrum of Pulsar B0834+06 at 326MHz with 4 channels of total 32MHz bandwidth

Figure 5.15 shows the fitted $B(\theta_\parallel)$ and $\theta_\perp(\theta_\parallel)$. In the upper figure, dots in magenta are sampled brightness, dots in yellow are the initial guess of brightness and dots in red are fitted brightness using gradient and line search method. In

the lower figure, dots in yellow are zeros initial value for $\theta_\perp(\theta_\parallel)$ and red dots are fitting result. The fitted $\theta_\perp(\theta_\parallel)$ matches the identified apexes positions, the latter is shown in Figure 5.10. It's a good evidence that the fitting was a success.

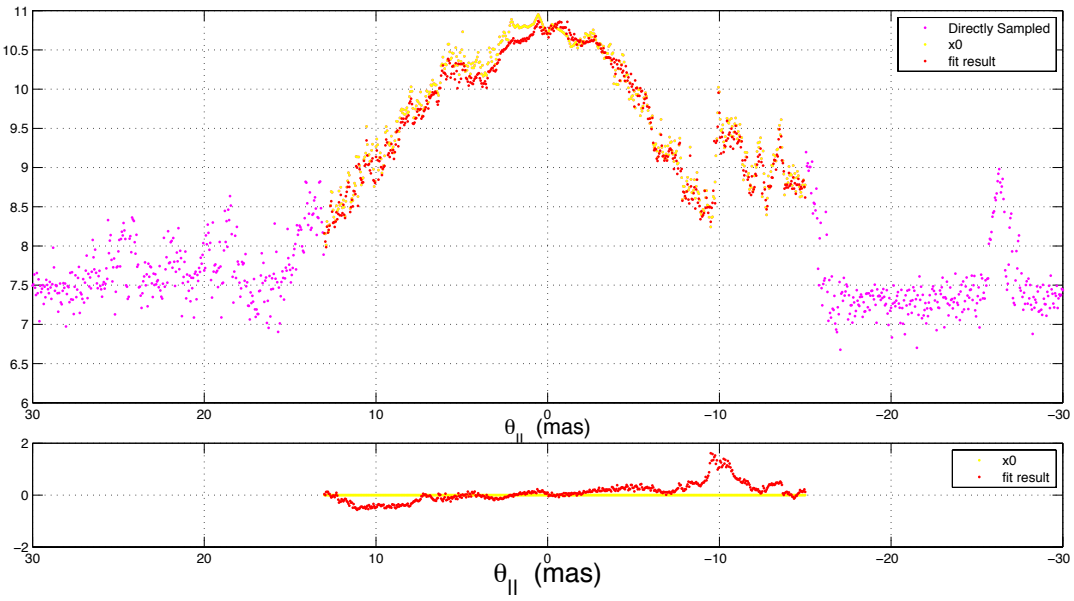

Figure 5.15: Brightness (the upper panel, y axis is in logarithm scale($\log 10(B)$) and $\theta_\perp$ (lower panel, y-axis is in unit of mas)). Magenta dots are the directly-sampled brightness, yellow dots are the initial guess and red dots are the fitting result. In the lower panel, yellow and red also represent the initial guess and fitting result of $\theta_\perp$

Figure 5.16 shows the modeled secondary spectrum with fitted $B(\theta_\parallel)$ and $\theta_\perp(\theta_\parallel)$ and Figure 5.17 shows residual before (left panel) and after fitting(right panel). The fitting is done in the entire secondary spectrum but Figure 5.16 and Figure 5.17 only show part of it. The mean of squared residual after fitting is reduced by about 75 percent, which is from 0.1516 to 0.03846.

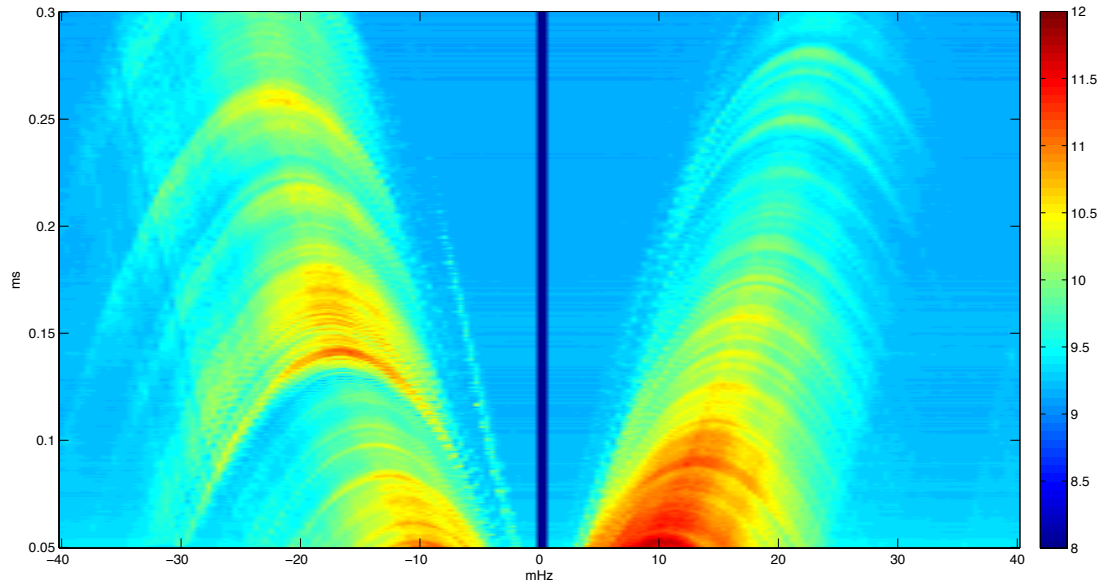

Figure 5.16: Modeled Secondary spectrum with fitted $B(\theta_{\parallel})$ and $\theta_{\perp}(\theta_{\parallel})$

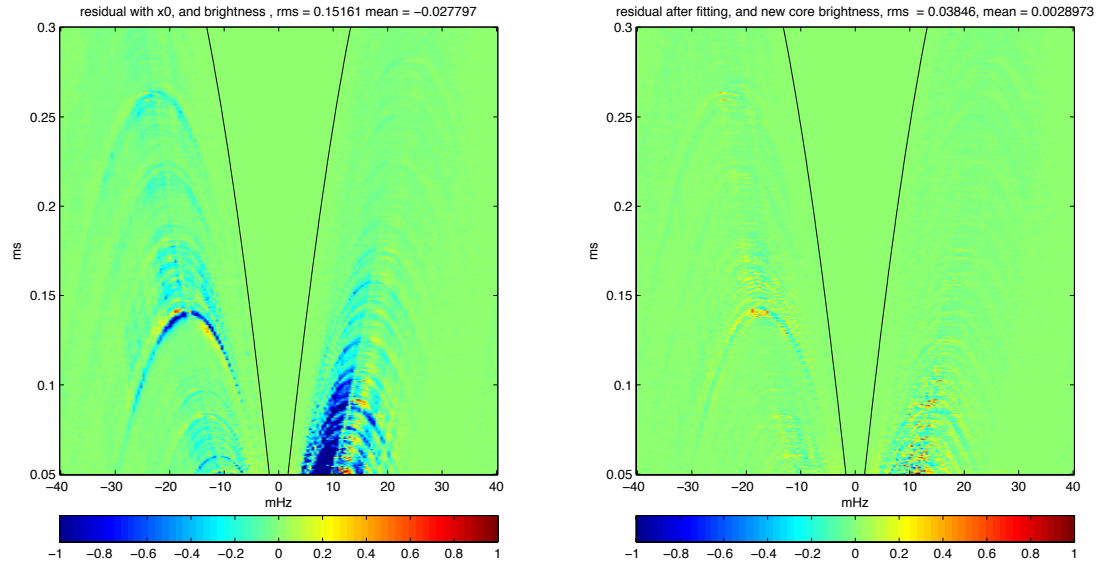

Figure 5.17: Residual before and after fitting

Figure 5.18 presents the $\theta_{\perp}(\theta_{\parallel})$ in $\boldsymbol{\theta}$ domain. The peak of $\theta_{\perp}$ is $\sim 1\ mas$, but in $-30\ mas$ to $30\ mas$ region its not a big fluctuation, which is better illustrated in this figure.

All figures above provide a very strong evidence that the primary feature

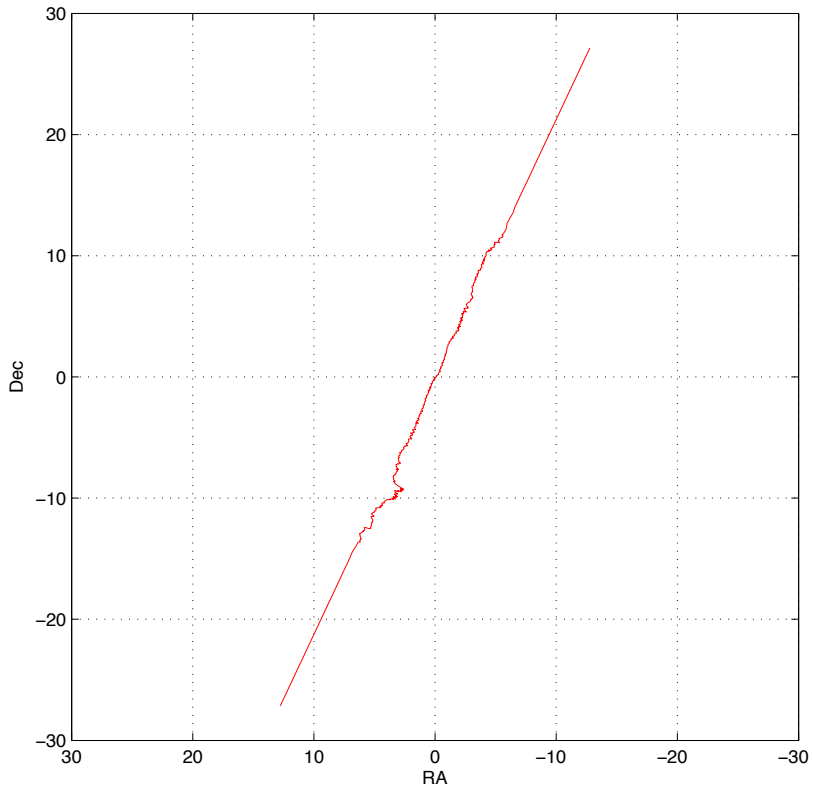

Figure 5.18: $\theta_\perp(\theta_\parallel)$ in RA-Dec coordinates, in unit of *mas* in both coordinates

part of this interstellar medium's structure is very close to a curvi-line with brightness distribution as shown in Figure 5.15. And the peak in $B(\theta_\parallel)$ at $\theta_\parallel = -10$ has the biggest $\theta_\perp$.

5.5 Estimate offset feature's brightness and $\theta_\perp$

For offset feature, according to Equation 5.28 and 5.29, because of the term $2\theta_{3\perp}\theta_{\perp 0}\cos\alpha_2$, $\Delta\tau$ is also linear function of $\theta_\perp$ after ignoring the higher order terms, and $\theta_{\perp 0}$ is a big number which makes $\Delta\tau$ the dominant term. In other word, $\theta_\perp$ fluctuation along offset feature mainly moves the sub-arc vertically. This phenomena makes a big difference when we fit the $\theta_\perp$ using forward method. Details will be discussed in the following sections.

Before we jump to fitting offset feature's brightness and $\theta_\perp$, let's look at the observed offset feature in the secondary spectrum domain of Pulsar B0834+06, the same data set of chapter 2, 3 and earlier sections of this chapter.

5.5.1 Offset feature in different frequency channel

Primary feature in secondary spectrum shown earlier are from the dynamic spectrum of four 8MHz bandwidth sub-channels, with center frequency at 314.5MHz (channel 1), 322.5MHz (channel 2), 330.5MHz (channel 3) and 338.5MHz (channel 4), or in other words, from a 32MHz bandwidth centered at 326.5MHz. We check primary feature's secondary spectrum in each sub-channel, and there are no obvious difference. But there are differences for offset feature.

In Figure 5.19 to Figure 5.22, four sub-channels are plotted separately. It's clear that offset feature varies significantly between different channels. For example, In channel 4, there is no thin sub-arcs above 1 ms, but in channel 1 there are five thin sub-arcs, one at $1.1ms$, two around $1.05ms$, and another two around $1.07ms$. In channel 2, there are four thin sub-arcs above 1 mas, the one at $1.1ms$ disappears. In channel 3, those four sub-arcs in channel 2 merge into two sub-arcs, but the thick sub-arc at $1ms$ is the strongest comparing to the other three channels. There are more differences if you keep searching.

We still don't understand why offset feature varies so much at different frequency. From results of Chapter 2 we expected that the scattered image is independent with frequency. This is still an unsolved puzzle for future research.

5.5.2 Cleaning Method

The gradient method can perfectly recover brightness alone for offset feature. But once $\theta_\perp$ is involved, even a small change in initial guess leads to a totally

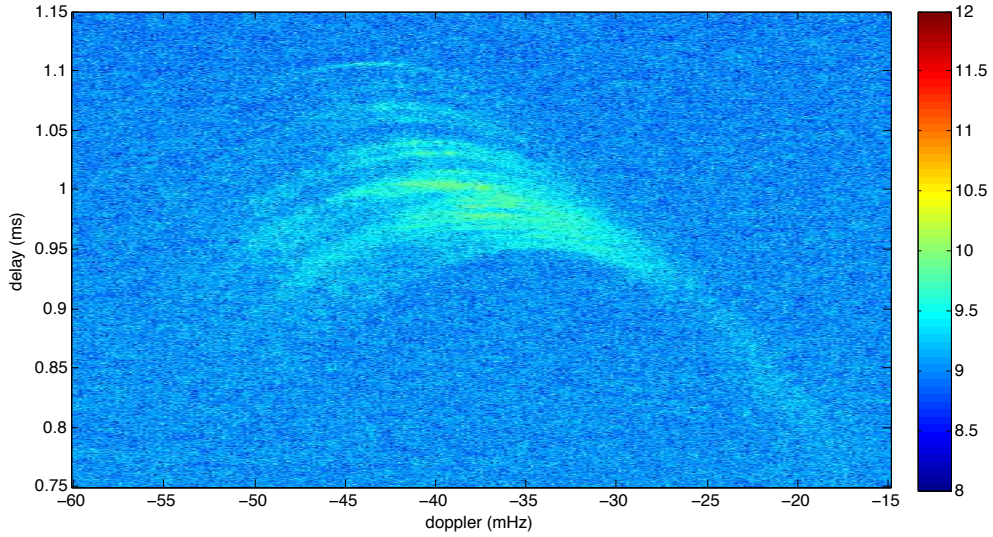

Figure 5.19: Offset feature at 314.5MHz, the intensity is in log_{10} scale

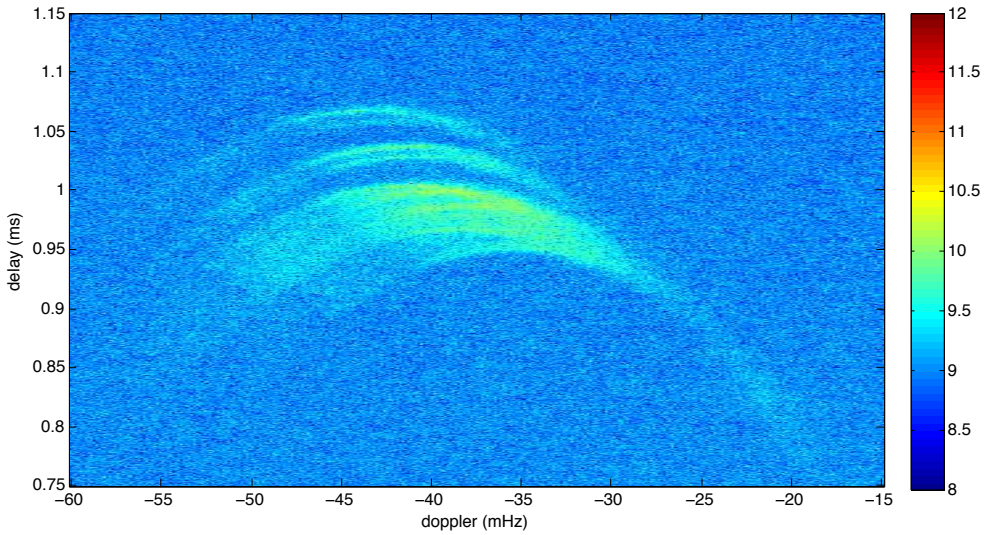

Figure 5.20: Offset feature at 322.5MHz, the intensity is in log_{10} scale

different fitting result which clearly implies that this method doesn't converge.

Gradient method only works when the evaluated function, $F(\mathbf{x})$, is a continuous function of $\mathbf{x}$. For primary feature, $F(\mathbf{x})$ is a smooth function of both brightness and $\theta_\perp$, while for offset feature, $F(\mathbf{x})$ is only a smoothed function of brightness. The reason is: due to geometry, $\theta_\perp$ fluctuation along primary feature

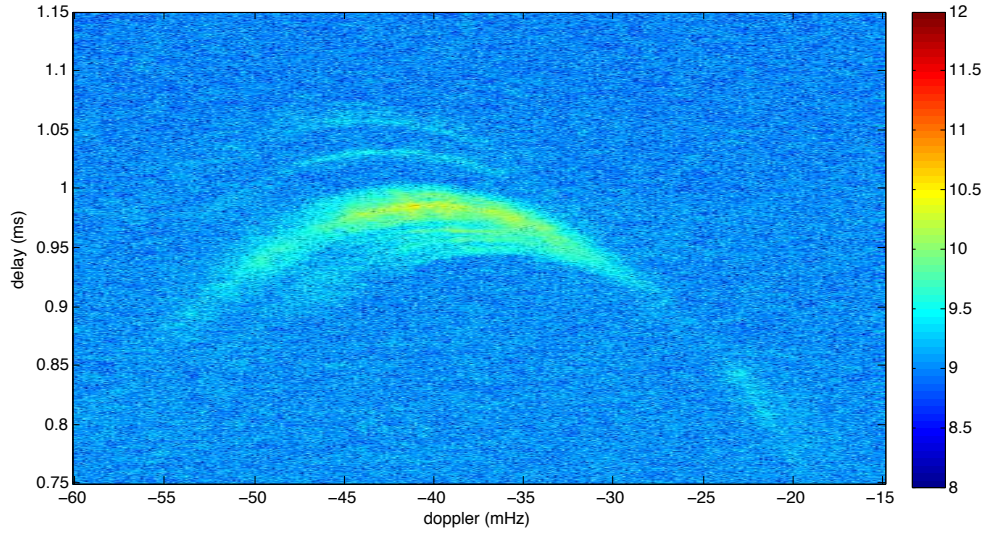

Figure 5.21: Offset feature at 330.5MHz, the intensity is in log_{10} scale

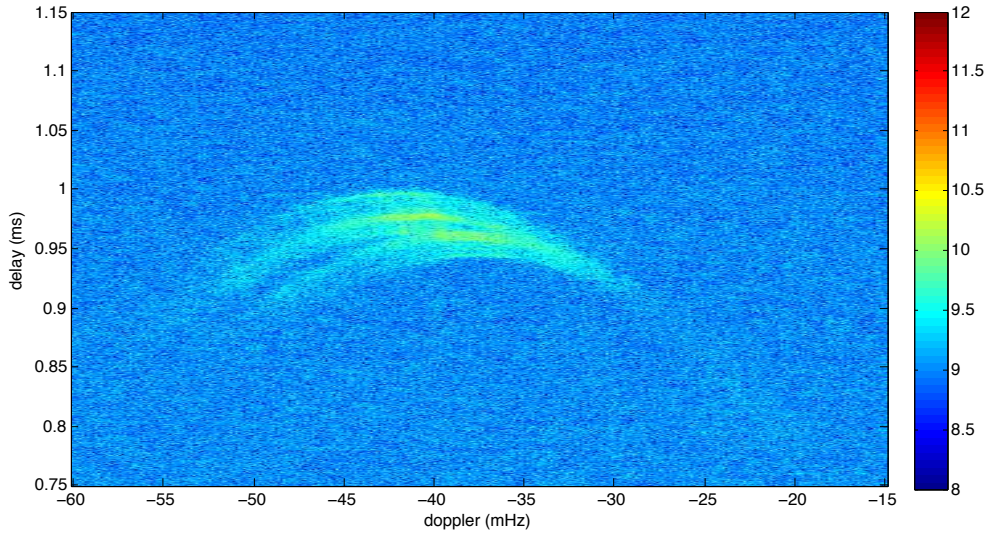

Figure 5.22: Offset feature at 338.5MHz, the intensity is in log_{10} scale

mainly moves the sub-arc horizontally, while $\theta_{\perp}$ fluctuation along offset feature mainly moves the sub-arc vertically. Because of the shape of reverse sub-arc, horizontal shift doesnt make dramatic change in residual, but vertical shift will leave a hole in the secondary spectrum (See Figure 5.23) and eventually makes mean squared residual discontinuous.

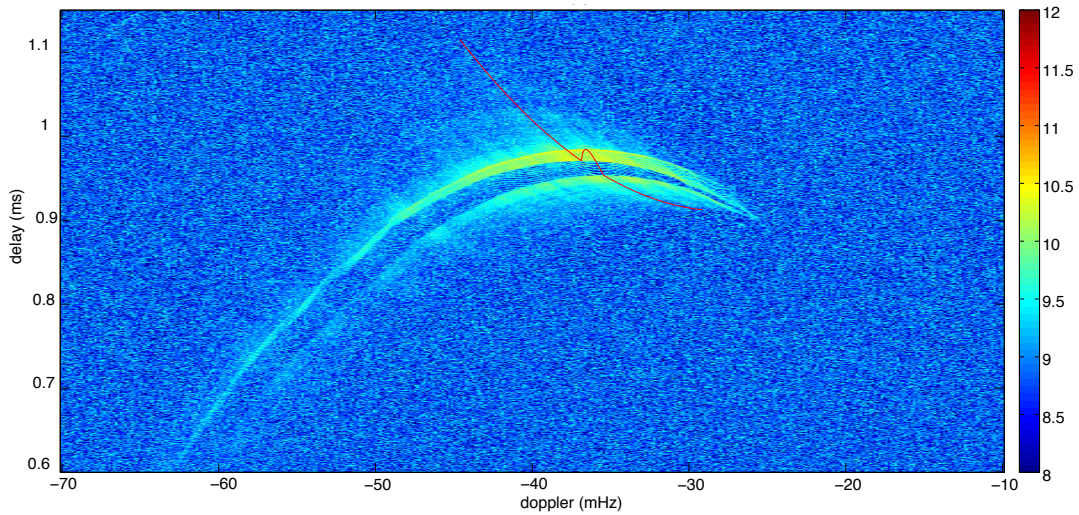

Figure 5.23: Simulated effect of $\theta_\perp$ fluctuation on secondary spectrum at $\tau = 1ms$, the intensity is in log_{10} scale

Clean algorithm is well used in interferometry [42]. Here we borrow this idea and change it to serve our purpose, and we call it cleaning method. The basic idea is straightforward. First simulate one single sub-arc layer, then cross-correlate with template data to find a few possible apexes, use some selection criteria to identify them as true or false apex, subtract the true sub-arcs from the data according to those apexes. Repeat those steps above on the remaining secondary spectrum to find more possible apexes until a certain number of times is reached or the remaining secondary spectra are all negative. The hardest parts of this method in our particular case are, how to find possible apexes, and the selection criteria. Once apexes are identified, we can easily convert them to $\theta_\perp$ given offset feature's parallel axis.

Detailed Steps of Cleaning Method:

1. Generate a single sub-arc, and use it as a standard layer. Left panel of Figure 5.24 shows an example of sub-arc layer.

2. Find sub-arc template to calculate cross-correlation between this template and entire secondary spectrum to locate a few possible sub-arc apexes (we choose the first five positions with highest cross-correlation). We only choose center part of the sub-arc as template (see right panel of Figure 5.24). If the

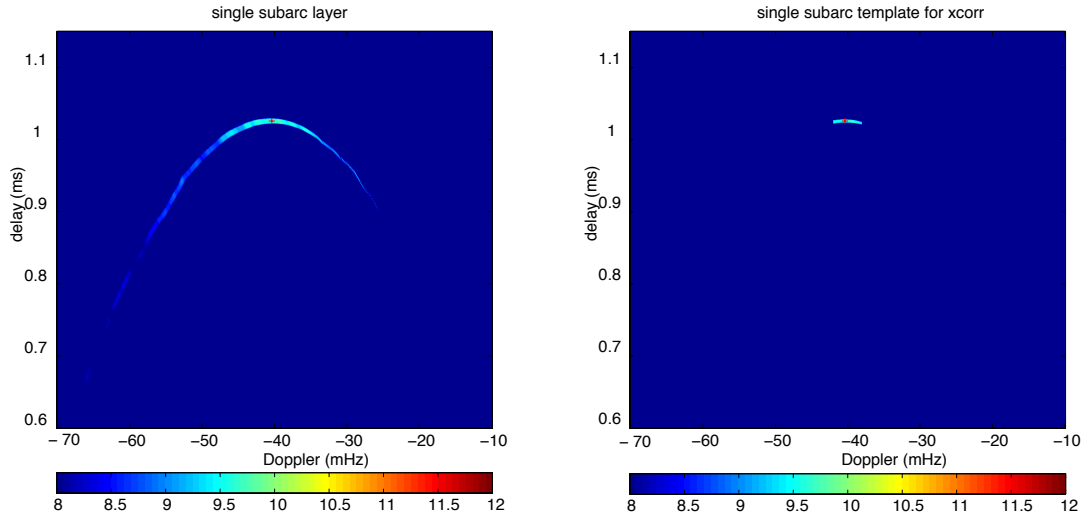

Figure 5.24: Standard sub-arc layer (left) and its sub-arc template for cross-correlation (right), y-axis is delay [0.6ms 1.15ms] and x-axis is doppler [-70mHz -10mHz], the intensity is in log_{10} scale

selected sub-arc region is too far out, then cross-correlation can't find the right apexes. Left panel of Figure 5.25 shows the cross-correlation using full sub-arc, peaks for different delay positions are not on the red line, which is the apex positions according to the input $\theta_{\perp}$. Right panel of Figure 5.25 shows the cross-correlation using sub-arc template in Figure 5.24 (right), and the peaks are now on the red line. The reason is that, when the chosen sub-arc region is too further out, then when we move the template along Doppler direction, the template sub-arcs arm will touch other sub-arcs below it which gives spurious correlation.

3. Judge if those five possible apexes as true or false apexes, by checking corresponding sub-arcs with those apexes in the remaining secondary spectrum (we just call them evaluated sub-arcs) and compare them with the standard sub-arc layer shown in the left panel of Figure 5.24. Two criteria are used:

   (a) Check how many zero/negative pixels in those evaluated sub-arcs. If the zero/negative pixels ratio is above some threshold (we usually choose 10%-20%), then treat this apex as a bad guess, and put it into a black-list.

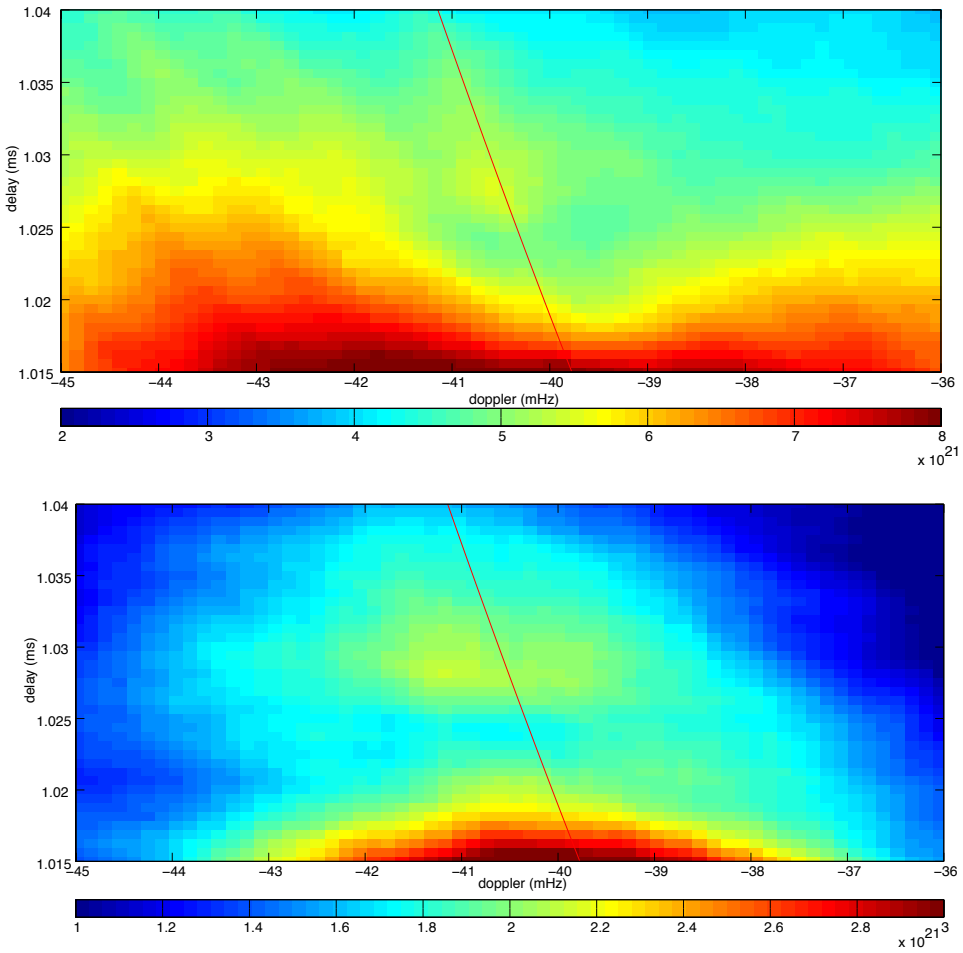

Figure 5.25: Cross-correlation using full sub-arc as template (upper) and partial sub-arc (down), y-axis is delay [1.015ms 1.04ms] and x-axis is doppler [-45mHz -36mHz], the intensity is in log_{10}

(b) Estimate 1-D core image's brightness using sub-arcs (let's call it ' sub-arc core brightness') and calculating their cross-correlation coefficients with the previously-estimated 1-D core image brightness. Each sub-arc can be treated as the interference between the core of primary feature and one offset point in offset feature, like what is discussed in Chapter 3. In this case, we assume both primary feature and offset feature are linear, so evaluated sub-arcs are thin in delay and averaging it over delay plus Jacobian could give us an good estimate of the primary feature's core 1-D brightness.

Simulation is done to test the method. We first simulate reversed sub-arc using the estimated 1-D core image of primary feature, which is shown in Figure 5.26 as red points. Then we apply the method above to the sub-arc, multiply a constant, and plot the estimated sub-arc core brightness in the same figure as black curve. They match pretty well. We also test it on observation data. Blue curve in Figure 5.26 comes from the identified sub-arc in channel 1 (Figure 5.19), and background is carefully removed before estimating core image from sub-arc. We can tell that the estimated core image from real observation is highly correlated with black curve and red points. There is a little gap at $3.7mas$ in blue curve, which is due to the fact that when we choose the sub-arc, we use a threshold to exclude the noise, SNR is low at that region.

The cross-correlation between them shows the similarity between standard sub-arc and evaluated sub-arcs better than 2-d cross-correlation we did earlier, because it can be easily normalized to get coefficient and use this number to exclude bad apexes. If the correlation coefficient is lower than a threshold (we usually choose 80% - 90%), then treat this apex as a bad guess, and put it into the blacklist as well.

4. Shift the standard sub-arc layer to those possible apexes positions we get in step 2, and subtract the normalized shifted sub-arc from the secondary spectrum, with normalization factor c. The reason we subtract also bad apexes, is because if all possible apexes are identified as bad guess in this iteration, and if we don't do that subtraction, then 2D cross-correlation in the next iteration will locate the same possible apex positions.

5. Repeat step 2) to 4) N times.

6. Add all sub-arc layer back from the blacklist.

7. Clean again on the remaining secondary spectrum, with different c, N, and template.

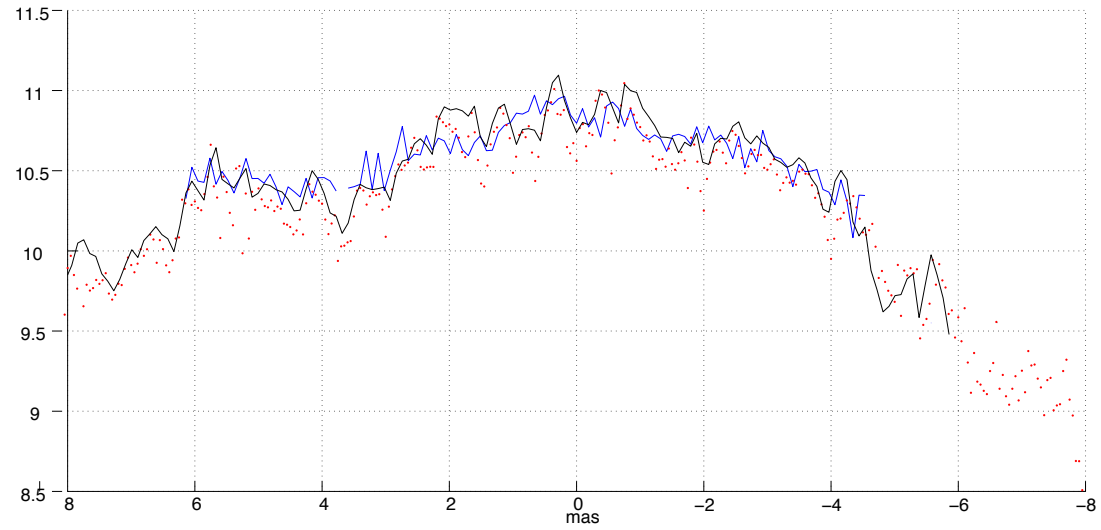

Figure 5.26: 1-D core brightness of previous fitting result and of estimating from sub-arc, y-axis is $\log_{10}(B)$, x-axis is $\theta_{\|}$, red dot is 1-D core image estimated from primary feature in previous chapter, black curve is 1-D core image estimated from simulated reversed sub-arcs of 1ms offset feature, the blue curve is 1-D core image estimated from observed reversed sub-arcs of 1ms offset feature,

5.5.3 Simulation of cleaning method and gradient method

Simulation is done to test if our cleaning method can find the right apexes. Figure 5.27 shows the input and recovered $\theta_{\perp}$ using cleaning method. The black curve is the input $\theta_{\perp}$, the red points are the recovered $\theta_{\perp}$, and green points are the linear interpolation of red points. Figure 5.23 shows the the secondary spectrum using the input $\theta_{\perp}$. Its recovered very well, except that there is a gap in red dots between -6 and -5.5 *mas* in Figure 5.27 where no valid apex is found over there. Thats due to the hole in the secondary spectrum. $\theta_{\perp}$ is not perfectly recovered, but matches the shape of the input very well.

Cleaning method can find a reasonably recovered $\theta_{\perp}$ for offset linear feature, but it has a hard time recovering the brightness. Since evaluated function $F(\mathbf{x})$ is still a continuous function of brightness for offset feature, gradient method works perfectly for only recovering offset features brightness, based on the recovered $\theta_{\perp}$ from previous cleaning method result.

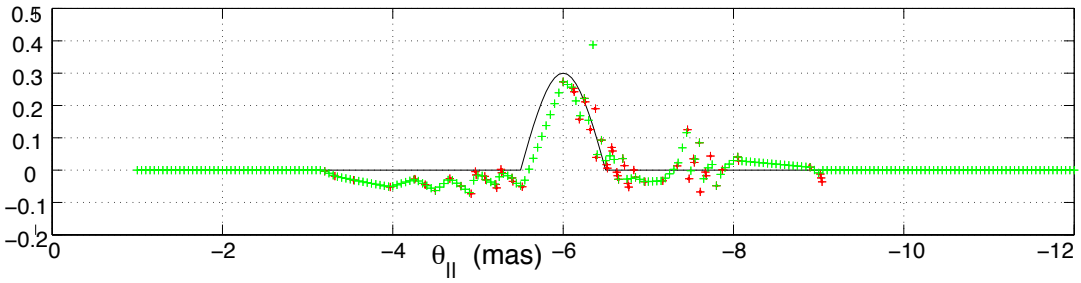

Figure 5.27: input (black curve) and recovered (red dots) $\theta_\perp$ using cleaning method, green dots are the interpolation of recovered $\theta_\perp$

The fitting result is very promising. Figure 5.28 shows the recovered brightness and $\theta_\perp$ and Figure 5.29 zooms in the brightness in the center part. Red points are the fitted brightness and black points are the input brightness. Most red points are on the top of the black points implying that the combination of cleaning method and gradient method works in recovering offset feature's $\theta_\perp$ and brightness.

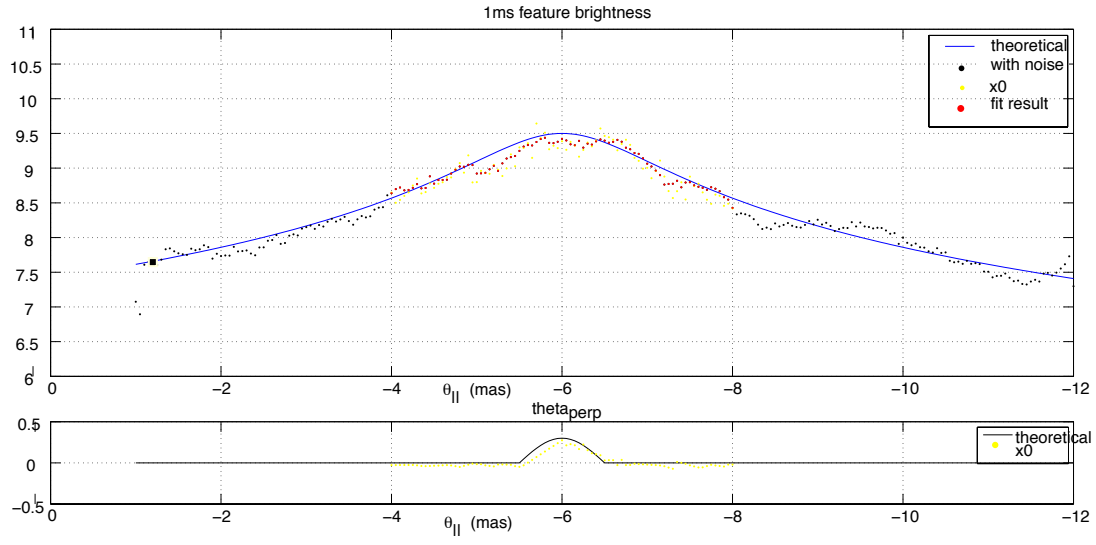

Figure 5.28: input and recovered brightness (upper panel) and $\theta_\perp$ (lower panel) using gradient method.

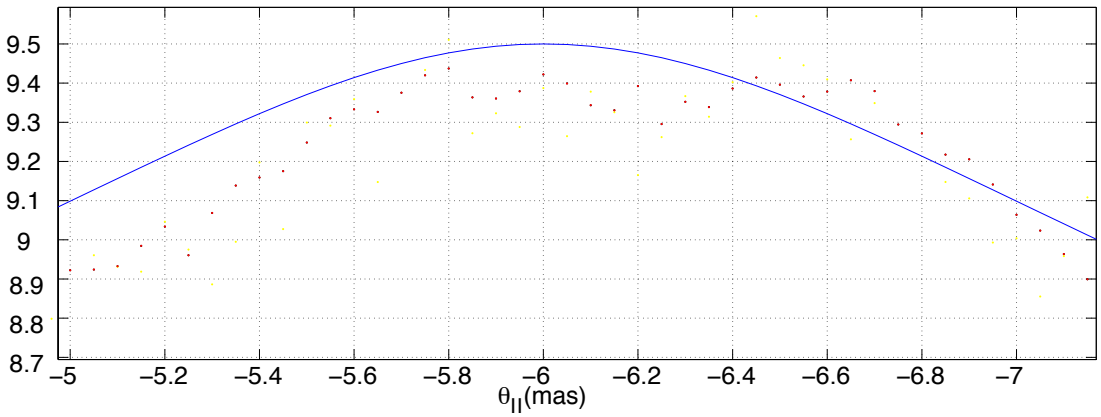

Figure 5.29: zoom in version of Figure 5.28

5.5.4 Apply cleaning method to observation data and two linear offset feature model

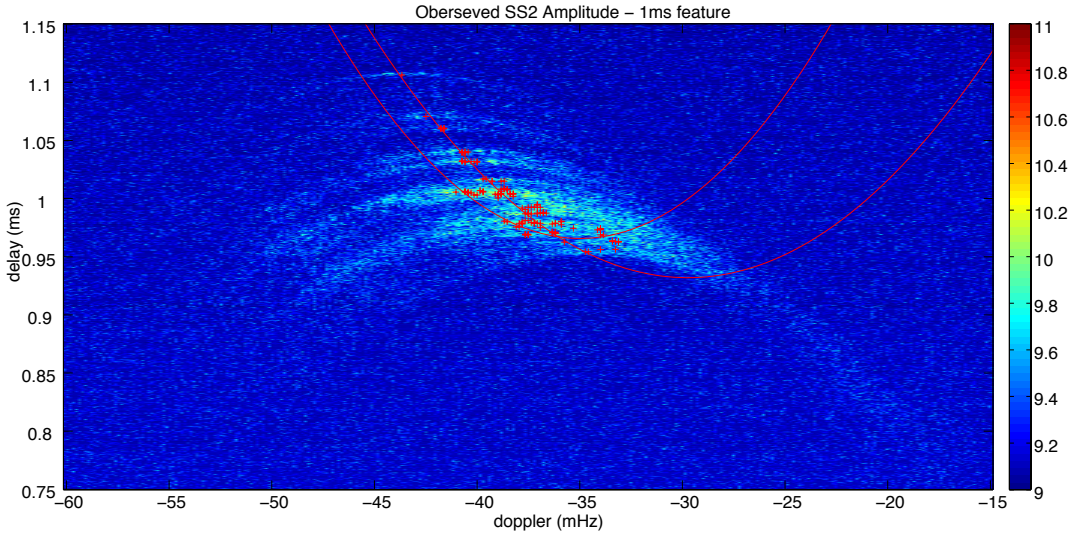

Figure 5.30: Identified apexes in offset feature (channel 1, 314.5MHz) using cleaning method in secondary spectrum, the intensity is in log10 scale, red dots are identified apexes and red curves corresponds to the two straight lines in the angular domain shown in Figure5.31

Now with observed data, Figure 5.30 shows the identified apexes in channel 1 using cleaning method and Figure 5.31 shows those apexes in RA-Dec coordinate. According to those identified apexes, its clear that one linear offset model is not ac-

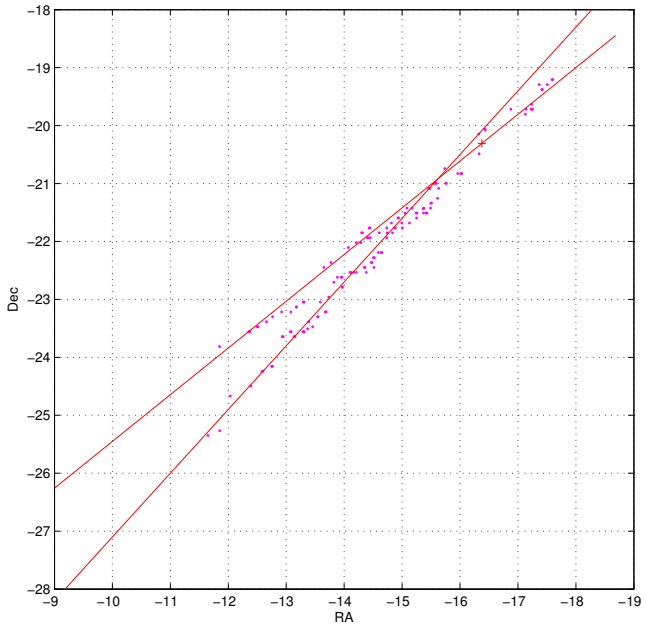

Figure 5.31: Identified apexes in offset feature using cleaning method in angular domain

curate and that a two linear feature model might fit this observation much better. The two straight red lines in Figure 5.31 help us to visualize the separation of those two groups of apexes and in Figure 5.30 we convert them into two forward parabolic arcs in red. Let's name the linear feature with bigger slope as offset linear feature 1 and the other as offset linear feature 2. At $(RA = -15.5\ mas, Dec = -21\ mas)$, linear feature 1 and 2 merge and it's hard to tell which linear group those apexes belong to. To make the model simple, we assume that linear feature 2 starts around $(RA = -12\ mas, Dec = -24\ mas)$ and ends right before the crossing, and all other apexes belong to linear feature 1.

Is that possible that the gap between those two linear offset features is actually filled in? In another word, is it possible that this is one thick feature with width instead of two? It's not possible. if it was, then there shouldnt be any gap between those two forward red parabolic arcs.

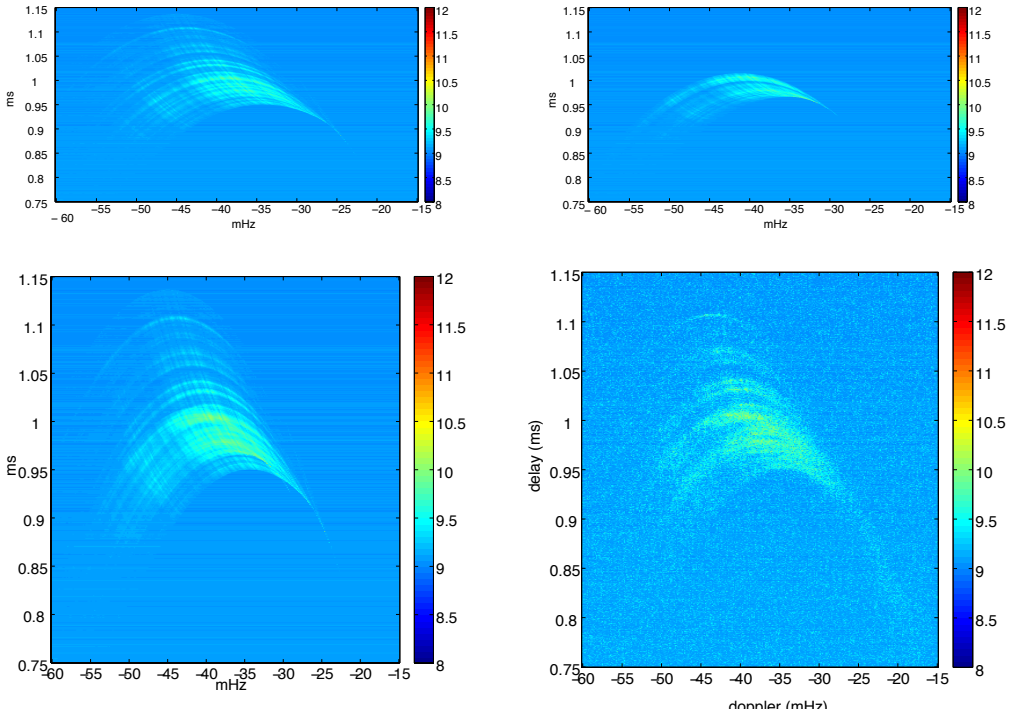

Figure 5.32: Modeled and observed two linear offset feature at 314.5MHz. *upper-left:* modeled linear feature 1, *upper-right:* modeled linear feature 2, *lower-left:* both modeled linear features added together, *lower-right:* observed offset linear feature

Its a very interesting result. We never think it this way until the cleaning method provides more accurate apexes positions. What would the secondary spectrum look like if we the brightness model in the angular domain is two straight line? Based on this two straight-line model, we simulate the secondary spectrum using directly-sampled brightness along the two forward parabolic arcs in Figure 5.30. Figure 5.32 shows the modeled offset linear feature 1 and 2 in the upper two panels, linear feature 1 and 2 added together in the left-down panel and the observed linear offset feature in the right-down panel. Comparing to Figure 5.5 which uses one linear offset feature model, two linear feature model is much closer to the observation data.

5.5.5 Fit brightness based on 2 linear offset feature model

In order to make the fitting simple and efficient and in the same time keep the model accurate, from now on, we use two straight-line model for linear offset feature, while we still use one curvi-line model for primary feature.

We use directly- sampled brightness as initial guess, and we use both gradient method as discussed in section 5.4, and lsqnonlin fitting program provided in matlab which uses Levenberg-Marquardt (L-M) algorithm. Those two algorithms return very similar fitting results. Figure 5.33 shows fitted brightness using gradient method (marked in blue) and lsqnonlin (marked in red), for linear feature 1(upper panel) and linear feature 2(lower panel). zero $\theta_{\|}$ corresponds to the lowest delay of those two linear features. Vertical red line indicates the crossing of two linear feature, and we align those two linear feature according to the crossing. In both linear offset features, specially linear feature 1, both algorithms match very well. It implies that both gradient method and L-M method converge. It makes perfect sense that all LMS algorithms are supposed to converge to the same value, it's not dependent with what algorithm you use. In the rest of this section, all fitting results are from lsqnonlin.

Figure 5.34 shows the fitted brightness of linear feature 1 in the upper panel and linear feature 2 in the lower panel. Four channels are marked in blue (channel 1), red (channel 2), green (channel 3) and black (channel 4), respectively. Two linear features are aligned in the same way as Figure 5.33.

In linear offset feature 1, there is a peak at -11 mas, which doesn't show up in all other channels, that matches the phenomenon that that thin sub-arc at ~ 1.1 ms only appears in channel 1. It also clearly shows how those four sub-arcs merge into two from channel 2 to channel 3, at -8.5 mas and -9.5 mas, the red curve has two big peaks, each of them has a dent which forms two small peaks next to each other, and in green curve, those two small peaks become one, and in black curve, all of them disappear. At -7 mas, brightness in four channels drops with a different slope, the order from slowest to fastest is the same order of channel.

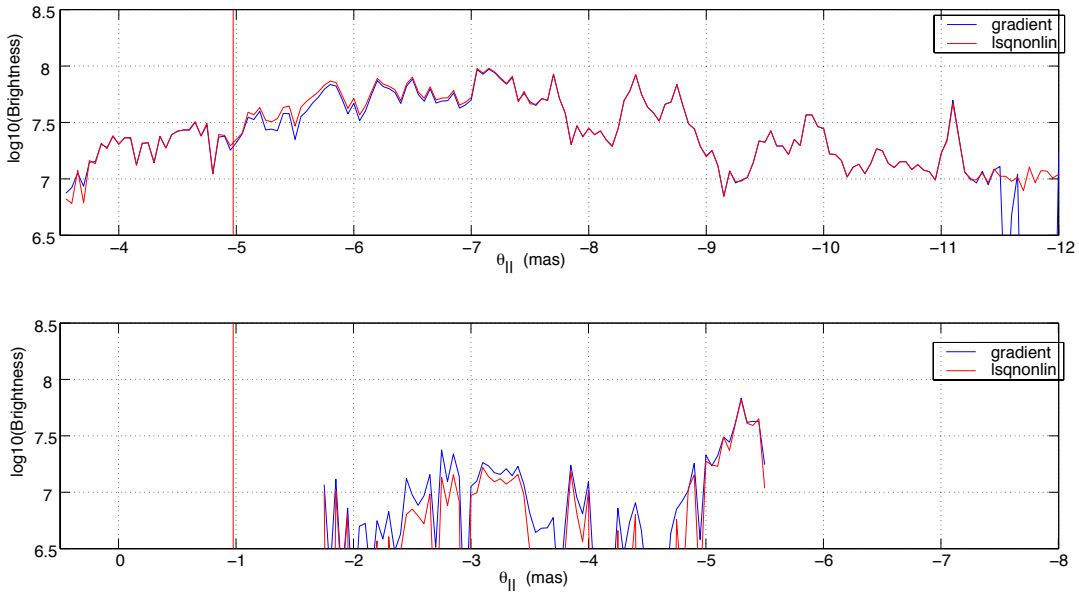

Figure 5.33: Fitted brightness of linear feature 1 (upper) and linear feature 2 (lower) using gradient method (blue) and L-M method (red), y-axis is $\log_{10}(B)$

In linear offset feature 2, brightness in general is weaker than linear feature 1. Because of lower SNR, the brightness looks more noisy. Green curve (channel 3) is obviously higher than all other channels between -4 to -3 mas, which matches the phenomenon that in channel 3 there is a strong thick sub-arc at $1ms$.

Figure 5.35 to Figure 5.38 show observed secondary spectrum (left) and modeled secondary spectrum (right) from channel 1 to 4, based on the fitted brightness shown in Figure 5.34. All of those models match the observation, implying that this two linear offset model is a simple and accurate model.

Except that there is some weak signal on the right tail of the reversed sub-arcs in the observation data, but it's not there in our models. For example, in Figure 5.37, there is some signal at (-22mHz, 0.8ms) in the left panel, which is not shown in the model in the right panel. That position corresponds to the interference of the 1ms offset feature and the bright primary feature at -10mas. The reason that it's not shown in the model is that, based on the 1-D brightness

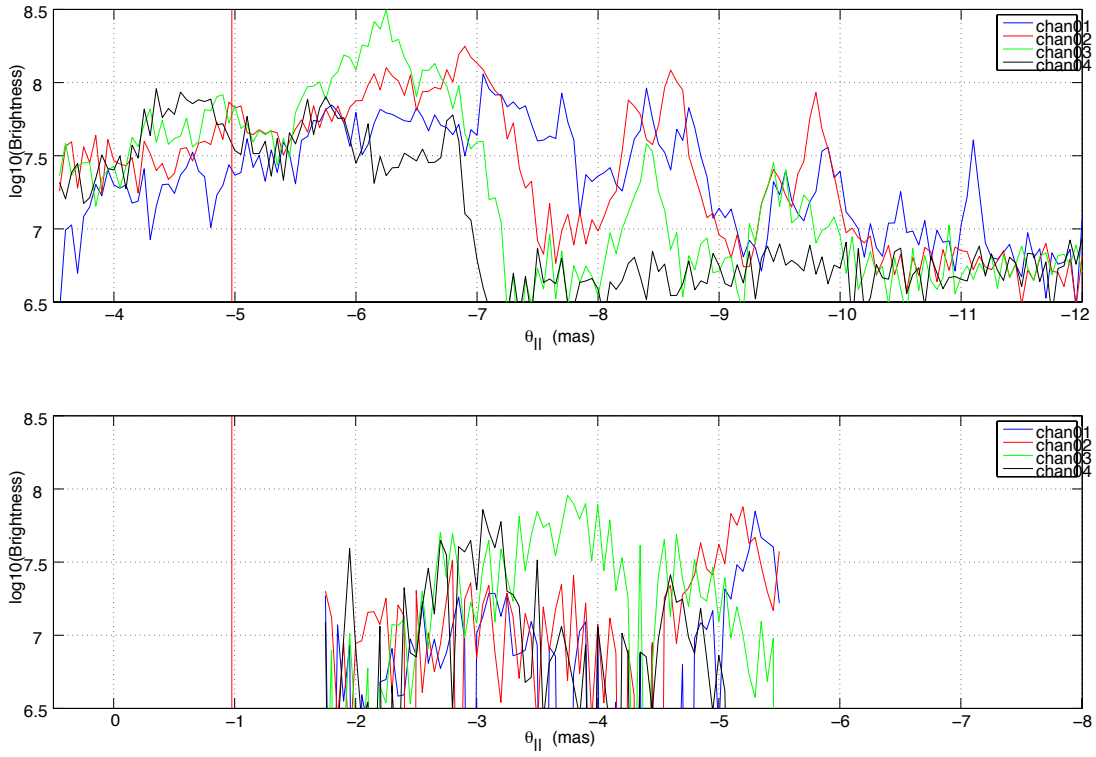

Figure 5.34: Fitted brightness of linear feature 1 (upper) and linear feature 2 (lower), in all four channels, y-axis is $\log_{10}(B)$

image model, all those simulated reversed sub-arcs's width gets smaller and smaller when from its left tail to its right tail, due to Jacobian. When it reaches to the most right end, it becomes a broken line and eventually disappears . But in real observation, the brightness image has small width which will make it possible to see the interference of the 1ms feature and the bright primary feature at -10mas.

5.6 Conclusion

In this chapter, we take extreme case to make it a 1-dimensional model. Both straight-line and curve-line models are studied.

Straight-line linear model has unique position mapping between secondary spectrum and angular spectrum, backward method can be used to re-construct the

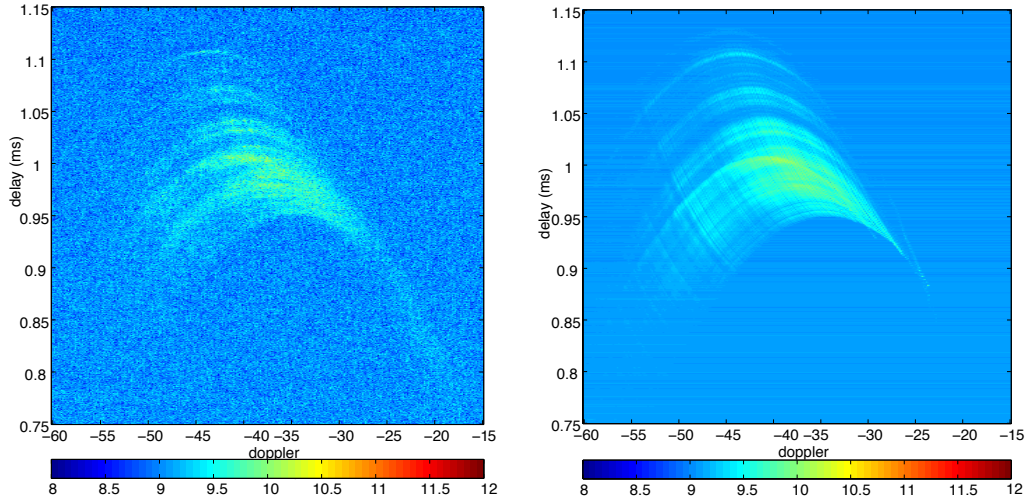

Figure 5.35: Observed and modeled two linear offset feature in channel 1. *upper-left:* observed offset linear feature, *upper-right:* modeled offset linear feature with fitted brightness and two linear features.

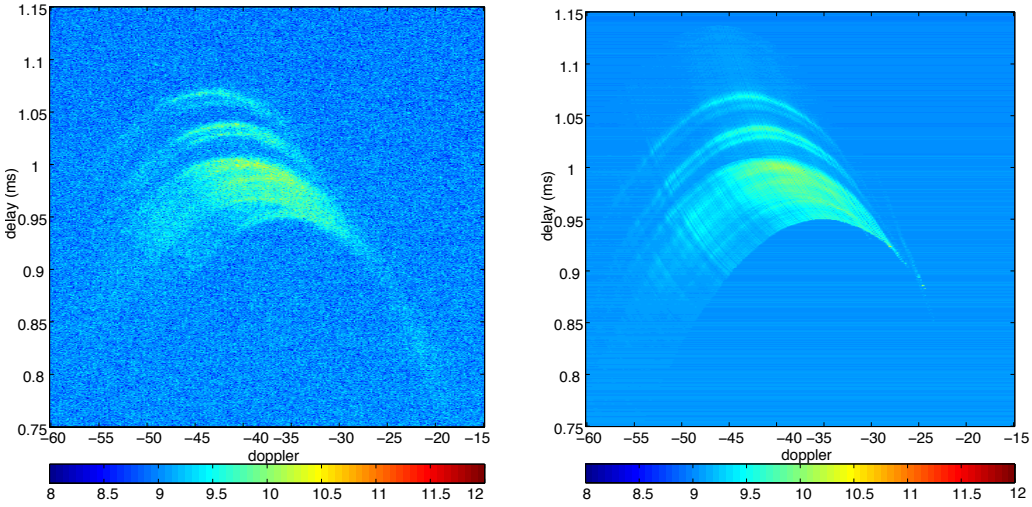

Figure 5.36: The same as Figure 5.35, but in channel 2

straight-line linear brightness distribution. However, straight-line can not explain the phenomenon that the apexes of some reverse sub-arc are shifted away from the main forward parabolic arc.

Curvi-line linear model is more close to our observation, however, it has ambiguity when we try to find the angular position from secondary spectrum so

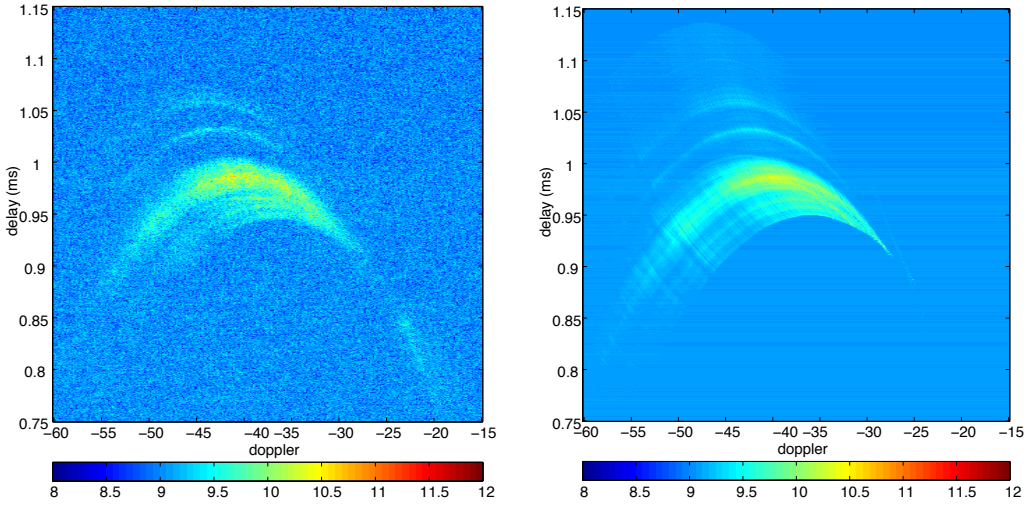

Figure 5.37: The same as Figure 5.35, but in channel 3

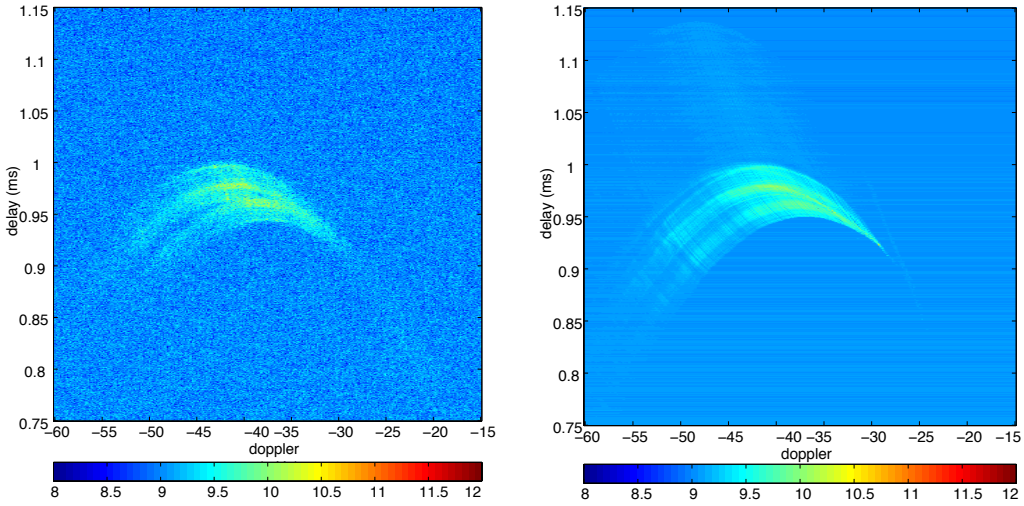

Figure 5.38: The same as Figure 5.35, but in channel 4

backward method can't be used. In order to solve this, an approximation method is developed to realize the position mapping and brightness reconstruction. We use curvi-line linear model on primary feature, and use gradient method to fit both $B(\theta_{\|})$ and $\theta_{\perp}(\theta_{\|})$. We apply this method to observation data after simulation is verified, and find a good estimate of the primary feature's brightness distribution along $\theta_{\|}$ with $\theta_{\perp}$ fluctuation.

It's hard to apply the same technique to the 1ms offset feature, because curvi-line linear model for offset feature makes the evaluated function $F(x)$ discontinuous, due to the geometric difference between primary feature and offset feature. We invented a new cleaning method to estimate the $\theta_\perp$ fluctuation, and found out that offset feature is better modeled as two straight-lines, and we fit the $B(\theta_\parallel)$ along both straight-lines. Offset feature is quite different in different channel, so all brightness is fitted in all four channels.

Chapter 6

Conclusion and physical explanation of the scattered image of pulsar B0834+06

6.1 Comparing the various models from previous chapters

In each chapter we have different models and techniques, and different estimation of the scattered image based on those models and techniques.

In chapter 2, we used identified apexes position and phase information of the secondary cross spectrum, to find the scattering positions of the screen, in both in primary feature and offset feature regions. We also estimated the effective velocity and the effective distance. We developed a good basic understanding of the primary and offset feature. However, we did not estimate brightness on those positions and we could not resolve points from the central core of the scattered image. Figure 2.2 shows the astrometry image of the screen.

In chapter 3, we use reversed sub-arc to re-construct the 2-D core scattering image which is shown in Figure 3.9. The core image has an axial ratio of ~ 3 and

is tilted in the same direction as chapter 2. The brightness integrated over perpendicular direction matches the 1-D $B_{\parallel}(\theta_{\parallel})$ estimated in chapter 2. The brightness integrated over parallel direction which gives the estimate of $B_{\perp}(\theta_{\perp})$ shows more homogenous distribution.

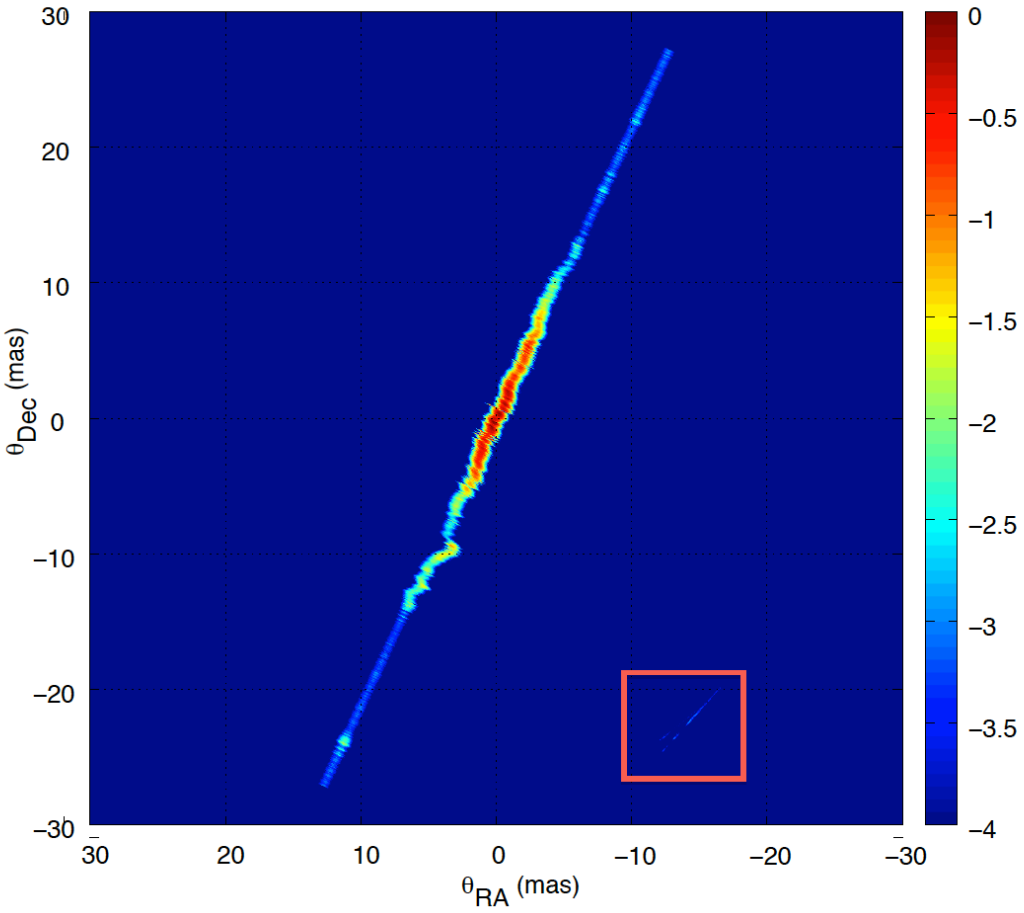

Figure 6.1: Estimated 1-D brightness distribution including both primary and offset feature, with dynamic range between -4 to 0. The offset feature in the red square is expanded in Figure 6.2 below.

In chapter 4, we analyzed a different data set, but of the same pulsar. We developed an imaging technique based on the electric field representation, which has a two-fold ambiguity. As in Figure 4.5 it shows the same parallel direction as in chapter 2 and 3. However, due to the lack of phase information, the position

ambiguity can't be solved, especially in the core image. We noticed four features in Figure 4.5, one of which (RA=-5mas, Dec=8mas) is far off the main parallel axis of the primary feature which was not seen in the results of those two previous chapters.

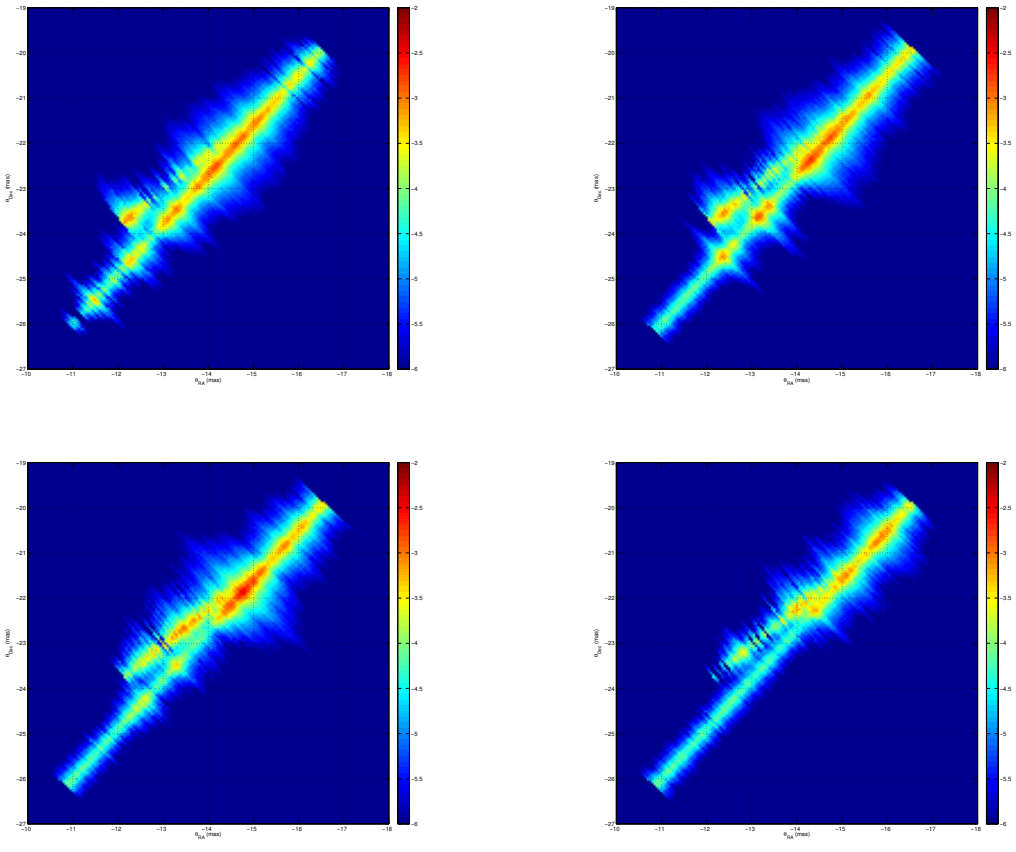

Figure 6.2: The same as Figure 6.1, zoom in offset feature region, with dynamic range between -6 to 2, four different channels. *upper-left:* Channel 1, *upper-right:* Channel 2, *lower-left:* Channel 3, *lower-right:* Channel 4

In chapter 5, curvi-line linear feature model is used on primary feature, and two straight-line linear model is used on offset feature. Figure 5.15 and Figure 5.34 show the brightness distribution and $\theta_\perp$ fluctuation for primary feature and offset feature. Figure 5.18 and Figure 5.31 show the geometry of primary feature and offset feature. It's hard to combine them to give a good picture of their bright-

ness image because the linear model has no width. In order to make it easy to present brightness for linear model, we extended the fitted model in the perpendicular direction using kolmogorov model, with a very small width. Figure 6.1 shows the fitted curvi-line brightness image. There is one significant $\theta_\perp$ fluctuation at (RA=3mas, Dec=-10mas). The offset feature is in the lower-right corner, but in this dynamic range ([-4 0]) is too weak to see. Figure 6.2 zooms in and display the two-linear offset feature model in a different dynamic range([-6 -2]) in four different channels so the brightness variation can be seen. 1-D brightness model is quite accurate if the actual brightness is essentially linear, and it can estimate the brightness further away from the origin, instead of only estimating the core image like in chapter 3. It reveals the fluctuation, and we found a good model for offset feature as well.

Since chapter 4 is from a different dataset, we can't compare them directly, but we can compare the core image from chapter 3 and extended core image from chapter 5. From chapter 3 we learned that the core brightness distribution along primary feature's parallel axis shows inhomogeneity while its distribution along the perpendicular axis is more homogeneous. In order to include both, we model the core image as a 2-D kolmogorov function modulated with a function of $\theta_\parallel$ to present the in-homogenous variation along the parallel axis.

$$B_2(\theta_\parallel, \theta_\perp) = \frac{F_1(\theta_\parallel)}{[1 + (\frac{\theta_\parallel}{\theta_{\parallel p}})^2 + (\frac{\theta_\perp}{\theta_{\perp p}})^2]^{11/6}} \tag{6.1}$$

From Chapter 3, $\theta_{\parallel p} = 3.85mas$ and $\theta_{\perp p} = 1.3mas$. $F_1(\theta_\parallel)$ can be derived by integrating $B_2(\theta_\parallel, \theta_\perp)$ over $\theta_\perp$ and equate it to 1-d brightness brightness distribution $B(\theta_\parallel)$ in Chapter 5.

$$B_2(\theta_\parallel, \theta_\perp) = \frac{B(\theta_\parallel)[1 + (\frac{\theta_\parallel}{\theta_{\parallel p}})^2]^{8/6}}{C_0[1 + (\frac{\theta_\parallel}{\theta_{\parallel p}})^2 + (\frac{\theta_\perp}{\theta_{\perp p}})^2]^{11/6}} \tag{6.2}$$

Where $C_0 = \theta_{\perp 0}\sqrt{\pi}\Gamma(4/3)/\Gamma(11/6)$ is a constant. In Figure 6.3, the left pane is re-print of the 2-D core brightness image from chapter 3, and the right panel is 2-D extended core image from the curve-line 1-D brightness in chapter 5. They

exhibit very similar patterns.

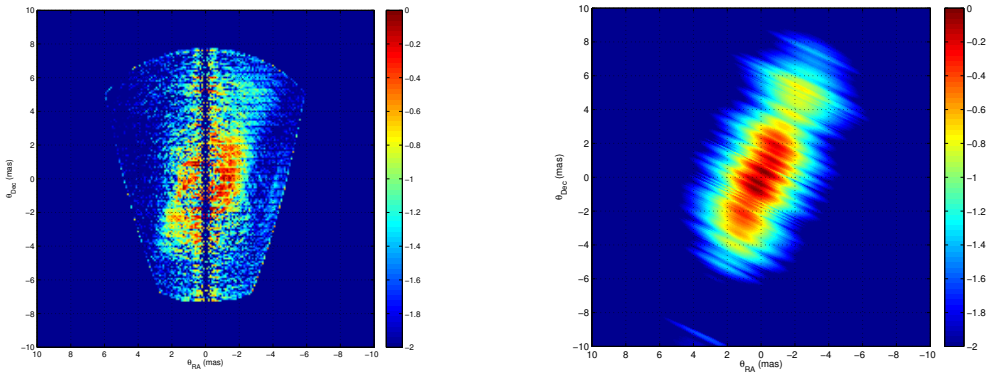

Figure 6.3: Observed and modeled two linear offset feature in channel 1. *upper-left:* observed offset linear feature, *upper-right:* modeled offset linear feature with fitted brightness and two linear features.

Since the 2-D core brightness image has width, Figure 6.1 can not be accurate. Unfortunately we don't have knowledge about the perpendicular width outside of the core image. Here we assume that outer part of the primary feature has the same characteristic width as the core image and extend Figure 6.1 using Equation 6.2 and it's plotted in Figure 6.4. This 2-D brightness distribution explains the 2-D core image better, and it also explains the anisotropic property of the brightness, the in-homogeneity of the brightness distribution along primary features parallel axis, and the perpendicular variation. It seems that among all the model we obtained in this thesis, this extended 2-D core brightness image fits our observation the best. This is similar to the scattered image estimated by Trang and Rickett [49] for the pulsar B1133+16.

6.2 Summary of the properties of reconstructed brightness image

Here is a summary of the properties that we have learned from all those reconstructed brightness images.

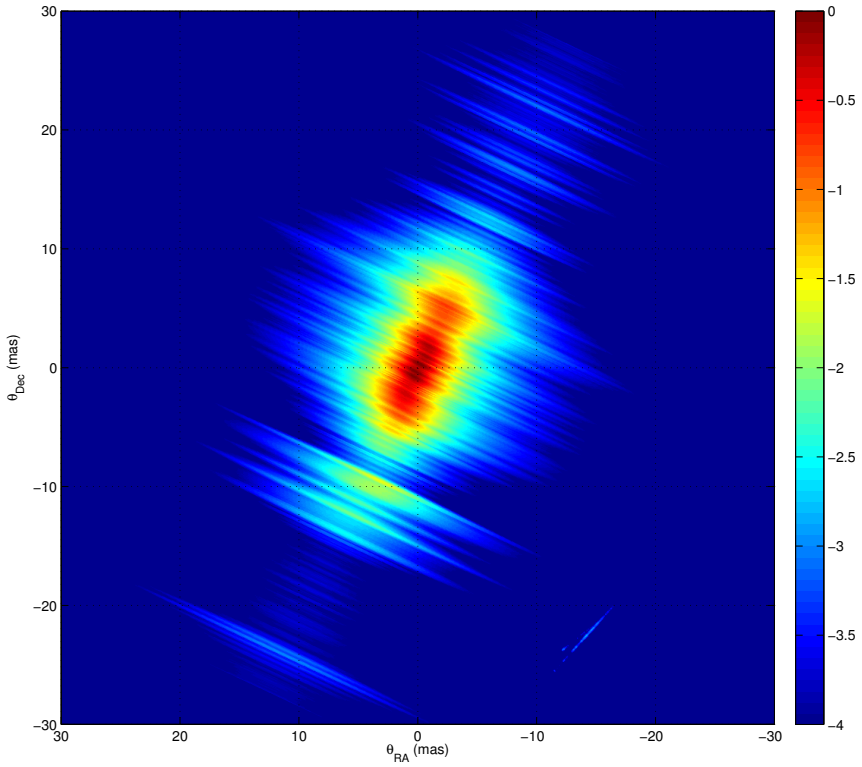

Figure 6.4: Estimated 2-D brightness distribution including both primary and offset feature

1. Two separate features

   There are two separate features, one is primary feature which goes through the center, the other is an offset feature which is located around ($RA = -15mas$, $Dec = -22mas$). Offset feature's brightness strength is ∼100 times weaker than primary feature, as you can see in Figure 6.1 and Figure 6.4.

2. Anisotropic

   All brightness images are very anistropic. Primary and offset features are both elongated, at different angles (The angle between those two features and velocity is $\alpha_1 = 25.4^o$ and $\alpha_2 = 51.3^o$ respectively). While 3:1 is only moderately anisotropic estimated at half of the peak brightness, the effective axial ratio at, say, 0.01 of the peak might be higher, making an extremely

anisotropic image, which must be explained in terms of the underlying plasma turbulence.

3. Inhomogeneous

   The brightness distribution along primary feature's parallel axis shows inhomogeneity. No common model, such as kolmogorov, can be used to describe this distribution. There are a few very narrow peaks, such as (RA=3 mas, Dec=-10 mas) and (RA=-6mas, Dec=12.5 mas).

4. Homogeneous

   The brightness distribution along primary feature's perpendicular axis, as shown in Figure 3.11, follows the homogenous kolmogorov model with $\theta_p = 1.3mas$ quite well.

5. curvi-linear model

   There is fluctuation in $\theta_\perp$ along the primary feature's parallel axis. The small fluctuation can be seen in 2-D brightness figures, such as the right panel of Figure 6.3. We noticed in particular the large displacement at (RA=3 mas, Dec=-10 mas) which is a peak in brightness as well.

6. Frequency dependence

   While the primary feature's brightness image is independent with frequency, the details of the offset feature's brightness vary with frequency. For example, Figure 5.34 shows the systematic shift with frequency. That might be due to the the fact that refractive index is dependent with frequency and offset feature's displacement from the origin is due to refraction rather than diffraction.

$$n = \sqrt{1 - \frac{w_p^2}{w^2}} \tag{6.3}$$

6.3 Plasma turbulence

What is the physical plasma turbulence behind the scattered brightness image? What is the relationship between them?

Scattered brightness image is what the pulsar looks like after its electromagnetic waves travel through the interstellar plasma. Scattered brightness distribution doesn't necessarily represent the same distribution of the interstellar plasma, but they are related.

In order to explain the anisotropic image, there are two possible models for the plasma distributions. We call them parallel [11] and orthogonal geometry models.

1. In parallel geometry model, there is one big anisotropic filament aligned along the main scattering axis, its shape is controlled the magnetic field whose direction is the same as the main scattering axis. There are very compact, denser 'knots' which are responsible for the discrete locations of the subarcs, and those 'knots' are due to isotropic turbulence substructure, which are distributed along the filament. Since the scattering is isotropic, the potentially visible region on the screen would be circular with its angular size determined by the scattered angle of the turbulence. However, the perpendicular width is restricted by the width of the filament. The offset feature in this model has the similar turbulence structure as the primary feature. It's caused by a separate big filament along its own scattering axis with denser 'knots' on it, and it's in the visible region so we can still see it. Figure 6.5 illustrates this parallel geometry model.

   Advantage of the parallel model:

   (a) Easy to explain offset feature, it has the same scattering type as the primary feature.

   (b) The offset feature is in the circular region if we choose the radius as the distance between origin and furthest point of the primary feature.

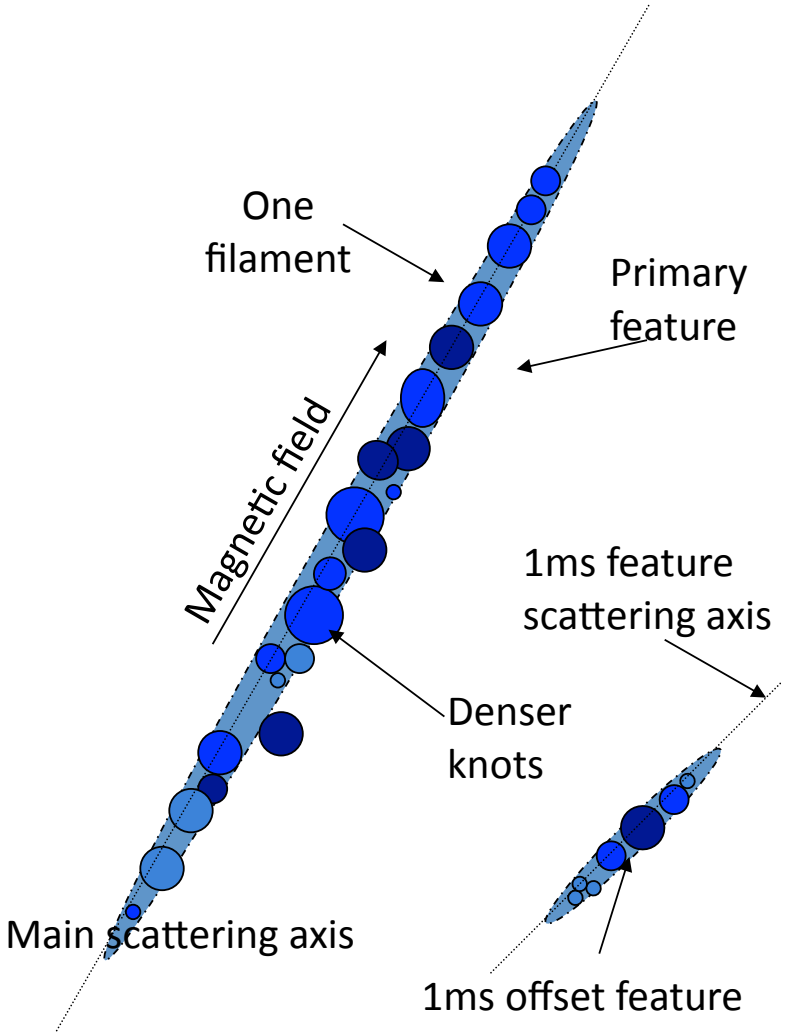

Figure 6.5: parallel geometry model

(c) Easy to explain the in-homogeneity, just due to the plasma turbulence density of each clump along the line.

(d) Easy to explain the displaced blob in the brightness image with big $\theta_{\perp}$, such as the one at (RA=3mas, Dec=-10mas)

Dis-advantage the parallel model:

(a) While it is not clear how accurately the pulsar must be aligned behind the filament, it seems an unlikely and special configuration.

(b) Hard to explain the similarity of two data sets. The data set in chapter 4 looks similar with the other data set and they are 22 months apart, It seems unlikely that the pulsar lies behind the center of the primary feature at both times is even rarer.

(c) It's rare that all the 'knots' are in a line, both primary feature and offset feature.

(d) It's hard to explain that the estimated axial ratio of the core image is $\sim$3 and the 2-D core image is smooth, unless a few 'knots' are carefully overlapped with each other, otherwise the axial ratio has to be 1.
item In [21], they observed the same pulsar in Jan of 2005 at the same frequency over a period of 26 days. In their result the center of the forward primary arc stays at the origin. If this was parallel model, and the velocity direction is very close to the positive Dec axis, then it wouldn't stay at the origin.

2. In orthogonal geometry model, the primary feature is due to anisotropic plasma turbulence elongated along the magnetic field which is orthogonal to the direction of the primary scattering axis. Then the scattered brightness is elongated along that axis. If the density and variance of the turbulence vary along that axis, there will be in-homogeneity in the 1-D brightness. Since it's anisotropic, the visible region on the screen is not circular, with large maximum scattering angle θ_{s2} in the parallel direction and small maximum scattering angle θ_{s1} in the orthogonal direction. The perpendicular width of brightness image is due to θ_{s1}. The offset feature might be due to the similar filament-shaped plasma turbulence as the primary feature in the same screen, but in this area the column density of electrons has gradient. This electron column density gradient work as a prism, pulsar's plane wave is refracted through the 'prism' and bent to the direction of the earth. Figure 6.6 shows the orthogonal geometry model with 1ms offset feature model 1, the prism is illustrated as a green triangle in this figure.

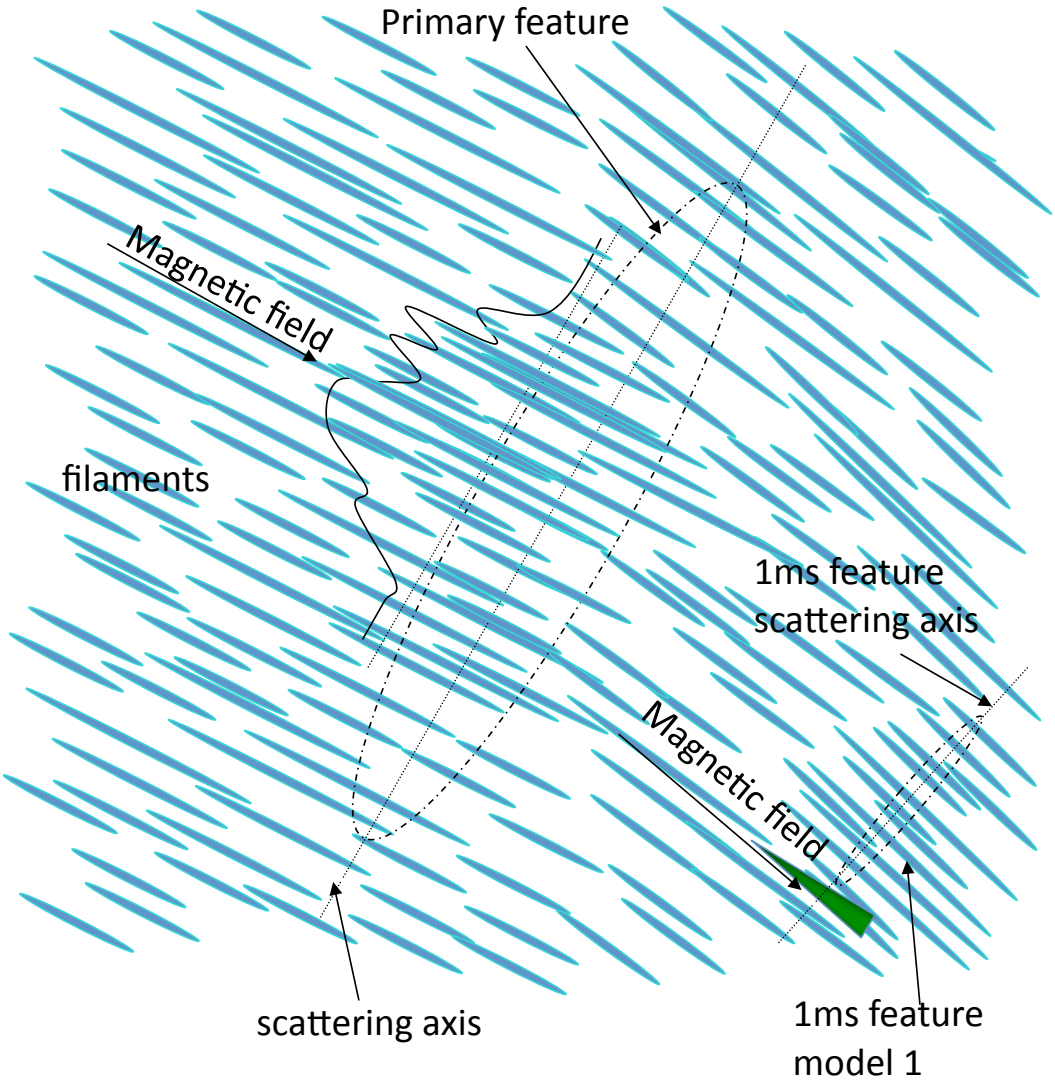

Figure 6.6: orthogonal geometry model 1

Advantage of the orthogonal model:

(a) Easy to explain pulsar position. Its not necessary that the pulsar has to be right behind the center of the primary feature.

(b) Easy to explain the similarity of the two data sets.

(c) Prism-shaped column density of plasma in 1ms offset model causes frequency dependent refraction to explain why the offset feature is frequency dependent.

(d) It doesn't require special plasma structure as a few 'knots' in a line.

(e) Easy to explain the reconstructed 2-D core image with axial ratio of 3.

Dis-advantage of the orthogonal model:

(a) Unlike the parallel model in which 1ms offset feature is the same as primary feature, In orthogonal model, we have to add a prism shaped scattering screen to make it possible for us to observe 1ms offset feature.

(b) Hard to explain the displaced blob in the brightness image with big $\theta_\perp$ at (RA=3mas, Dec=-10mas).

6.3.1 Summary

In summary, we think the orthogonal model could fit our observation better than the parallel model. It has some distinct advantages over the parallel model, such as the pulsar doesn't need to be behind the center of the primary feature, or it's easy to explain the similarity of those two data sets. Although it still has some disadvantages, there are still supporting explanations. The prism shaped screen is necessary to explain why we can observe 1ms offset feature, it also helps explains the frequency dependence of the offset feature. It does makes it harder to explain the displaced blob in the brightness image with big $\theta_\perp$, but it could be due to a small prism or a displaced 'knot' which is introduced in parallel model.

6.4 Further work

Firstly, in Chapter 3, sections 3.1 and 3.2 present two different models (instantaneous and ensemble-averaging) and their theoretical relations for the secondary cross spectrum $C(f_D, \tau, \boldsymbol{b})$ in Equations 3.33 and 3.60. We found inconsistency in the Jacobians between those two models. This inconsistency goes back to the formulation of the visibility from the scattered image in Equation 3.6. Equation 3.6 is introduced without explicit justification and all the problems come from this point. We still haven't resolved this inconsistency mathematically, this will

be one of our our highest priorities to work on as further work.

Secondly, We still don't have enough knowledge about the width of the outer part of the primary feature. Figure 6.4 uses the assumption that outer part has the same characteristic width $\theta_{\perp p} = 1.3mas$ as the core brightness image. It is a good estimation. However, when we calculate the higher delay area (> 0.05 ms) of secondary spectrum based on this model using method in section 3.4.2, there is no clearly isolated reserved sub-arc, all reversed sub-arcs are smeared with each other. It is possible that that the characteristic width of the outer part is over-estimated, or this 2-D model based on a 2-D kolmogorov function modulated with a function of $\theta_{\parallel}$ is not accurate. An iterative method can be used to improve the scattered brightness image in Figure 6.4 by calculating the secondary spectrum from this brightness distribution and compare with the observed secondary spectrum.

Thirdly, interpretation of the scattered image in terms of the physical structure of the plasma would be much clearer if we could observe the same pulsar for multiple times continuously using the same resolution and frequency, maybe every few days, maybe every one week or two, then we might find out the continuous movement of the plasma structure, similar as discussed in [21]. In their result, there are four blobs in their secondary spectrum, and they moved toward the positive doppler along the main forward arc. With our image reconstruction technique, we will see those blobs moving in the angular domain with more brightness and position details, and it will also help us to determine the geometry model.

In the case of parallel geometry model, because the effective velocity direction basically points to the positive Dec axis, both the primary feature and the 1ms offset feature will move out of the picture slowly. Once the center of the primary feature moves away from the pulsar angular position, then the main forward parabolic arc in the secondary spectrum will be shifted and become more asymmetric. The 1ms feature in the secondary spectrum will move down a little

bit in a parabolic track and then move up again in the positive doppler side.

In the case of orthogonal geometry model, the main forward parabolic arc will stay, the individual reversed sub-arcs in the secondary spectrum will move along the main forward arc toward the positive doppler direction. The 1ms feature in the secondary spectrum will disappear if it's only in a small region, but other offset feature at different position with different prism angle might be able seen.

By observing the secondary spectrum using continuous observations will definitely help us determine the plasma turbulence type. Although we are more lean to the orthogonal model, but without the continuous observation, we can't be 100% sure.

Last but not least we plan to test the two geometries using the scintillation code developed by Coles et al. (1995) [50]. This tool simulates the electric field of a wave after propagation through a random phase changing screen (typically described by a homogeneous Kolmogorov spectrum). It includes the computation of a dynamic spectrum of intensity. It will be modified to include an inhomogeneous distribution of anisotropic turbulence and can simulate interferometric visibility. By comparing this calculated secondary spectrum with observation it will help us determine which plasma structural model fits our observation.

Bibliography

[1] Andrew G. Lyne, Francis Graham-Smith, 2006, Pulsar Astronomy, Cambridge University Press

[2] W. F. Brisken, J.-P. Macquart, J. J. Gao, B. J. Rickett, W. A. Coles, A. T. Deller, S. J. Tingay, C.J.West, 2010, ApJ, **708**, 232

[3] Armstrong, J. W., Rickett, B. J., & Spangler, S. R. 1995, ApJ, **443**, 209

[4] Bignall, H. E., Macquart, J.-P., Jauncey, D. L., Lovell, J. E. J., Tzioumis, A. K. & Kedziora-Chudczer, L. 2006 ApJ, **652**, 1050

[5] Birn, J., Forbes, T. G., & Hesse, M. 2006 ApJ, **645**, 732

[6] Brisken, W. F., Benson, J. M., Goss, W. M. & Thorsett, S. E. 2002 ApJ, **571**, 906

[7] Coles, W. A., McLaughlin, M. A., Rickett, B. J., Lyne, A. G. & Bhat, N. D. R. 2005 ApJ, **623**, 392

[8] Cordes, J. M. 1986, ApJ, **311**, 183

[9] Cordes, J. M., Weisberg, J. M., Frail, D. A., Spangler, S. R. & Ryan, M. 1991, Nature, **354**, 121

[10] Cordes, J. M. & Rickett, B.J. 1998, ApJ, 507, 846

[11] Cordes, J. M. & Lazio, T. J. W. 2001, ApJ, **549**, 997

[12] Cordes, J. M. & Lazio, T. J. W. 2002, astro-ph/0207156

[13] Cordes, J. M., Rickett, B. J., Stinebring, D. R., & Coles, W. A. 2006, ApJ, **637**, 346

[14] Dennett-Thorpe, J. & de Bruyn, A. G. 2003, A&A, **404**, 113

[15] Deller, A. T., Tingay, S. J., Bailes, M. & West, C. 2007, PASP, **119**, 318

[16] Dennison, P. A. & Blessing, R. G. 1972, Proc. Astron. Soc. Aust. **2**, 84

[17] Desai, K. M. & Fey, A. L. 2001, ApJs, **133**, 395

[18] Fiedler, R. L., Dennison, B., Johnston, K. & Hewish, A. 1987, Nature, **326**, 675

[19] Goldreich, P. & Sridhar, S. 1995, ApJ, **438**, 763

[20] Hill, A. S., Stinebring, D. R., Barnor, H. A., Berwick, D. E., & Webber, A. B. 2003, ApJ, **599**, 457

[21] Hill, A. S., Stinebring, D. R., Asplund, C. T., Berwick, D. E., Everett, W. B. & Hinkel, N. R. 2005, ApJ, **619**, L171

[22] Kedziora-Chudczer, L. 2006, MNRAS, **396**, 449

[23] Lazio, T. J. W., Waltman, E. B., Ghigo, F. D., Fiedler, R. L., Foster, R. S. & Johnston, K. J. 2001, ApJs, **136**, 265

[24] Lyne, A. G., Anderson, B. & Salter, M. J. 1982, MNRAS, **201**, 503

[25] Macquart, J.-P. & Melrose, D. B. 2000, ApJ, **545**, 798

[26] Narayan, R. 1992, Philos. Trans. R. Soc. London A, **341**, 151

[27] Putney, M. L. & Stinebring, D. S. 2006, Chin. J. Astron. Astrophys., **6b**, 233

[28] Rickett, B. J. 1990, ARA&A, **28**, 561

[29] Rickett, B. J., Lyne, A. G. & Gupta, Y. 1997, MNRAS, **287**, 739

[30] Rickett, B. J., Kedziora-Chudczer, L. & Jauncey, D. L. 2002, ApJ, **581**, 103

[31] Rickett, B. J., Johnston, S., Tomlinson, T., & Reynolds, J. 2009, MNRAS, 395, 1391

[32] Romani, R., Blandford, R. D. & Cordes, J. M. 1987, Nature, **328**, 324

[33] Senkbeil, C. E., Ellingsen, S. P., Lovell, J. E. J., Macquart, J.-P., Cim, G. & Jauncey, D. L. 2008, ApJ, **672**, 95L

[34] Spangler, S. R. 1999, ApJ, **522**, 879

[35] Stinebring, D. R., McLaughlin, M. A., Cordes, J. M., Becker, J. M., Espinoza Goodman, J. E., Kramer, M. A., Sheckard, J. L. & Smith, C. T. 2001, ApJ, **549**, L97

[36] Synthesis Imaging in Radio Astronomy II, eds. Taylor, G. B., Carilli, C. L. & Perley, R. A. 1999, ASP, Vol. 180

[37] Trang, F. S. & Rickett, B. J. 2007, ApJ, **661**, 1064

[38] Walker, M. A., Melrose, D. B., Stinebring, D. R. & Zhang, C. M. 2004, MNRAS, **354**, 43

[39] Walker, M. A. & Stinebring, D. R. 2005, MNRAS, **362**, 1279

[40] Wolszcan, A. & Cordes, J. M. 1987, ApJ, **320**, L35

[41] M.A.Walker, D.R.Stinebring, 2005, MNRAS, 362 (2005) 1279-1285

[42] Thompson, A. R.; Moran, J. M.; Swenson, G. W., 2007, Interferometry and Synthesis in Radio Astronomy, John Wiley & Sons,

[43] Rchard N. Manchester, Joseph H. Taylor, 1977, Pulsars, W.H. Freeman and Company,

[44] Andrew Lyne, 2006, Pulsar Astronomy, Cambridge Astrophysics,

[45] Ferriere, K. 2001, Reviews of Modern Physics, **73**,1031

[46] McCray, R., and T. P. Snow, Jr., 1979, Annu. Rev. Astron. Astrophys. **17**, 213.

[47] Carruthers, G., 1970, Astrophys. J. Lett. **161**, L81.

[48] Manchester, R.N., Taylor, J.H., 1972, Astrophys. J. Lett. **10**, 67-70

[49] Frank S. Trang, Barney J. Rickett, 2007, ApJ, **661**, 1064-1072

[50] W. A. Coles, J. P. Filice, R. G. Frehlich, and M. Yadlowsky, 1995, Applied Optics, Vol. 34, Issue 12, 2089-2101